Giant magnetoresistance based sensors for local magnetic detection of neuronal currents

Laure Caruso

▶ **To cite this version:**

Laure Caruso. Giant magnetoresistance based sensors for local magnetic detection of neuronal currents. Medical Physics [physics.med-ph]. Université Pierre et Marie Curie - Paris VI, 2015. English. NNT : 2015PA066272 . tel-01241867

HAL Id: tel-01241867

https://theses.hal.science/tel-01241867

Submitted on 11 Dec 2015

HAL is a multi-disciplinary open access archive for the deposit and dissemination of scientific research documents, whether they are published or not. The documents may come from teaching and research institutions in France or abroad, or from public or private research centers.

L'archive ouverte pluridisciplinaire **HAL**, est destinée au dépôt et à la diffusion de documents scientifiques de niveau recherche, publiés ou non, émanant des établissements d'enseignement et de recherche français ou étrangers, des laboratoires publics ou privés.

Université Pierre et Marie Curie

Doctoral school ED PIF

CEA Saclay, DSM/IRAMIS/SPEC/LNO

Giant magnetoresistance based sensors for local magnetic detection of neuronal currents

Par Laure Caruso

Thèse de doctorat de Physique

Dirigée par Myriam Pannetier-Lecoeur

Présentée et soutenue publiquement le 21/07/2015

Devant un jury composé de :

Professor Risto Ilmoniemi : reviewer

Professor Michel Hehn : reviewer

Susana de Freitas

Thierry Bal

Régis Lambert

Denis Schwartz

Contents

Introduction

Neurosciences represent a large scientific research field on the brain and the nervous system which has developed many ramifications across experimental and theoretical disciplines to unveil an exquisitely complex biological system.

The brain orchestrates actions, thoughts and perceptions through fast neuronal communications, thanks to neuronal cells which convey information across complex temporal patterns within the neuronal network. Breaking the neural code is intertwined with the development of new neurophysiology methods.

The purpose of the present thesis work is to develop a novel tool for neurophysiology, able to detect the neuronal activity at local scale through the magnetic field generated by the electrical activity. Detecting and imaging the brain activity through the magnetic signature is the method used for MagnetoEncephalography (MEG) which is a worldwide developed technique for clinical investigation in neurosciences. However, MEG requires to have thousands of neurons synchronized to be able to detect a signal and the detailed magnetic field sources are not fully understood. For that reason, a number of researchers have tried or are trying to perform more local experiments.

So far, only macroscopic experiments have been performed, either with SQUIDs located on each side of an *in vitro* brain slice [1], either by means of toroidal coil wound round the cells [2] or with chip scale atomic magnetometers. In these experiments, the signal is measured at best at mm distance from the source and is not really local.

In the framework of the European *Magnetrodes* project, in collaboration with INESC-MN (Lisbon), UNIC-CNRS (Gif-sur-Yvette), ESI (Frankfurt) and Aalto University (Espoo), we aim to develop the magnetic equivalent of electrodes, named "magnetrodes", able to be implanted *in vivo* to measure magnetic fields at scales of tens of microns.

The challenge is to build a magnetic sensor sensitive enough, integrable on a very thin tip because the amplitude of the expected signals is in the range of pT to few nT at small distance from the sources. In addition, the nature of the neuronal activity (Local Field Potentials and

Action Potentials) provides a temporal dynamic varying from DC to few kHz.

Recent advances in spin electronics have permitted to give rise to magnetoresistance based sensors, which present a large working frequency bandwidth (DC to few GHz) and can be miniaturized in micro metric devices. Those characteristics have driven the chosen magnetrode technology (here GMR sensors) as the most promising approach for the required conditions.

The first chapter focuses on the physiological function of neurons. First, the biology of neuronal cells including their structure and function is reported. Second, a general overview of the primary techniques of basic neurophysiology research such as electrophysiology and magnetophysiology at different levels of scrutiny is reported. In this chapter, we are also giving a basic model of a neuron or an assembly of neurons to estimate the magnitude of magnetic signals and we present some more elaborated models.

The second chapter introduces a state-of-the-art on biomagnetic sensors. A brief overview on ultra-sensitive magnetometers currently used for MEG measurements (SQUIDs and atomic magnetometers) is described before introducing the physics beyond the magnetrode technology: spin-electronics based sensors. One of the main constraint in studying tiny magnetic field is to identify and control the noise sources; hence a section is dedicated to the noise sources emerging in GMR sensors.

In the third chapter, the attention is focused on the magnetrode sensors developed throughout this work. Two kinds of probes have been developed: first ones are planar probes (ECoG-like) dedicated to analyze the neuromagnetic signature at the surface of the tissues (i.e either *in vitro* and *in vivo* experiments) while second ones are sharp magnetrodes, processed as a needle-shape to allow penetrating the tissues. The microfabrication process developed throughout this work is presented for both planar and sharp GMR based sensors. Their characterization and performances in terms of noise, sensitivity and detectivity are given.

Furthermore, in order to test the magnetrode technology before experimenting on physical model (biological tissues), a simple phantom was realized to mimick the neuronal behavior in a biological-like solution (Artificial CerebroSpinal Fluid).

The two last chapters (4 and 5) are devoted to the results obtained on living tissues with the magnetrode technology. Chapter four focuses on magnetic recordings performed on *in vitro* models. The first one is a mammalian muscle which involves relatively simple mechanisms thanks to the basic features of chemical synaptic transmission, in contrast to central nerve cells which have convergent connections, since muscle cells are mono-innervated

with a single excitatory synapse. The detection of magnetic fields created by axial currents within a mouse muscle (soleus muscle) are strong enough to be sensed by planar magnetrodes. The second studied model is mouse hippocampus slices, commonly used in electrophysiology thanks to synchronous activity of parallel-arranged pyramidal cells. Both muscle and slice magnetic recordings are fully described in this chapter.

The following chapter (5) reports the results obtained *in vivo* in the visual area of anesthetized cats. These experiments were performed in parallel to electrophysiological recordings. The experimental setup and the first magnetic recordings results are presented.

A general conclusion and perspectives of this work are given in the last part.

During this thesis, I designed all the set of masks used for sharp magnetrodes. I also developed the process for these probes and realized by myself the microfabrication and packaging probe as well as their characterization (noise measurements, response in field). The fabrication of planar probes has been realized in collaboration with Elodie Paul who is the process engineer of the lab. The electronics schemes developed throughout this work were realized by the team of the lab. I participated to the experiments (hippocampus slices, muscle and cortex) in collaboration with the CNRS-UNIC at Gif-sur-Yvette (France) and the ESI team in Frankfurt. Modeling at cellular scale has been done by F. Barbieri from CNRS-UNIC team and the simple magnetic modeling presented in section 1.3.3.1 has been developed by C. Fermon.

Chapter 1

Neurophysiology

Neurophysiology addresses the study of the nervous system at various levels: from brain scale to ion channels, in order to understand how the brain is functioning. One part of the answer can be found in neural coding and neuronal communication. Due to its extreme complexity, our knowledge of this organ is still uncompleted, therefore, understanding brain activity requires simultaneous recordings across spatial scales, from single-cell to brain-wide network, providing information about the relationship between structure, function and dynamics in neuronal circuits and assemblies. In this chapter, I will briefly describe the biology of neurons and their corresponding signals, then I will discuss the neurophysiology techniques developed to access brain activity.

1.1 Biology of neurons

1.1.1 Structure of neurons

1.1.1.1 From brain to neuronal cells

The nervous System is composed by the Central Nervous System (CNS), consisting of the brain and the spinal cord, and the Peripheral Nervous System (PNS), which connects the CNS to the limbs and organs through the spinal cord and nerves (motor command and sensory inputs)[3]. The mammalian brain includes the cerebral cortex and deep brain structures (brain stem, thalamus, cerebellum, hippocampus, basal ganglia) and contains more than a billion neurons, each neuron being itself connected to a thousand of neurons. This complex network allows perception, movement and consciousness.

CNS contains two types of cells; excitable cells and non excitable cells (like glial cells,

which play a support and nutritive role). Neuronal cells (i.e neurons) are excitable cells, like myocardial and skeletal muscle cells; they are able to trigger Action Potential (AP) and are the main signaling units of the nervous system.

Neurons within the cerebral cortex are organized into columnar structures called cortical columns (figure1.1). The neuronal communication occurs within these cortical columns through neurons which represent the basic unit of the nervous system.

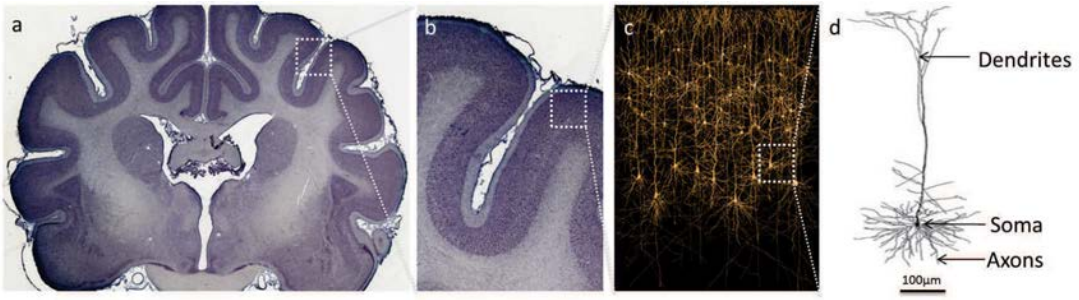

Figure 1.1: From brain to neuron. a) Coronal plane of a human brain b) Zoom-in of the cortex (superficial layer in violet) (adapted from Brainmaps.org). c) The cortical columns are parallely arranged within the cortex d) Single neuron in rat cortex (layer V) (adapted from [4])

1.1.1.2 Neuron morphology

A neuron comprises a cell body (soma) and two extensions: the dendrites that receive neuronal inputs (input components) and the axons that carry the information to other neurons. The soma (integrative component) is the metabolic center that contains the nucleus, allowing storage of the genes and synthesis of cell's proteins. Axons (output components) transmit nervous signals to other neurons, glands and muscles. If some axons are surrounded by an insulating myelin sheath that increases the speed of AP propagation [3, 5], neurons in the cerebral cortex are myelin-free. The typical morphology of a pyramidal neuron is shown in Figure 1.1d).

1.1.2 Function of neurons

1.1.2.1 Ions flux across the neural cell membrane

The neural cell membrane is a lipid bilayer (made of proteins) that defines the intracellular from the extracellular medium. Contrary to electric currents carried by electrons, electric currents in solution are carried by ions, thus electric signals in neurons are guided by ions

moving across transmembrane channels according to their electrochemical gradients. The transmembrane gradients are expressed by an electric potential difference between the inner and outer edges of the cell membrane. At rest, neurons maintain this potential difference, which is typically -65 mV amplitude (-90 mV for muscle) considering that the net charge outside of the membrane is arbitrarily zero. This potential is called the resting membrane potential and it is controlled by ionic pumps and channels within the cell membrane that forms the membrane's permeability. Ionic flux on both sides of the membrane is controlled by ionic diffusion to achieve a concentration equilibrium.

When a stimulus appears (either physical or chemical changes) ionic channels (Na^+) open temporarily and let Na^+ ions enter into the cell. This mechanism is guided by concentration gradient and electrostatic pressure, which brings the inner cell more positive while K^+ ions are pushed out through K^+channels because of the electric changes. A change in the cell polarity brings the cell to depolarize over a threshold: if the threshold is not reached, the cell returns to its resting membrane potential or fires if the threshold is exceeded.

This ionic flux through transmembrane ion channels exhibits amplitude, shape and duration recorded mainly electrophysiologically or by optical methods (cf Part.1.2 and Part.1.3). The study of ionic currents remains nowadays the possibility to have access to neurosignals transmission from cellular scale to macroscopic scale which is a key element for understanding how the brain works.

1.1.2.2 Neurotransmission

Neurons process and transmit electrochemical messages to other neurons through synapses. A synapse is a junction between a pre-synaptic neuron and a post-synaptic neuron. Neurotransmission within synapses occurs when a pre-synaptic neuron sends an electric signal through its axon to the post-synaptic neurons releasing neurotransmitters. Neurotransmitters are endogenous chemicals that can be excitatory or inhibitory (mostly glutamate or γ-Aminobutyric acid (GABA)) allowing neurons to trigger nerve signal (cf section1.1.2.3).

When an AP arrives at the axon terminal, voltage gated calcium channels open and induce the neurotransmitters release (excitatory or inhibitory). The neurotransmitter is then fixed on the membrane of a post synaptic channel receptor. The effect of the receptor opening is translate into the Post Synaptic Potential (PSP), that can either be inhibitory or excitatory (Figure 1.2). One can distinguish axial currents, transmembrane currents and extracellular currents.

1.1.2.3 Action Potential

Action potentials are the building blocks of the electric neuronal communications since they convey the neuronal information from one place to another in the nervous system (other neurons, muscle fibers...). An action potential (AP) is a fast transient depolarisation of the plasmic membrane that is triggered under a certain threshold and the firing action potential rate is depending on the permeability of the neuronal membrane (figure 1.3).

When a signal arrives in the axonal termination of a pre-synaptic neuron, the voltage-gated calcium channels open to trigger the neurotransmitters release; it creates a small depolarisation and thus changes the membrane potential; the signal is carried towards the soma (Post-Synaptic Current-PSC); if the signal reaches a certain threshold, the AP is transmitted along the axon; the neuron fires.

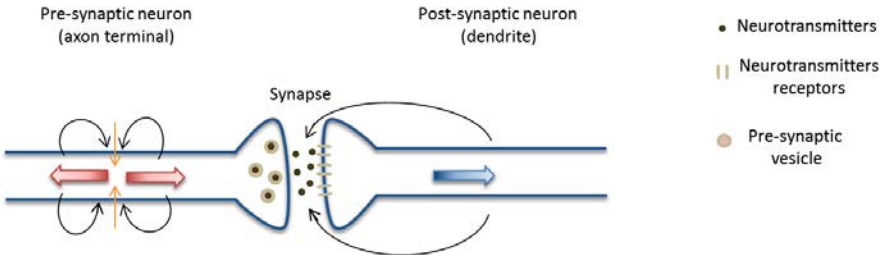

Figure 1.2: AP transmission between a pre-synaptic neuron and a post-synaptic dendrite. When the depolarization (AP) arises in the axon terminal, neurotransmitters are released, generating a Post-Synaptic Current (PSC). The red arrows are the action potential currents, the blue arrow is the PSC and the orange arrows are the transmembrane currents.

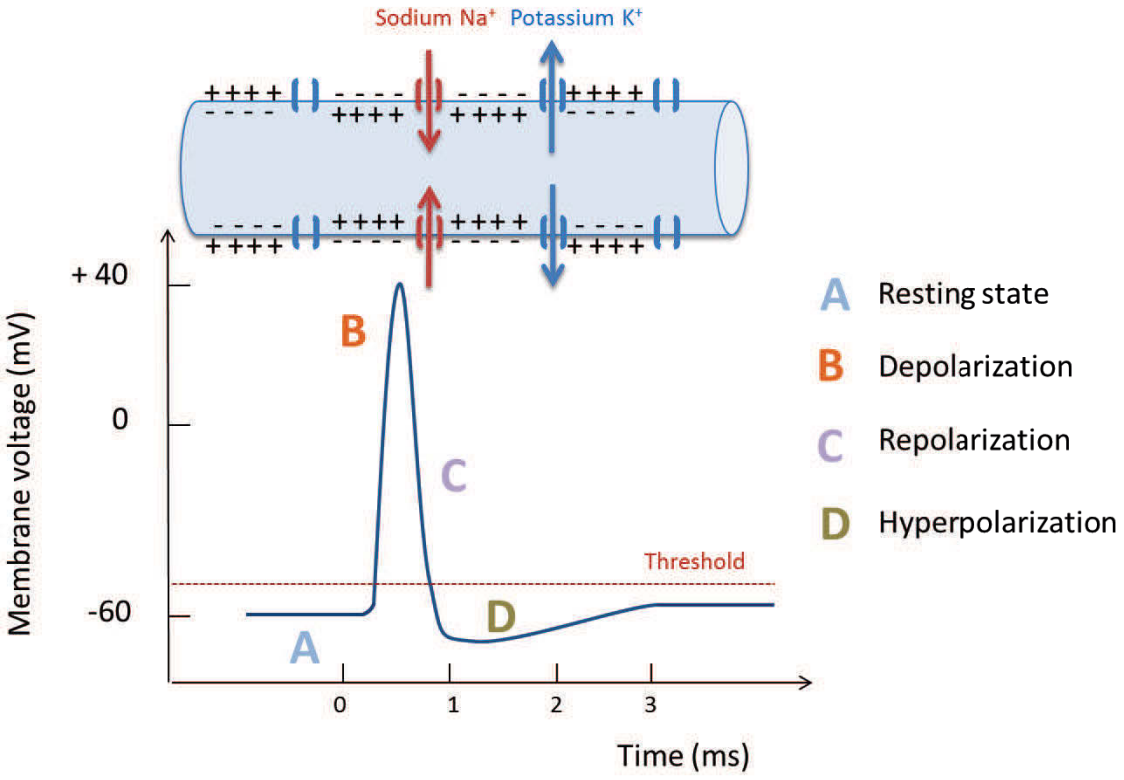

Figure 1.3: Action Potential generation: when Sodium ions enter through the membrane, the local potential (which was at its resting value (A)) increases and reaches a strong positive value (B); the opening of the Potassium channels which drives positive ions from the inside to the outside of the cell induces a decrease in the membrane potential (C). The last phase is the hyperpolarization (D) where the potential returns to its resting value.

1.1.2.4 Local Field Potential

Local Field Potential (LFP) refers to the electric potential in the extracellular space around neurons. LFPs are mostly generated by synchronized synaptic currents arising on cortical neurons and can provide relevant information that is not present in neuronal spiking activity. However, the origin of those signals is still unclear and is subjected to discussions in the neurosciences community: [6, 7].

LFPs can either be recorded by a single-electrode or multi-electrode arrays [8, 9] and their frequency range (0.3 - 300 Hz) leads to information on cerebral rhythms [10]. Figure 1.4 shows typical LFP response recordings with multielectrode array in human.

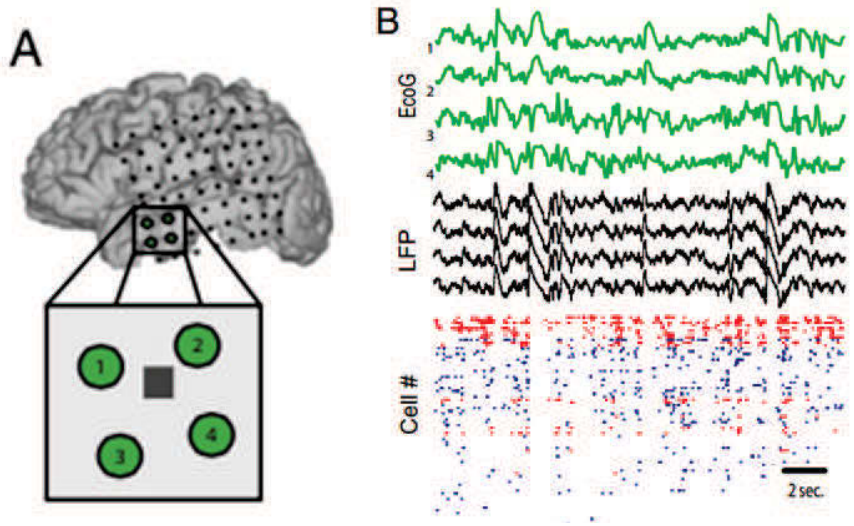

Figure 1.4: Local Field Potentials recorded during slow-wave sleep in human. a) Medium temporal lobe recordings. Green circles represent four surface electrodes and the grey square the Utah array (100 silicon electrodes) that record LFPs in depth b) Delta waves (high amplitudes, low frequency -< 4 Hz waves) visible both with surface electrodes (ECoG (see 1.2.1.2), green traces) and with deep electrodes (Utah array, black traces). Cell # represents the firing cells of identified neurons (red (inhibitory) and blue (excitatory)). Modified from [11]

1.2 Electrophysiology

The most popular and well known technique to investigate the temporal brain response is electrophysiology, used since the 18th century when Luigi Galvani discovered the link between nervous system and electric activity [12]. Electrophysiology tools measure the electrical activity in living cells (nerve, muscle[13]), in the extracellular and intracellular medium[14]. This activity results from changes in ionic currents (i.e ionic flux), creating small electric and magnetic fields that constitute the main source of information in neurosciences. Here are presented the most common methods used to record electrical activity, classified by decreasing size of the ensemble studied, from whole brain to unique cell compartment.

1.2.1 Macroscopic scale

1.2.1.1 Electroencephalogram - EEG

Electroencephalogram (EEG) is the oldest and most widely used non-invasive method investigating cerebral electrical activity through a net of hundreds of electrodes (up to 256) mounted

at the surface of the scalp. Electric currents contribution in the extracellular medium generate a potential (scalar and measured in volts) with respect to a reference potential. This potential difference represents an electric field (vector measured in volts per meter) which is measured in EEG with millisecond resolution and mostly comes from synaptic activity (excitatory and inhibitory)[15, 10]. This non-invasive technique allows measurements in human while most of the cerebral processes data are coming from animal models. EEG is widely used in clinical applications diagnostic (Parkinson's disease, epilepsy...) as well as for cognitive research (perception, movement, language, memory...)[16, 17]. Moreover, as the measured signal is collected from two electrodes far from dipole sources, it comprises distortion and attenuation effects due to conductivity of other tissues (bone, skull, skin...) that thereby decreases the spatial resolution (cf Figure 1.7).

1.2.1.2 Electrocorticography - ECoG

Invasive techniques such as ECoG and microelectrode array have been developed because of few clinical settings like movement disorders localized in deep brain structures (basal ganglia or thalamus) and in patients with intractable epilepsies [8, 18]. ECoG is composed by a flat array of platinum-iridium or stainless steel electrodes to record at the surface of the cortex thereby bypassing skull distortion of the electric signal. Flat array of electrodes covers large cortex areas allowing the study of neuronal communications through brain signal analysis such as LFP recordings [19] and chronic implantation can be achieved by means of flexible grid electrodes [20]. Typical spatial and temporal resolution for electrocorticography are 1 cm and 5 ms respectively (Figure 1.7)[21].

1.2.2 Mesoscopic scale

At cellular level, neuronal signaling is mainly investigated by electrophysiology and very recently by optical detection. One measures the electric potential variation within neurons while some optical detection techniques measure a change in the optical emission of fluorescent neurons genetically modified using light. Electrophysiology tools give an extremely high signal-to-noise ratio with a direct electrical measurement and optogenetic signals are recorded by means of designed molecules that convert membrane potential into an optical signal, which is an indirect measurement. Nevertheless, electrophysiology techniques are very invasive at this scale owing the need of a physical contact with the medium whereas optical methods are less invasive techniques which exploit the relative transparency of tissues to the light for surface structures. Both techniques are reported below.

1.2.2.1 Extracellular recordings

Extracellular recordings represent a large neurosciences research field involving the use of several types of tools to investigate the neuronal signature in the extracellular medium. Large-scale recordings from neuronal ensembles are now possible with microelectrodes and micro-machined silicon electrode arrays [14].

Single microelectrode Simple electrodes can be inserted within the tissues to record LFPs in the extracellular medium. Various types of electrodes can be used, either metallic or made of glass (capillary filled with a conductive solution).

Microelectrode arrays Microelectrode arrays (MEA) are devices that contain several electrical probes to measure directly the extracellular potential of neurons in a relatively large neuron network (up to thousands of neurons). Inserted microelectrodes allow exploring the electrical activity of deep layers, giving access to LFP signal as well as AP since the frequency operating range varies from direct current to few kHz [22]. Electrodes can be made with metal, glass or silicon. University of Utah and BlackRock Mircosystems [23] have developed an extracellular multi-electrode array system (containing up to 96 electrodes) called "Utah array" which is nowadays a benchmark for multi-channel recordings; such recordings detect neuronal signals within a large population of neurons, allowing spatial reconstruction of the neuronal activity.

1.2.2.2 Optical techniques

Optical techniques start to be used often for neuronal activity studies at cell level. Two main optical methods have been developed over the last 15 years: calcium imaging and Voltage Sensitive Dyes Imaging (VSDI), which allows optical detection of neuronal electrical activity and optogenetics which on the opposite uses light as a neuronal activity trigger.

First technique to use light for neural recordings is calcium imaging that use fluorescent molecules (calcium indicators) to record membrane voltage changes through the variation of the calcium concentration. It is then an indirect membrane potential measurement. Another recent technique, the VSDI method measures directly the membrane voltage changes through optical recordings. A voltage-sensitive dye is injected into neurons and a high-resolution fast-speed camera detects the membrane voltage changes at the peak excitation wavelength of the dye.

Optogenetics combine both genetics and optics to probe the neuronal electric signature by means of optical techniques (*Nature's "method of the year" 2010*). It involves exogenous genes coding for light-sensitive proteins within neurons that are activated or inhibited during a light emission: the recorded signal is then a photon flux coming from the fluorescence of light-sensitive proteins within neurons. By using voltage-sensitive dyes (VSDs), one can trigger the photosensitivity and control the membrane voltage potential by switching the wavelength of the light. A blue light (473 nm) will then trigger neurons to fire while yellow green (532 nm) will keep them quiet. This on-off switching is a tremendous advance in signal processing and allows new opportunities for both healthy and diseased brain [24]. Optogenetics can record signals from a single spine ($\backsim$1 µm) to brain level area (2 mm) that reveal a very high temporal resolution (see Figure 1.5) with reduced invasiveness compared to electrophysiology techniques. However, the light scattering limits the technique to surface events investigation.

However, limitations are the low signal-to-noise ratio, the phototoxicity which can damage nerve cells and the indirect measurement since the electric signal is converted into an optical signal and the light scattering effect becomes prohibitive for depth tissues (cf table 1.9).

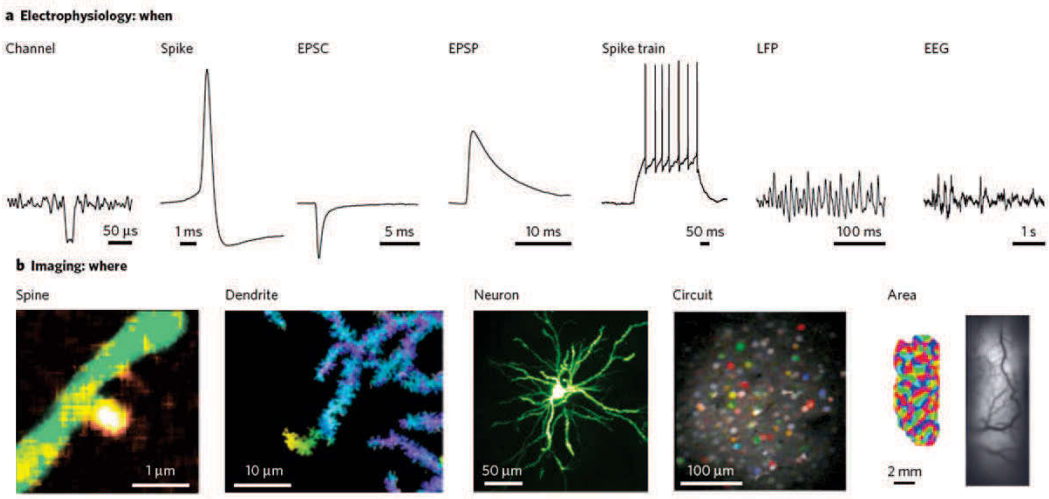

Figure 1.5: Electrophysiology and optogenetics methods spatial and temporal scales. a) Electrophysiology can record single channel, spikes, Excitatory Post Synaptic Current (EPSC) and Excitatory Post Synaptic Potential. Representative examples shown are of a single nicotinic acetylcholine channel opening; an action potential in a cerebellar interneuron *in vivo*; an excitatory post-synaptic current (EPSC), an excitatory post-synaptic potential and a spike train from cerebellar granule cells *in vivo*; gamma oscillations (LFP) recorded in the hippocampus of an anaesthetized rat; and an electroencephalogram from an anaesthetized mouse during visual stimulation. Adapted from [24].

1.2.3 Microscopic scale

Electrophysiological recordings at cellular level can be performed on *in vitro* cells, for instance brain cells, which are kept in a nutritive, temperature and humidity-controlled environment, or during *in vivo* experiments with implanted electrodes. One way to get the efficient coupling between the cell membrane and the measuring electrode is to use intracellular methods such as patch clamping that records faithfully the voltage or current across the cell membrane by inserting very thin probes (usually glass micro-pipette).

1.2.3.1 Intracellular recordings

Patch-clamp Intracellular recordings investigate neuronal cell activity at microscopic scale *i.e* at cellular scale. The patch-clamping has been developed by Neher and Sackman [25] and gives rise to voltage clamp and current clamp techniques. The basic idea is to penetrate the cell using a microelectrode or a glass micro-pipette to precisely measure the voltage across the cell membrane and investigate the membrane-contained ion channels with minimal damage to the cell (Figure 1.6); nevertheless, patch-clamp recordings are performed in a limited time mostly because the pipette is penetrating the cell membrane which makes the technique invasive.

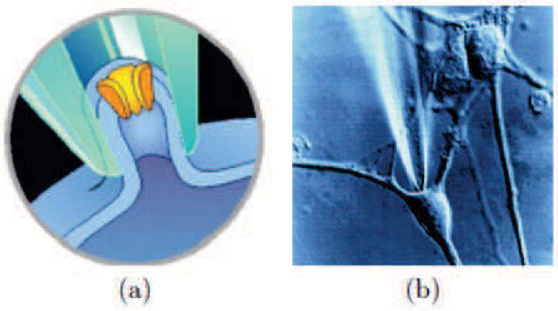

Figure 1.6: Schematic representation of intracellular recordings. (a) Patch-clamp principle (cell-attached technique): a thin pipette (1 µm diameter), isolates an ionic channel to perform intracellular recordings. (b) Microscopy image of patch-clamping. Adapted from [26].

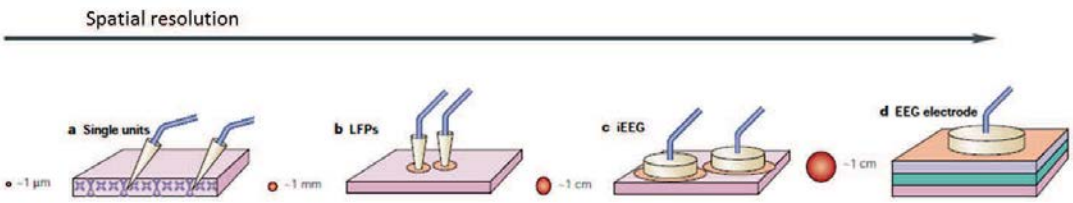

Figure 1.7: Electrophysiology recordings at various scales: from scalp to single-unit recordings Adapted from [27].

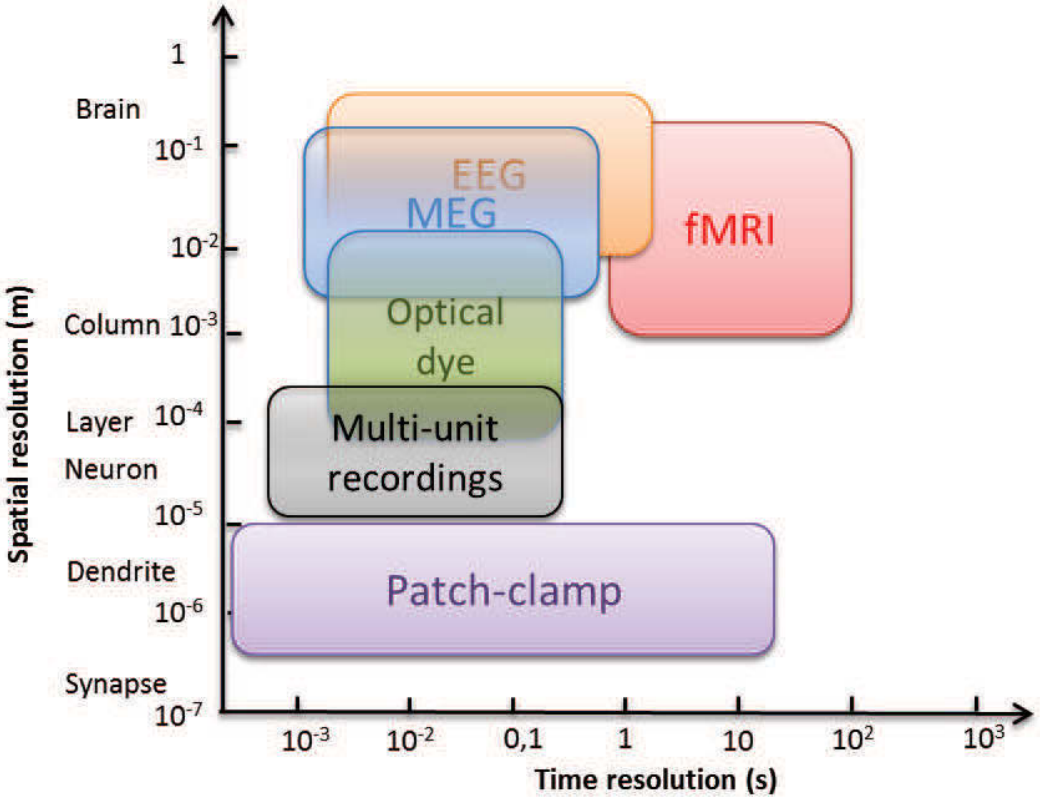

Figure 1.8: Comparison of several techniques used for electrical, magnetic, optical recordings, of neuronal activity, in terms of spatial and time resolution.

	Advantages	Disadvantages
Electrophysiology	• High temporal resolution, • High SNR • Direct electric measurement	• Low spatial resolution • Invasive measurement • Need of reference
Optogenetics	• Targetted stimulation, • No physical contact with cells • Simultaneous recordings on multiple sites	• Low SNR • Light scattering • Indirect measurement • Phototoxicity
Magnetophysiology	• Reference free • High dynamical temporal resolution • **Direct current measurement** • Vectorial information	• Technologically challenging at cellular scale • Inverse problem at brain scale

Figure 1.9: Advantages and disadvantages between the presented techniques: electrophysiology, optogenetics and magnetophysiology.

1.3 Magnetophysiology

Magnetophysiology, which consists on measuring the magnetic field generated by the ionic currents is much less developed than electrophysiology. The main reason is the weakness of the magnetic fields at the surface of the body. The signals, typically 7 to 9 orders of magnitudes lower than the Earth field and typically 5 orders of magnitude lower than the environmental magnetic noise require shielded environment and very sensitive magnetic sensors. In practice, nearly all the existing systems are using SQUIDS (Superconducting QUantum Interference Devices) which will be described in chapter 2. These sensors need a nitrogen or helium liquid cooling inducing very expensive and complicated systems for the detection. However, MEG (MagnetoEncephalography) has been developed since the 1950's and now about 300 systems are installed around the world. MCG (MagnetoCardiography) has been also developed up to a commercial state but only few systems are presently working around the world.

1.3.1 Brain scale: magnetoencephalography

The principle of a MEG system is to use a large array of cm-size SQUIDs sensors which record different magnetic fields or field gradient components [28]. Any current is creating a magnetic

field and if a large enough number of neurons are coherently activated, the magnetic fields are summing up and a measurable magnetic field can be detected outside of the brain. If this field is well mapped, current sources can be reconstructed allowing 3D localization of active electrical sources [29]. However, these magnetic signals are smalls, in the range of 10 to 500 fT and comparable to the magnetic noise of the brain, typically 100 fT at low frequencies, created by the normal brain background activity. For that reason, an averaging with an external trigger is commonly used in MEG recordings (evoked potentials). Reference [30] is giving a recent review of MEG and comparison with fMRI (functional Magnetic Resonance Imaging) which is a complementary way of performing functional brain imaging. If localization of sources is of main interest of MEG, the evaluation of the strength of the signals and the exact origin of the MEG signals, primary, volume currents or a combination of both is still under discussion.

1.3.2 Local measurements

A number of more local signals measurements have been performed in the last years using different kind of sensors. One approach is using atomic magnetometers of several mm size inserted as near as possible of the brain. Epileptic spikes on a rat have been recently measured by that technique [31] with detected amplitude of about 3 pT at the surface of the brain.

Some measurements of slices using millimeter size SQUIDS have been also performed [32] and more recently using high-temperature SQUIDs [33, 1]. Typical amplitudes detected were also in the range of 5 pT up to 15 pT at a distance of 3-4 mm.

Another experiment consisting on using a toroidal pick-up coil around an isolated crayfish giant axon has been performed [34]. Measurements on a human nerve have been also performed by the same approach [35]. These measurements gave amplitude up to 300 pT of amplitude with a dipolar shape very similar to what we measured on a muscle (see Chapter 4, section 4.1).

A first set of experiments has been done by INESC-MN [36, 37] using magnetoresistive (MR) sensors, that could not evidence a purely magnetic response component. The measured signals show a strong capacitive coupling between the sensor and the living medium, whose large amplitude might have concealed the magnetic signature.

1.3.3 Magnetic field created by neurons

One important question related to our work is to evaluate what is the amplitude and direction of the magnetic field created by a single neuron or by an assembly of neurons. Magnetic fields are created by any currents flowing inside the brain. Hence intracellular axial currents are a first source but return currents, acting like a counterpart, are also a second source of magnetic fields. Seen at a very large distance, all the currents are cancelling and the created magnetic field disappears. At a cm distance, corresponding to magnetoencephalography, intracellular currents and extracellular currents have not the same space distribution and a net signal can be detected. Locally, the intracellular axial currents will have a dominant contribution in the detected magnetic field.

1.3.3.1 A very simple model of a single neuron

In this part, we will focus first on the determination of the magnetic field created by a single neuron. For that, we first consider the most simple model but able to give already an order of magnitude and to help better understanding the physics.

The neuron is modeled as a cylinder with a typical neuron diameter of $d = 2$ µm and a resistivity of $\rho_S = 150$ Ω.cm. When an action potential is created, the potential difference in the neuron induces a net current given simply by the Ohm law. Hence, a $V_p = 20$ mV difference inside the neuron on a distance of $l = 200$ µm is creating a net current of

$$I = \frac{\pi d^2 V_p}{\rho_s l} = 0.87\, nA \tag{1.1}$$

The field induced by this direct current can then be calculated through the Biot and Savart law. For a very small distances r compared to the neuron length, the field is orthoradial and simply given by:

$$B_\Theta = \frac{\mu_0 I}{2\pi r} \tag{1.2}$$

which gives in our specific case a field of 17 pT at 10 µm. The field (H) is given in A/m and the magnetic induction B in tesla (T); both are related through $\mu_0 = 4\pi 10^{-7}$ In all this thesis, we will always normalize both to tesla. When the distance r increases and becomes comparable to l, the field is decreasing as r^2 (dipolar configuration), and at very long distances as r^3.

To better understand the shape of the field during the AP propagation, we can consider the propagation of the AP. In that case, two opposite currents exist, creating opposite fields.

Then at small distances, we would measure a bipolar shape of the field in time which is what was observed in the muscle (see Chapter 4), while at large distances the AP behaves like a quadrupole. The peak-to-peak amplitude of the field will be of the same order of magnitude than the first calculation.

The next step in this very simple model is to introduce the extracellular currents of this direct current. It should be noted that the total extracellular currents are of the same amplitude than the direct currents but they occur in the external medium.

Here also the model can be in a first approach very simple. We may consider that the extracellular currents are passing the neuron membrane at regular points and are closed inside a continuous medium which have a conductivity of the same order than inside the neuron. Then, the typical extent of these extracellular currents is a volume of about l^3 around the neuron. Hence, if the distance of measurement r is small compared to l, the extracellular currents are surrounding the measurement point and the corresponding field is very low. This will however be wrong if the magnetic sensor used is on a large tip which breaks the network symmetry. Then, extracellular currents may have a very large cancellation effect of the direct currents. The computation of the extracellular currents would give a total field of 14 pT at 10 µm in case of symmetrical extracellular currents and of about 10 pT is case of symmetry breaking.

In order to have a time reconstruction of the signal, it is necessary to introduce the propagation of the AP. Typical speed of the propagation gives a signal extent of about 2 ms with a bipolar shape.

1.3.3.2 More sophisticated models of a single neuron

More sophisticated models may incorporate three different aspects neglected in the very simple model. The first one is the geometry of a complete neuron which is far from a simple cylinder. The second aspect is to introduce the frequency dependence of the transport inside the neuron, through the membranes and in the extracellular medium which induces a large frequency dependence of the fields predicted and the third one is to compute the time variation of the signal taking into account the capacitances and resistances (cable theory).

Models have been proposed by J.P. Wikswo group to describe their observations on single giant axons [38, 39, 40, 34] which gave a rather accurate view of the propagating AP. This nerve model has a lot of similarities to the muscle model we have studied (chapter 4).

Figure 1.10 gives the fields calculated with a more realistic model for a single neuron [Francesca Barbieri, Thierry Bal and Alain Destexhe, *private communication*] introducing

theses three aspects. Compared to our simple model, the field found is of the same order but these simulations allow describing the shape of the magnetic signal as function of time and as function of the observed part of the neuron.

In these models however, return currents have been considered as symmetrical and hence neglected.

Murakami *et al* [41, 42, 32] have developed models to explain MEG signal amplitudes from single neuron activity. The amplitude found for a single neuron is of the order of 0.4 to 3 pA.m which, taking a length of 200 µm common to our model and field decreases extent in the Barbieri model, leads to a field of 1.2 nT to 10 nT, typically 2 to 10 times higher than the simple model. Largest current spikes are seen in pyramidal cells.

Blagoev *et al* [43] have also developed a model taking into account the geometry of the neurons in order to evaluate MEG signals intensity. Their results are in agreement with the Barbieri model.

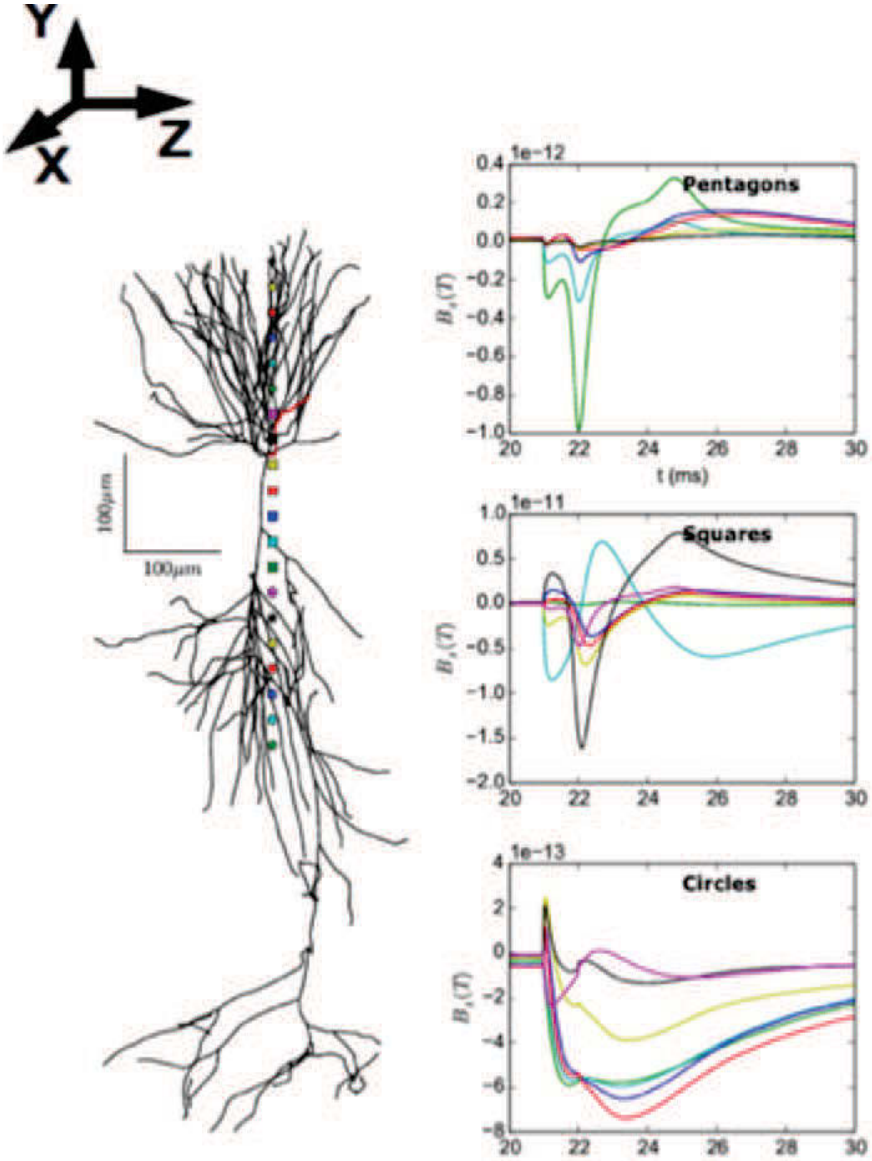

Figure 1.10: Magnetic field calculated in different positions along the dendritic tree. The positions are shown as pentagons, squares and circles along the neuron and are lying on the y-z plane at x = 10 µm. The column of panels represent respectively the z component of the MF versus time. The largest fields are found in the region around the soma, axon and proximal trunk, where the axial currents are the strongest. The beginning of the AP is fixed at 21 ms. *Courtesy F. Barbieri.*

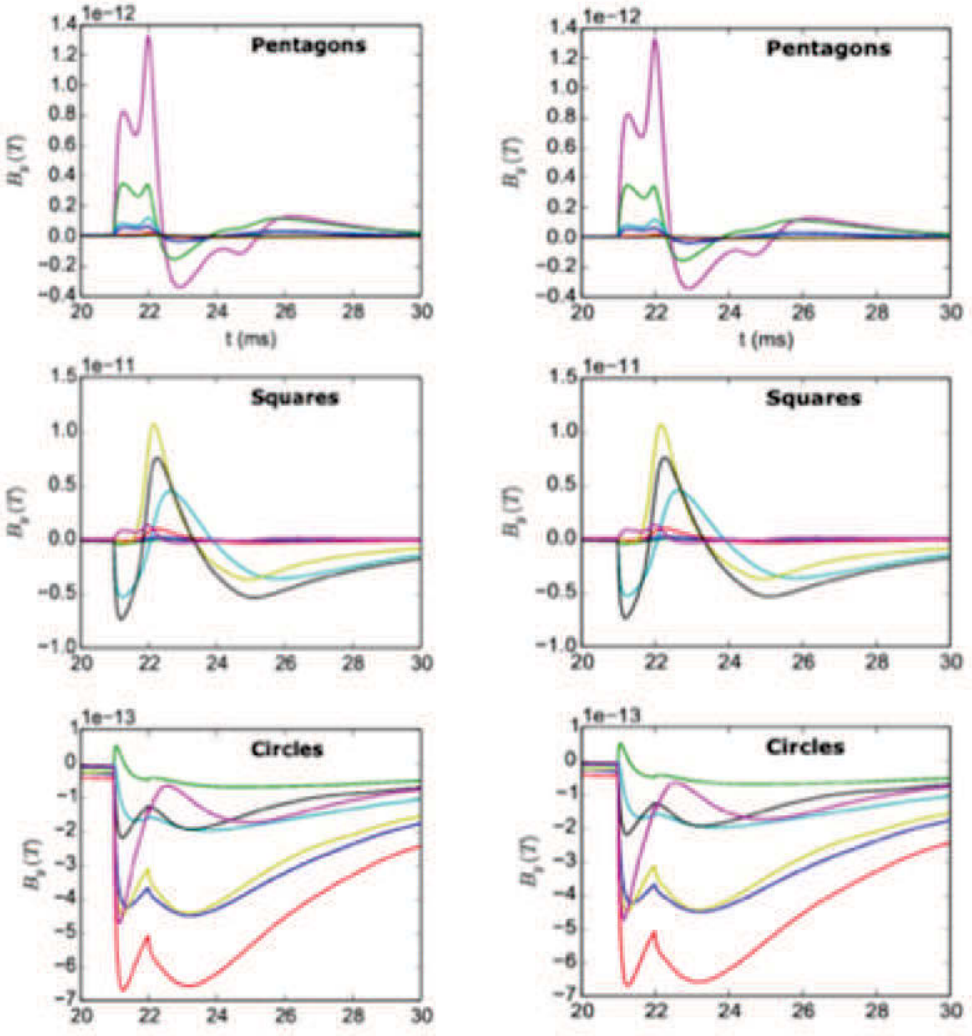

Figure 1.11: Magnetic field calculated in different positions along the dendritic tree. The column of panels represent respectively the x (left) and y (right) component of the MF versus time. *Courtesy F. Barbieri.*

1.3.3.3 Assembly of neurons

A single neuron is presently not measurable due to the weakness of the expected signal so we have until now investigated an array of neurons which present a coherent response. A simple model is just to consider that neurons are regularly disposed in a bundle and are fully synchronized. In that case, it is essential to consider the breaking of symmetry created by the probe *i.e.* only a half space is filled with neurons. Indeed, when the probe (200 µm thick for sharp probe, cf Chapter 3) is inserted into the tissues, it pushes neurons away and thus

the contributions of neurons located near the back of the probes have less contributions than those in front of the probe (where the sensor are). Therefore, the symmetry is broken and the contribution of extracellular currents is not the same anymore.

A typical distance between neurons is about 10 µm.

If we take our very simple model of the neuron, we can evaluate the field created by the assembly of neurons. We have developed for that purpose a simple software which allows creating an array of neurons with a triangular or square order and a given surface. We calculate the field created at the surface of this volume at the typical position of our probe. If we consider an array of 100 neurons synchronized measured at the edge, the field obtained is 260 pT with similar neurons as described above. If we consider 1000 neurons (300 µm x 300 µm array), we obtain a field of 1 nT. For a 1 mm^2 region (10000 neurons) we obtain a field of 2 nT.

If we take a more realistic model [F. Barbieri *et al, private communication*], we obtain the same scaling of field amplitude as a function of number of neurons in the array. Figures 1.12 and 1.13 are giving the modeled distribution and the obtained fields.

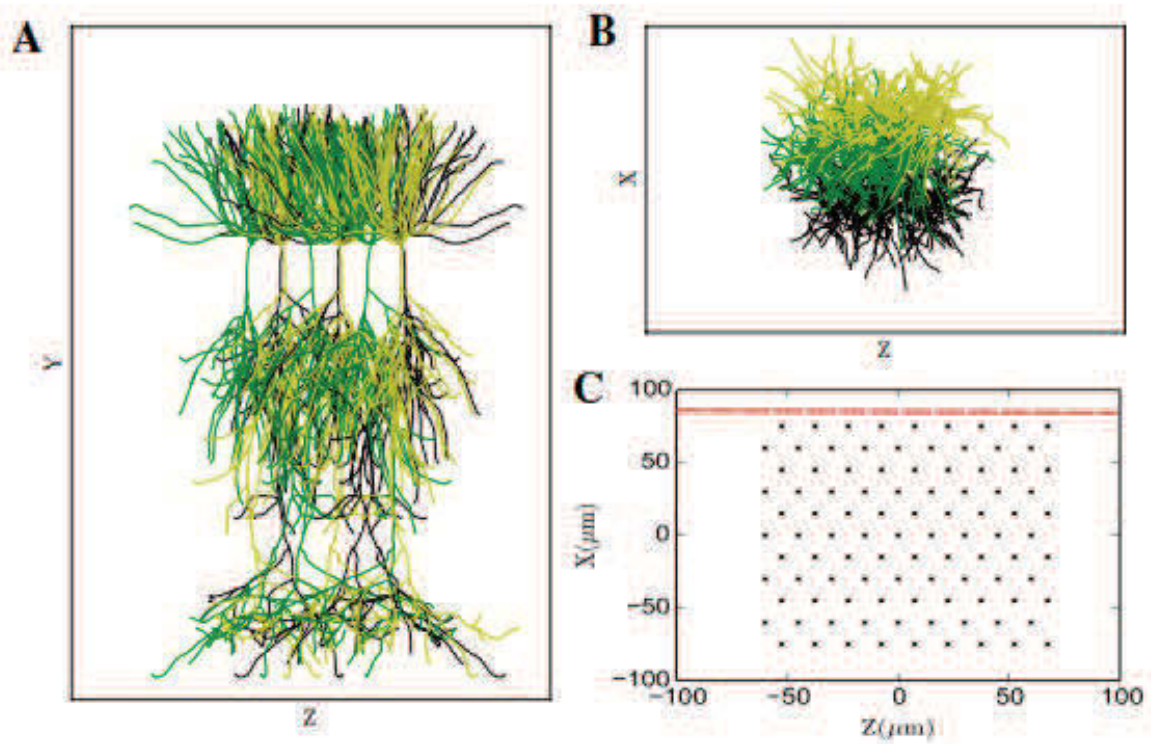

Figure 1.12: Sketch of the ensemble of neurons (only a fraction of the 100 neurons is plotted). A). View of the population on the y-z plane; a randomly rotated copy of the neuron used in the single neuron simulations is regularly placed on the x-z plane. B). View from the top. C). Positions of the center of the somata on the x-z plane, each soma has a diameter of around 10 μm and the distance between somata is equal to 5 μm. The red dashed line represents the y-z plane on which the MF is calculated. *Courtesy F. Barbieri.*

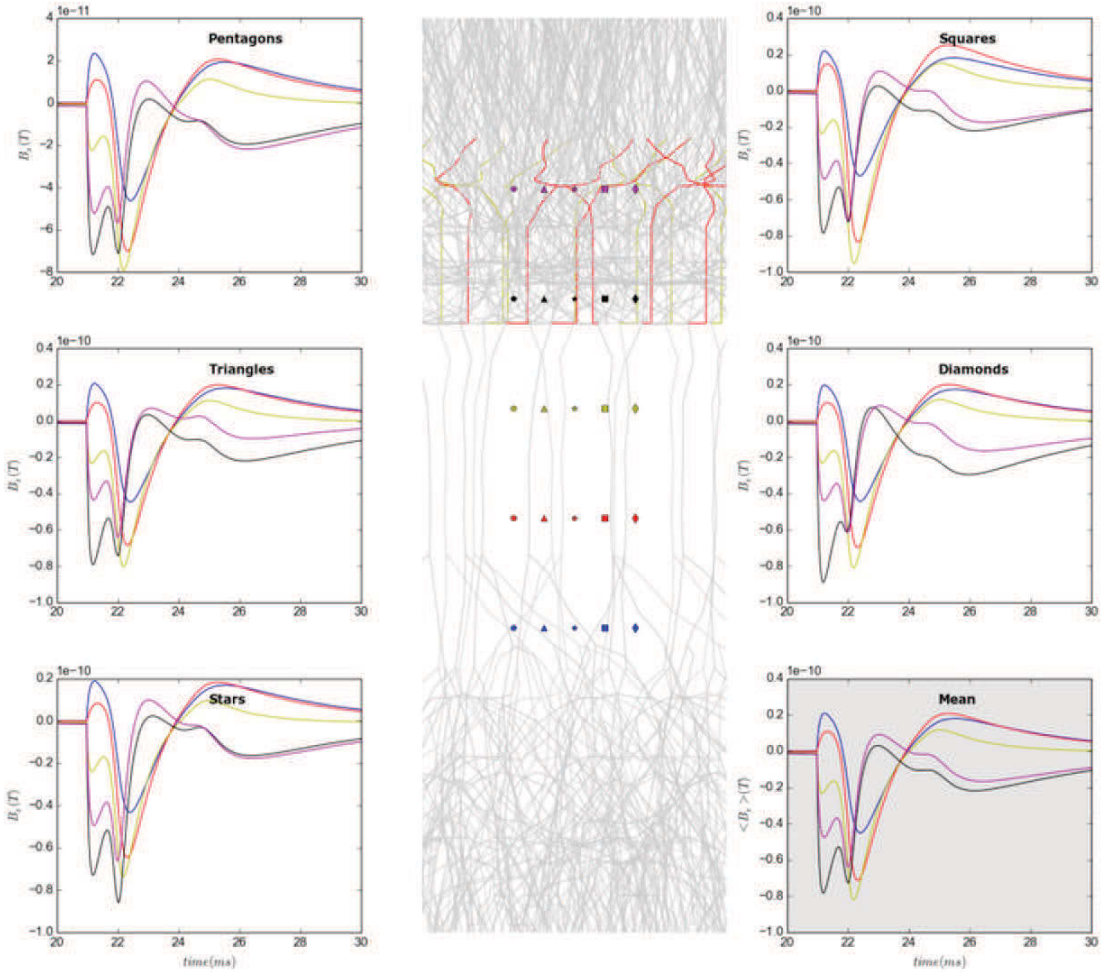

Figure 1.13: z component of the field produced by a population of 100 neurons synchronously firing a spike after stimulation. The grey panel shows the average field over 40 µm which corresponds to the length of the magnetic probe.

1.3.3.4 Analysis of the models

Different models in the literature since the first ones [39, 40, 34] are all giving the same time dependence of the signal, duration of 0.5 to 2 ms and shapes. In terms of amplitude, we still observed a discrepancy between different models. Our basic model is taking the same parameters than the Barbieri model and gives the same magnitude of fields. Other models give larger signals, up to one order of magnitude larger, which can be explained mainly by a difference in size taken as the effective current is varying as the square of the diameter. These amplitude and time dependence will be compared to our experimental results in the

next chapters.

However, these models have a number of limitations.

The first one is the accuracy of some parameters. For example, the internal conductivity of the neurons varies in the literature from 100 Ω.cm to 200 Ω.cm [44]. The second one is how to take into account correctly the extracellular currents.

To highlight this last point, we may calculate the field created by our 1000 neurons at 3 cm of distance and we obtained 90 fT if we do not take into account extracellular currents. This is the typical size of a MEG signal amplitude but if we introduce the extracellular currents and consider a rather focused localization of the extracellular currents, this would give a non measurable signal at 3 cm. A number of models for MEG signals are taking a larger number of sources, typically 10 000 to 30 000 to explain the measured signal as they introduce a partial screening of the signals. The third limitation of the models is related to synchrony which may reduce the size of the effective signals.

1.3.4 Conclusion

The advantages of measuring magnetic fields is to be reference-free (it is a direct measurement of the current signature and not a difference of potential measurement), to be totally non-disturbing and to avoid direct contact with the tissues.

Compared to electric probing, magnetic probing can be achieved at several locations on the same probe, leading to temporal information both on transmission and location, as well as opening the way to synchrony or coherent phenomena. Magnetic measurement does not require a reference point, and when mounted in array of several sensing elements on the same probe, leads not only to scalar information, like in the potential recordings, but as well to vectorial information of the currents. Furthermore, temporal magnetic response is not limited by capacitive effects and extremely fast events may be detected. However, we have seen from the various models that magnetophysiology at local scale requires very sensitive sensors. We are presently not able to detect a single neuron activity without averaging either on a large number of neurons, at least 100, or by averaging on time which requires a trigger on an external stimulus.

Chapter 2

Magnetic sensors

2.1 Magnetic sensors for biomedical applications

2.1.1 Magnetic field amplitudes

Magnetic field can be generated by a magnetized entity (permanent magnet, magnetized ferromagnetic material, magnetic nanoparticle...) or by an electric current. The magnitude of the corresponding field depends on the strength of the magnet or of the current, and to its distance to the sensing location. The following figure (Figure 2.1) shows the magnitude of various objects or various electric signals, including the magnetic signature of biomagnetic fields when recorded at the surface of the body. As discussed in Chapter 1, the electrical activity of activable cells (cardiac cells, muscles, nerves, neurons) gives rise to a corresponding magnetic field. These biomagnetic signals have usually very weak amplitude, and can only be recorded non invasively when a coherent signal, due to a large number of cells are activated together and in a certain direction (otherwise the signal is spatially averaged to zero). Magnetic cardiac signals and brain signals are typically of the order of few tens of pT and tens or hundreds of fT respectively.

Detection of magnetic signals can be achieved with an adapted sensor, whose field detection level should be in the range of the signal of interest. Figure 2.1 shows a scale with various signals strength together with various types of sensors according to the sensitivity range. But sensitivity is not the only parameter for the choice of a sensor, and in the next section are discussed the relevant parameters for biomagnetic signals detection.

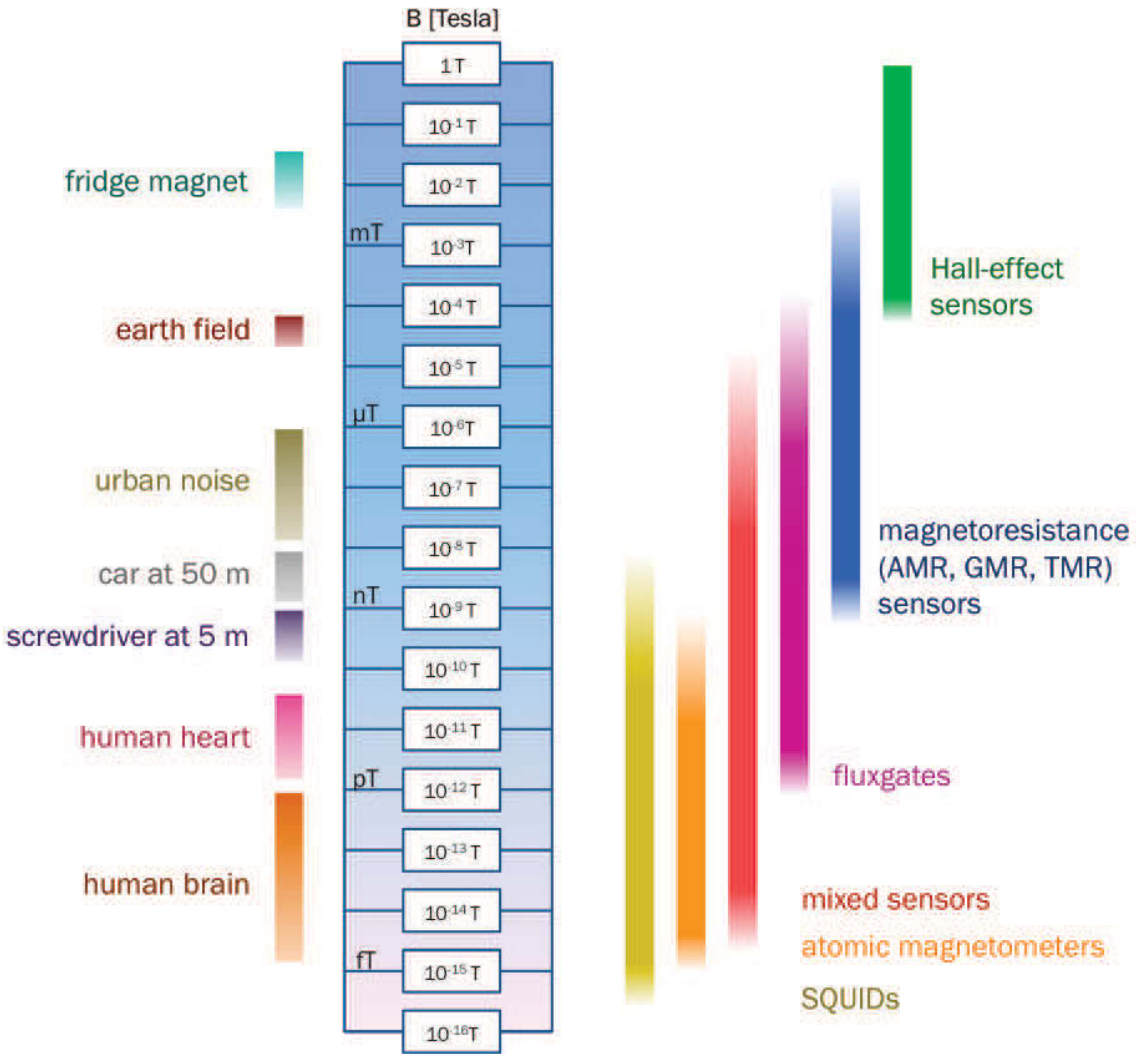

Figure 2.1: Magnetic field magnitudes (in tesla) and magnetic sensors adapted to record those signals.

2.1.2 Magnetic sensors for biomedical applications

Biomagnetic signals are characterized by low magnitude and low frequency (DC - few kHz) signals. In general, the choice of the sensor is driven by the nature of the sources and the signal of interest.

Proper sensors for biomagnetic signals are chosen according to the following parameters:

- Source characteristics (point-like or distributed, dipolar, quadrupolar...)
- Distance between the source and the sensor (which leads to the amplitude of the signal

at the sensor location)

- Allowable size
- Environmental conditions (in air for a non-invasive recording or in the conductive medium of the tissues for invasive recordings)

Biomagnetic signals when recorded non invasively, like in MEG or MCG, are distant to the source, exhibit low amplitude and can allow centimeter size sensor.

On contrary, local biomagnetic recordings, as those targeted in this work, are defined by a closer distance to the signal source, and therefore larger amplitudes signals, even though not expected to be larger than few nT; they required miniaturized sensors to fit to the small structures studied and limits the damages due to the penetration in the tissues. The sensor should also operates at physiological temperature and be compatible to the tissues environment, *i.e.* does not contaminate the living tissues with toxic materials, neither be corroded by the ions and natural chemicals of the tissues.

For non-invasive recordings, ultra-sensitive magnetometers should be used to allow recordings with a reasonable number of averages. The two main types of magnetic sensors are field sensors and flux sensors. Flux sensors sensitivity is proportional to the effective surface over which the field is applied (on SQUIDS, usually a pickup coil that contains several turns is used; the effective surface is the mean surface area times the number of turns, and the flux to consider is also depending on the inductance of the pickup coil), and though large surface sensors can offer a very high sensitivity. SQUIDs and atomic magnetometers are the main sensors used for MCG and MEG recordings.

2.1.2.1 SQUIDs

Superconducting QUantum Interferences Devices (SQUIDs) are ultra-sensitive magnetometers that can detect magnetic fields in the subfemtotesla range ($<10^{-15}$ T). Based on superconducting loops that contain Josephson junction, SQUIDs require a cryogenic environment due to superconducting properties; thus, SQUIDs are cooled down at very low temperature (4 K). The field of interest disturbs the current within a pick up superconducting loop, directly coupled to the SQUID. The flux is detected through a variation of the supercurrent running into the SQUID, which comprises a superconducting loop interrupted by one or two non-superconducting tunnel junction, called Josephson junctions [45, 46] (Figure 2.2).

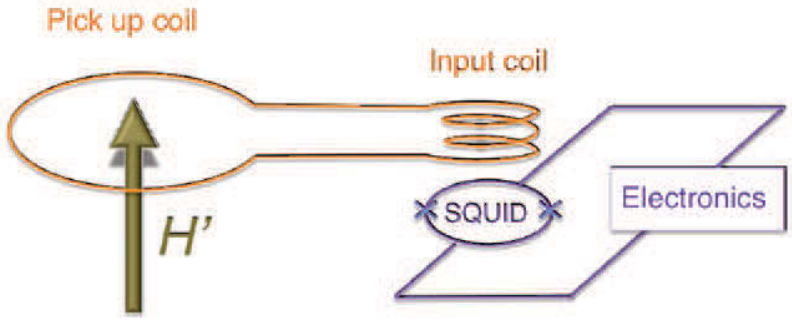

Figure 2.2: Principle of SQUID measurement. The field of interest is captured in a pick up coil which is coupled to a second loop (primary coil) directly coupled to the SQUID. Such flux transformers are made of superconducting materials, as well as the SQUID, which is a superconducting loop interrupted by Josephson Junctions, which are tunnel junctions or weakly superconducting areas. Both flux transformer and SQUIDs require a cryogenic environment to operate below the T_C of their superconducting material. Usually SQUIDs are used with a flux locked loop scheme which allows operating in the most sensitive part of the output voltage. (From [47])

SQUIDs are used since the 1970's for MCG and MEG [48] and commercial systems now allow MEG mapping on an array of more than 300 channels. SQUIDs have also been used for biomagnetic signal recordings of giant axons, nerve or on slice, but their large surface does not permit local recordings and the cryogenic temperature imposes the use of a cryostat which limits the distance to the source to few mm at best [33].

Though MEG signals recordings are widely used for neurosciences or clinical studies and are giving one of the main source of information on the magnetic signals generated by the brain neuronal activity.

2.1.2.2 Atomic magnetometer

Atomic magnetometers can detect magnetic field at room temperature in the femtotesla range (figure 2.1). The principle is based on an optical detector that measures the spin polarization variation of alkali atoms under a magnetic field while a laser diode light the atoms vapor. A first laser (pump laser) polarizes the alkali atoms. The atoms polarization is changed by the magnetic field, and this change in polarization can be detected through the absorption of the light of a second laser (probe laser) through the vapor cell (Figure 2.3).

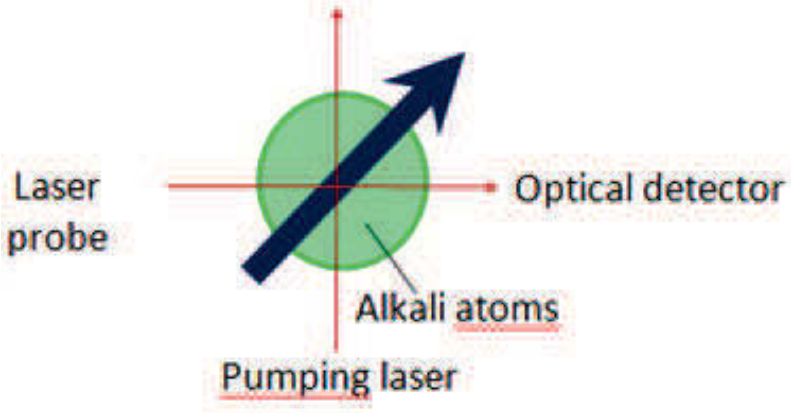

Figure 2.3: Principle of an atomic magnetometer.The pumping laser polarizes the alkali atoms and the laser probe is partially absorbed when an external magnetic field (blue arrow) is applied to the alkali atoms. Under magnetic field, electron spins precess and the light transmitted through the atoms vapor is reduced and is detected by the optical detector.

A new type of atomic magnetometers has been developed since 2003 [49] allowing an increased field sensitivity by the limitation of decoherence due to the spin relaxation. These SERF-magnetometers have allowed MCG and MEG recordings [50, 51, 52, 31]. One limitation is the strong magnetic shielding needed to operate the sensor in its linear response range and even if chip-scale magnetometers have been developed, their size is still in the few mm^3 range [53, 54].

One can also note that SQUIDs are vector sensors, sensitive to field applied perpendicularly to the pick up coil (*i.e* in the out of plane direction), whereas atomic magnetometers are scalar magnetometers.

Although these two types of sensors exhibit very good sensitivity of field and are successfully used for non-invasive recordings, they are not fitted to the requirements of local recordings within the tissues.

For local biomagnetic recordings, the chosen technology, which fulfills the specifications of micrometer size, very good sensitivity (hundreds of pT to nT range) and room temperature operation, is spin electronics. The choice has been to use Giant Magnetoresitive sensors, which are described in the next section.

2.2 Magnetoresistive sensors

A magnetoresistive sensor is a sensor whose resistance changes as a function of the applied magnetic field. The first type of MR sensor is Anisotropic Magneto-Resistance (AMR) sensor, which exploits the relative orientation of the current and of the magnetization [55]. More recently spin electronics physics has opened the way to new MR sensors, with higher sensitivity and small size.

2.2.1 Spin electronics

Electrons carry two types of angular momentum: the orbital angular momentum, due to its motion around the nucleus, and an intrinsic momentum, the spin. Magnets illustrate in a macroscopic way the effect of the spin orientation: in a ferromagnetic material, all the spins tend to align in parallel to each other's. The main purpose of spin electronics (« spintronics ») is to combine both the charge and the spin of electrons to make devices in which those two characteristics will play an active role.

The evolution of microfabrication techniques has made possible the development of systems smaller than the spin-diffusion length, the mean distance over which the electron can travel before its spin flips (tens of nanometers at room temperature). In such systems, two independent channels of conduction appears (Mott's model, 1936), according to the direction of the spin (up or down). The total current can be seen as the sum of each current flowing through those two channels.

In a ferromagnetic material, the electric conductivity is linked to the mobility of electrons at the Fermi level, which is different for the two spin states of electrons. In cobalt for example, the density of state at the Fermi level is more important for the spin-down polarized electrons, which means that they will undergo many more collisions, hence the resistivity of spin-down polarized electrons will be much greater than the one of the spin-up polarized (cf figure 2.4).

This phenomenon is the basis of the Giant Magneto-Resistance (GMR) effect, obtained by depositing successive layers of ferromagnetic materials. First GMR effect has been observed in 1988 by Baibich et al [56], and has been rapidly implemented in computers' read heads to replace AMR sensors, thanks to their better sensitivity and micrometer scale [57]. GMR sensors are field sensors and conserve their sensitivity when reducing the sensor's size, making them very attractive in applications where small sizes or large density is required.

Another type of spin electronics sensor, called TMR (for Tunnel Magneto-Resistance) sensor has been demonstrated in 1975 following the theoretical predictions of Julliere [58],

exhibiting large MR, but which field sensitivity at low frequency not better than GMR because of its higher low frequency noise.

2.2.2 Spin Valve -Giant MagnetoResistance

If GMR has been first demonstrated in multilayer structures, alternating magnetic and non magnetic very thin (nm range) layer, this type of structure is not ideal for a sensor application since the MR varies over a large field range, and thus does not exhibit the highest sensitivity. We will therefore focus here and the specific GMR structure chosen for magnetic field sensor application, discovered by Dieny in 1991 [59], the Spin Valve (SV) structure.

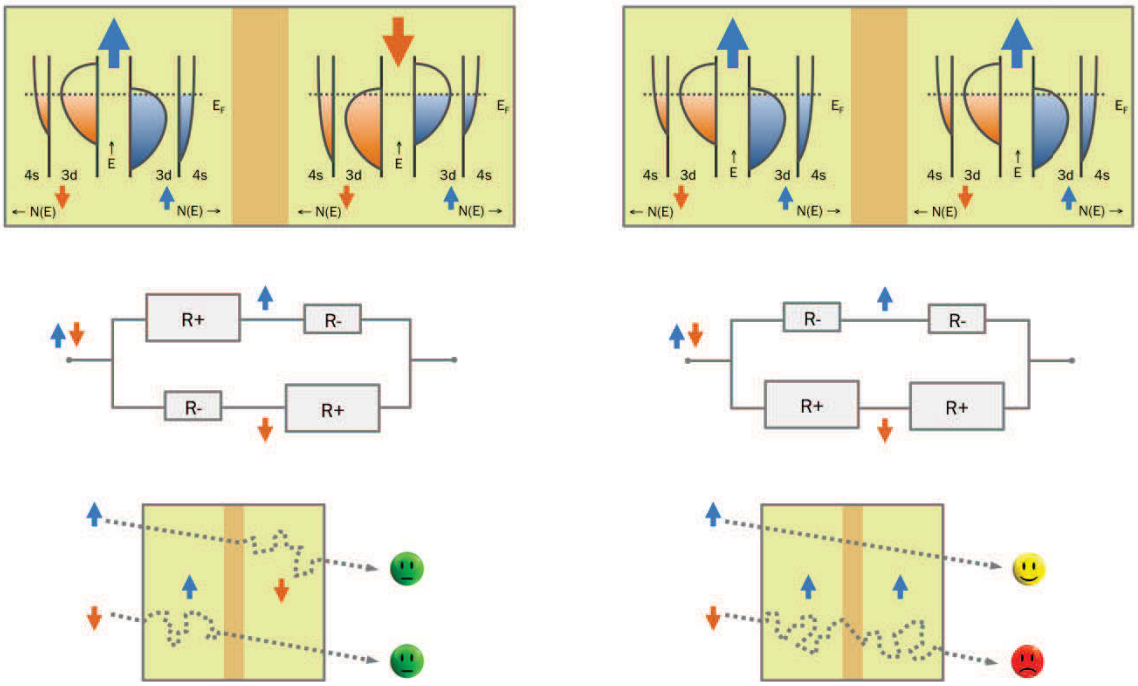

Figure 2.4: Schematics of the spin transport between two ferromagnetic layers separated by a non-magnetic spacer (in orange). On top, the band structure for both spins up and spins down when the ferromagnetic layers have oppposite magnetization direction (left) or same magnetization direction (right). Middle: resistance equivalent model in both case for both spins of the electrons. Bottom: easier transport of the electrons in the anti-parallel magnetization case (left) and on the paralle case (right). Courtesy Paolo Campiglio.

A simple SV (Figure 2.4) consists of a sandwich structure of two magnetic bi-layers separated by a non-magnetic metallic material[1] (copper being the most commonly used).

[1]note that in TMR, the metallic spacer is replaced by an insulating layer, through which the conduction

One of the bilayer has a fixed magnetization, so-called pinned layer (or reference layer), which is obtained by the direct coupling of a CoFe ferromagnetic layer, which exhibits a large spin polarization, an antiferromagnetic (AF) layer.

The in-plane applied field acts on the free layer magnetization, which is composed typically of a bilayer of CoFe and of NiFe, a very soft ferromagnetic material, which, by coupling, will rotate the magnetization of the CoFe for very low applied field. The spin transport depends then on the relative orientation of the pinned and the free layer. When the two magnetizations are in opposite directions, the resistance is at its maximum, and becomes minimal when the two magnetizations are along the same direction, where the spin transport is the most facilitated.

To create a linear response range between these two states, one induces either during the stack deposition or by patterning the sensor's shape, a field anisotropy in the free layer at 90° in plane from the magnetization direction of the pinned layer.

Therefore at zero applied field, the resistance of the spin valve is at its mean value (R_0), and the application of a field in the pinned layer direction will result in magnetization rotation towards the parallel or anti-parallel magnetization direction, and to a corresponding linear decrease or increase of the resistance. This configuration gives a rather linear response around zero field, on a field range which is linked to the field anisotropy, and for instance to the aspect ratio of the sensor. An example of the R(H) response of SV-GMR sensor is shown in Figure 2.5.

---

electrons tunnel.

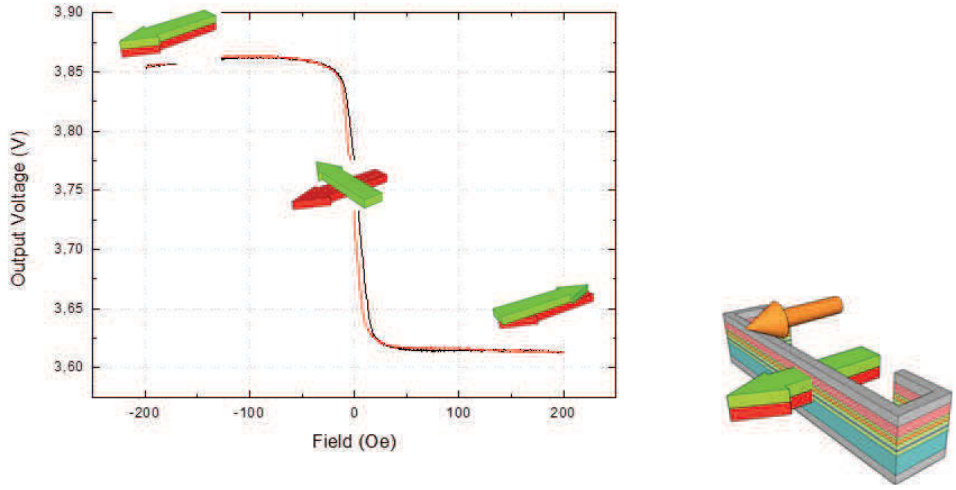

Figure 2.5: A typical $R(H)$ curve of a sharp magnetrode (#M11g). GMR is patterned as a yoke shape contacted by two points. The resistance R_0 is 250 Ω with a MR ratio of 4.48 % and a sensitivity of 1.2 %/mT. The red arrow does represent the hard layer while green arrow the free layer of the yoke. The external magnetic field applied (orange arrow) coming from a current source is parallel to the hard layer.

2.2.2.1 Sensor Magneto-Resistance (MR) ratio and sensitivity

The magnetoresistance ratio (MR) of the GMR which is given by the variation between the ratio of the antiparallel resistance R_{AP} and the parallel resistance R_P :

$$MR(\%) = \frac{R_{AP} - R_P}{R_0} \cdot 100 \tag{2.1}$$

where R_0 is the mean resistance defined as:

$$R_0 = \frac{R_{AP} + R_P}{2} \tag{2.2}$$

The sensitivity s of the GMR element is defined as the resistance change (%) per field unit (T or mT) at zero field (corresponding to the slope of the response $R(H)$) that can be expressed as:

$$s = \frac{1}{R_0} \cdot \frac{\Delta R}{\Delta H} \tag{2.3}$$

Typical MR ratio of SV-GMR are of the order of 5 to 10 % whereas sensitivity is ranging from 1 to 15 %/mT.

2.2.3 SV sensor

2.2.3.1 Sensor shape

GMR sensors, especially spin valve sensors, offer a wide variety of applications in many areas, in which the sensor design is a key feature to fulfill the specifications linked to the targeted application, from a single line pattern to very complex size and shape patterns [60][61]. The linearity response of the sensor is one of the required characteristic to avoid any multiple magnetic domains formation. Sensor linearity is guaranteed if all the magnetic domains contained in the ferromagnetic layers of the spin valve rotate uniformly with the applied external magnetic field.

The linearity of the sensor response is linked to the way an anisotropy field is created at zero applied field on the sensor. This can be achieved by an external magnet, or this can be achieved on small size sensor by the shape anisotropy. Additionally, one has to insure an homogeneous rotation and a monodomain soft layer. When an external field is applied with a magnet, the magnetic domains are stabilized, but in the case where shape anisotropy is used, one has to realize a structure free of magnetic domains inhomogeneity [62].

Two structures are good candidates for this. “Yoke” shape can be chosen for the GMR element. Micromagnetic simulations have shown (Figure 2.6) that along the main axis of the yoke shape, the ferromagnetic layer is rotating as a single magnetic domain, whereas the magnetic domains are confined to the corners of the structure [63] (cf Figure 2.6). These complicated magnetic configurations in thin films are due to the competition between the internal dipolar interactions (field created by an atom on another one) which tend to form domains and the exchange interaction which tends to align all the atoms in a ferromagnetic material. To ensure the linear response of the sensor with this type of shape, one has to place the contacts such as only the main arm of the GMR is measured, leading to a R(H) response free of jumps due to magnetic domains flipping. Figure 2.5 shows a centered, linear and without hysteretic behavior response which are key elements for low field detection.

Another possible structure is a meander short cut at the edges (Figure 2.7). As for the yoke shape, the magnetic inhomogeneities are located on the corners of the meander, and the shortcut forces the injected current to run in the metal layer of the pads; the R(H) response is then free of jumps.

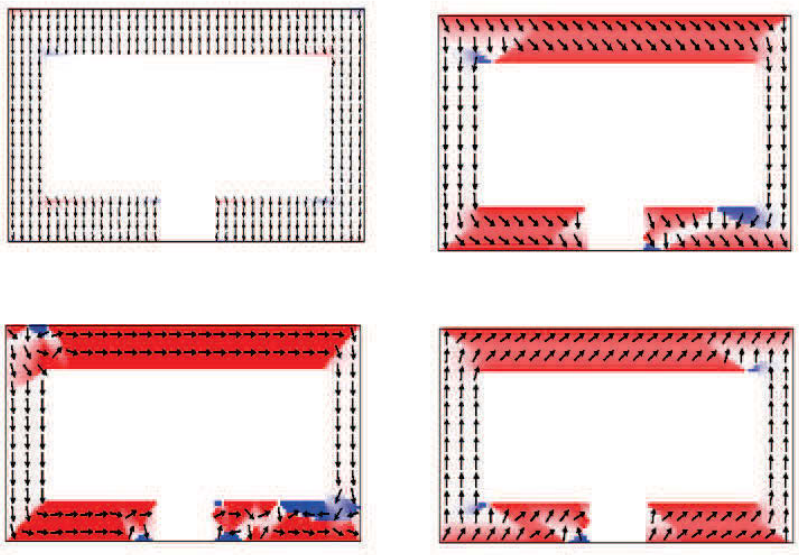

Figure 2.6: Evolution of the magnetization in a yoke for four external applied magnetic fields (-10 mT, -1 mT, 0, 1 mT). Arrows indicate the direction of the planar magnetization while colours indicate the momentum out of plane (typically 1°). This configuration is calculated by a micromagnetic software (*oommf*). Adapted from [63]

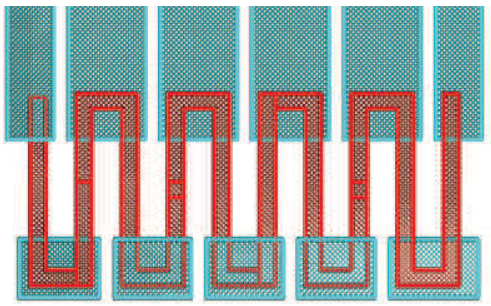

Figure 2.7: GMR meander shape with 10 segments, short-cut at the edges where magnetic domains inhomogeneities are located. The light blue lines are the contacts and the red lines the meander. The current passes through the GMR segments where the magnetization rotation is homogeneous. .

In these two configurations, the magnetic domains inhomogeneities extension depend on the size of the sensor, and sensors larger then 5-6 µm can show some non-linearity in their responses.

2.2.3.2 Contacts

The GMR sensor output can be collected with two configurations. In the first configuration, the current is sent from one of the magnetic bilayer (PL or FL) through the copper layer to the other magnetic bilayer. This is the CPP (for Current Perpendicular to Plane) measurement, where the highest MR ratios are obtained, but which requires a lithographic process with two levels of contacts electrodes deposition, and which also imposes, because of the high conductivity of the copper spacer, very small size sensors to achieve resistance of more than few Ohms. This configuration is chosen for TMR sensors where square resistance is much higher.

The second configuration - which has been chosen in this work- is the CIP (Current In Plane) where the current is sent from electrodes deposited both on top of the surface, on the edges of the structure, and where the current flows in the stack's plane. This configuration is easier to realize on microprocessing, and the resistance of the element is directly linked to the length l and width w of the structure.

In this work, magnetrode sensors (yoke or meander shape) are contacted by two pads contacts: the DC bias current and the output voltage are sent and measured simultaneously.

Another type of GMR sensor characterization can be achieved by four-points contact measurement: the current I_B is sent into the yoke extremities and the output voltage is measured in the linear part of the yoke (figure 2.8). This method suppresses the contribution of contacts resistance, however it has not be used for magnetrode sensing measurement; for the planar probes because the contacts surface was large enough to ensure a negligible resistance compared to the sensor resistance, and in the sharp probes because the allocated space for contact pads was very small (see Chapter 3).

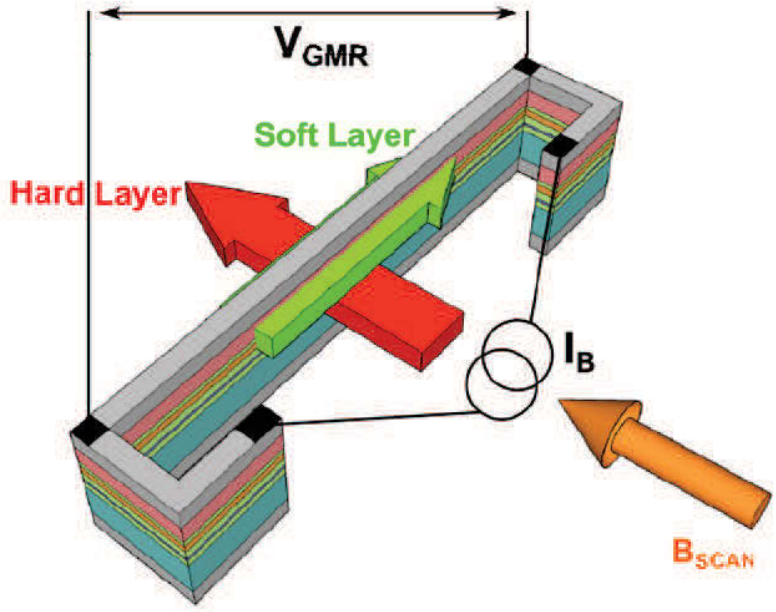

Figure 2.8: Four-points contact measurement of a yoke. B_{scan} is the external applied field. The current $I_B$is sent at the edges of the yoke and the output voltage V_{GMR} is measured in the linear region of the yoke. Adapted from [64]

2.3 Noise sources

Noise is a fundamental and unavoidable phenomenon in physics and electronics. Noise corresponds to random fluctuations of a macroscopic quantity (such as the output voltage of a sensor) around its mean value and is present in all electronic devices (active or passive components). This value can be evaluate and characterized to quantify the Signal-to-Noise Ratio (SNR) of a device.

V_T is defined as a fluctuating quantity (over a time window of T), that is measured in magnetic sensors noise characterization (sensor output voltage):

$$V_T = \frac{1}{2\pi}\int_0^{\mathrm{T}} V(t)e^{i\omega t}dt \tag{2.4}$$

where ω is the frequency.

The power of the signal V_T is given by:

$$P = \lim_{T\to+\infty}\frac{1}{T}\int_0^T |V(t)|^2\,dt \tag{2.5}$$

Usually used in the frequency domain by Parseval theorem:

$$P = \lim_{T \to +\infty} \frac{2\pi}{T} \int_{-T}^{+T} |V(\omega)|^2 \, d\omega \tag{2.6}$$

where $V(\omega)$ is the Fourier Transform of the signal $V(t)$. Hence can be deduced the Power Spectral Density (PSD) given in V^2/Hz and defined as:

$$S_V(\omega) = \lim_{T \to +\infty} \frac{2\pi}{T} |V_T(\omega)|^2 \tag{2.7}$$

2.3.1 Detectivity

Detectivity correponds to the field equivalent noise PSD, in other terms it is the voltage noise PSD $\sqrt{S_V}$ of the sensor given in $V/\sqrt{Hz}$ divided by s, the sensitivity given in V/T. It refers to a field for which the Signal-to-Noise-Ratio (SNR) is equal to one, allowing easy comparisons between sensors. It expressed as:

$$\sqrt{S_B} = \frac{\sqrt{S_V}}{s} \tag{2.8}$$

$\sqrt{S_B}$ is expressed in $T/\sqrt{Hz}$.

For instance, the field equivalent noise for GMR sensors is 20 to 100 $pT/\sqrt{Hz}$ [65].

Magnetoresistive sensors present several types of noise; at low frequency, the dominating noise sources are the thermal noise, the 1/f noise and the magnetic noise, which are described in the next section and represented in Figure 2.9.

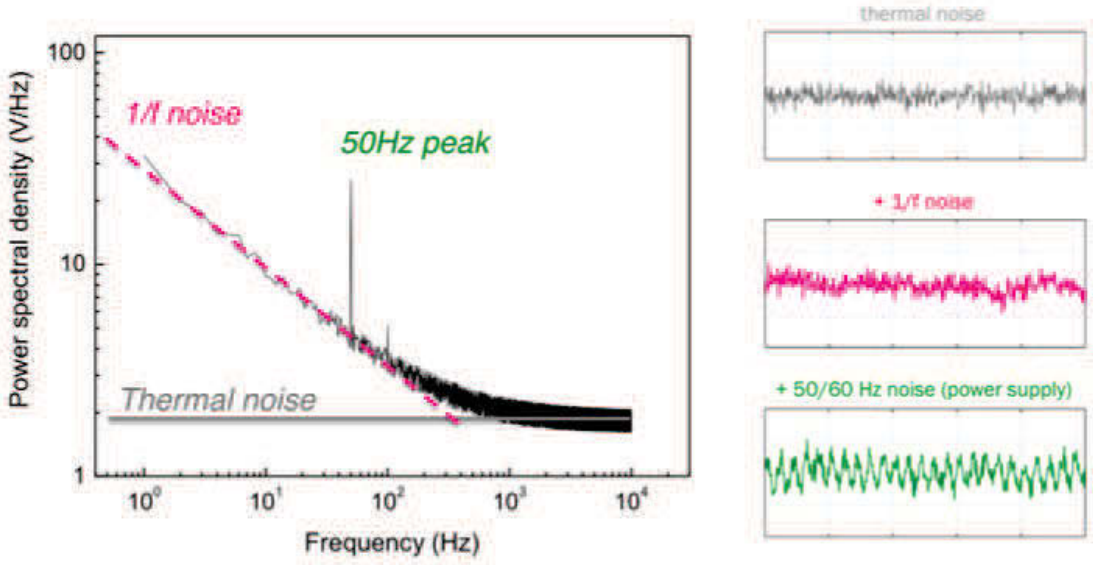

Figure 2.9: Voltage PSD as function of frequency.

2.3.2 Thermal noise (Johnson noise)

Thermal noise, also called Johnson-Nyquist noise [66], is characterized by thermal fluctuations of the charge carriers (here electrons) inside electronic devices regardless of the applied voltage or current. Johnson noise is a white noise meaning its frequency-independence.

The root mean square (RMS) voltage of the thermal noise V_{therm} in a resistance R in ohms (Ω) through a bandwidth Δf in Hertz (Hz) is given by:

$$V_{Therm} = \sqrt{4k_B T \cdot R \cdot \Delta f} \tag{2.9}$$

where k_B is the Bolztmann constant expressed in Joules per Kelvin ($k_B = 1,38{\cdot}10^{-23}\text{J.K}^{-1}$), T the temperature. For a bandwidth Δf of 1 Hz the voltage PSD of thermal noise can be expressed as:

$$S_v(\omega) = 4k_B T R \tag{2.10}$$

Thermal noise has no magnetic origin and no dependence in bias voltage sensor and it cannot be suppressed except by changing the temperature or the resistance of the sensor.

2.3.3 1/f noise (Flicker noise)

The 1/f noise refers to a frequency decreasing noise that follows a 1/f power law. It is present in all fluctuating systems such as geological and biological phenomena. 1/f noise is dominant at low frequencies and it constitutes a drawback in performances for MR sensors (GMR and TMR).

In GMR sensors, the 1/f noise arises from resistance fluctuations, it is thus dependent of the applied current within the GMR. The PSD of the 1/f noise is inversely proportional to the volume of the sensor and this can be explained by considering R the resistance of the GMR as the sum of N small resistances r (i.e $R = N \cdot r$); the fluctuations of R are $\sqrt{N}$ larger compared to the ones from r, therefore GMR fluctuations with a resistance R are following a law as the inverse square root of the volume ($\frac{1}{\sqrt{N}}$,i.e $\frac{1}{\sqrt{V}}$). The PSD associated to the 1/f noise is phenomenologically [67] defined as:

$$S(\omega) = 2\pi \frac{\gamma_H (R \cdot I)^2}{N_c \cdot \omega} \tag{2.11}$$

where γ_H is the Hooge constant, $R \cdot I$ the voltage across the sensor and N_c the number of charge carriers.

TMR sensors have a typical sensitivity 20 times higher than GMRs but the 1/f noise is also larger by the same amount. The noise in GMR is mainly the noise found in any metallic wire of the same size but the noise in TMR is mainly due to a tunnel barrier noise [68] which may be huge. At low frequencies, detectivity of present state-of-the-art GMRs and TMRs are comparable.

2.3.4 Random Telegraphic Noise (RTN)

Random Telegraphic Noise corresponds to fluctuations between two or several discrete levels with comparable energies to the presence of defects in the conductor. This is usually the main source of noise in semi-conductors. In MR sensors, these fluctuations originate mainly from the soft layer, where domain walls can be formed and thus several energetic configurations appear, inducing resistance fluctuations between the states.

In small size GMR sensors, defects become dominant and RTN noise can appear: (cf chapter 3, sharp magnetrode). These jumps are strongly dependent of the temperature, field and the applied bias current.

2.3.5 Magnetic noise

Magnetic noise can be present in all magnetoresistive structures [69], it is characterized by magnetic domain wall formation and motion in the soft layer in small thin film structures.

In GMR sensors, magnetic noise can be either observed as small jumps in the non-saturated parts of the R(H) GMR response (cf 2.2.2) but also on the PSD response during noise measurement. A way to detect and quantify this noise is by applying a magnetic field on the GMR (with the bias magnet), strong enough to reach the saturation regime. In this case, the noise disappears from the PSD response and a comparison between both with and without magnet can be performed. This kind of noise appears often as RTN magnetic noise on the spectrum.

This magnetic noise contribution in GMR spin valves can be strongly reduced by stabilizing magnetically the main part of the GMR sensor, by a yoke shape for instance, as previously detailed.

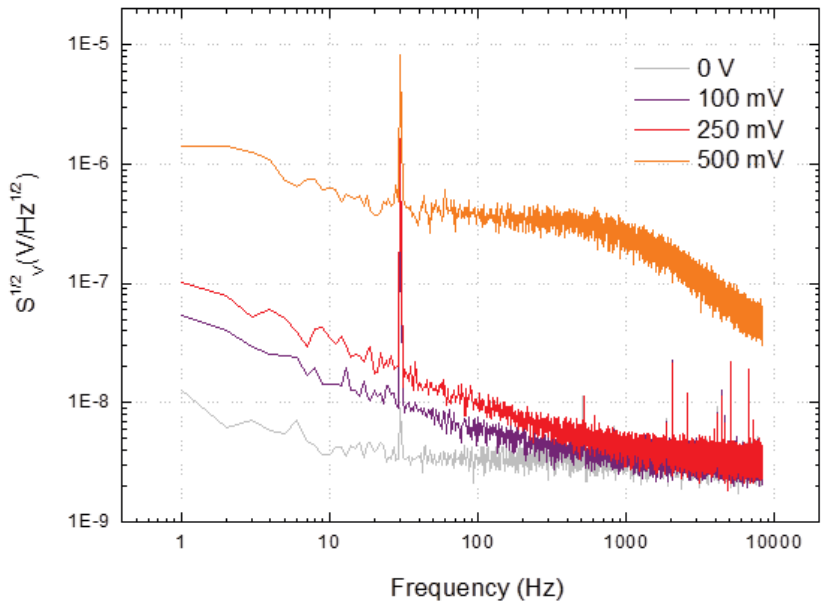

Figure 2.10: Voltage PSD as function of frequency at different voltages for a sharp magnetrode (cf chapter 3) patterned as a yoke shape (4x40 µm). Note the presence of magnetic RTN at 500 mV bias voltage in the GMR.

2.4 Conclusion

Biomagnetic signals have been so far detected with the help of large size, very sensitive devices such as SQUIDs and atomic magnetometers. In order to record a small scale biomagnetic signal, one has to choose a technology associating small size and high sensitivity at room temperature.

Spin electronics is a principle on which magnetic sensing can be realized along these specifications. The chosen type of sensor is a SV-GMR sensor, with a MR ratio around 5 to 10 %, sensitivity of few %/mT and noise levels given by thermal noise and 1/f noise. These sensors appear as one of the most promising technology for the main purpose of this work. We will present in the following chapters the performances of fabricated probes.

Chapter 3

Magnetrodes

I will discuss in this chapter the development of the probes (magnetrodes) that we used for magnetic recordings. I will first present microfabrication techniques involved in probe fabrication (sharp and planar) and their characterization defined by intrinsic properties such as sensitivity and noise level. Two kinds of magnetrodes are presented: sharp and planar probes that record within tissues or at the surface level respectively, both tested on *in vitro* and *in vivo* conditions.

3.1 Probes fabrication

We designed two types of magnetic probes: the first are sharp ones allowing entering within the tissues, the second are planar probes that record at the surface of the tissues (cortex, muscle or slice). Figure 3.1 presents a schematic of both probes on *in vitro* (hippocampus's slice) and *in vivo* (cortex) experiments.

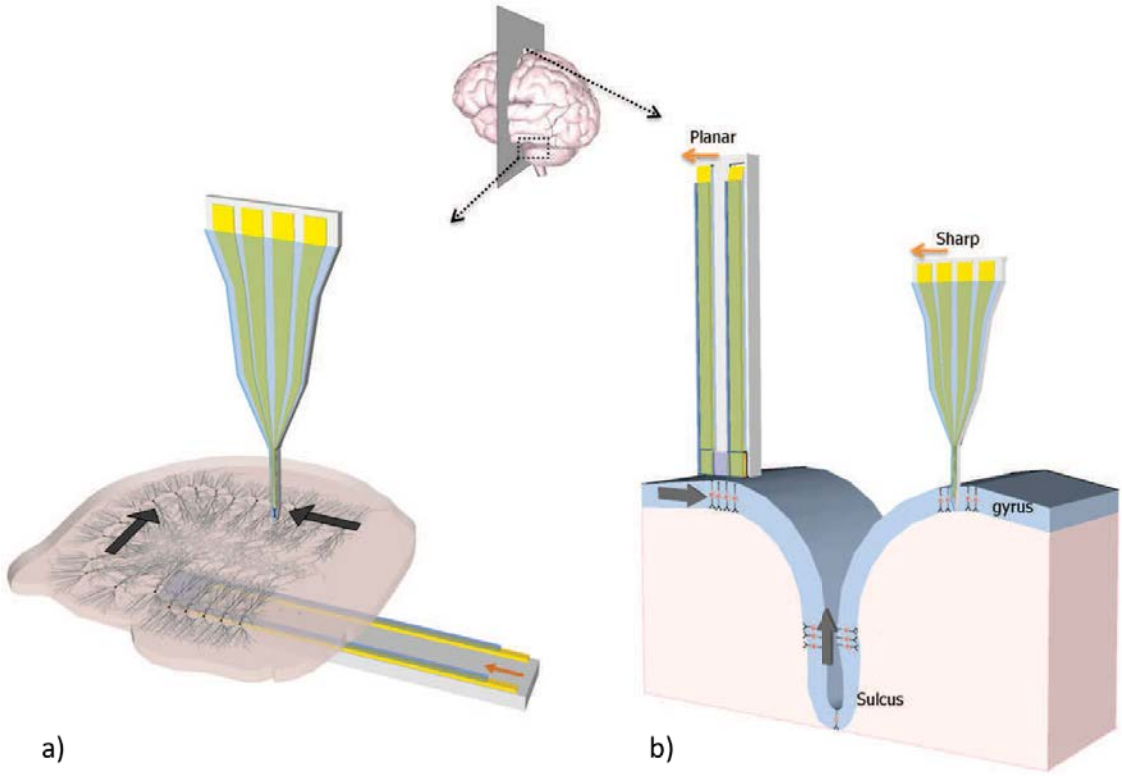

Figure 3.1: General scheme of experiments realized with the two types of probes: planar and sharp. a) *In vitro* recordings on a hippocampus slice (mouse). Planar probe (magnetoresistive sensor deposited on silicon substrate with gold contacts) are dedicated to record neurons network below the slice while sharp probes penetrate the slice to record within tissues. Black arrows represent magnetic field direction and orange arrows on planar probe show the sensitivity direction of the sensor. b) *In vivo* recordings (cat). Planar probe or ECoG and sharp probes for cortex experiments. Cortical neurons are perpendicularly aligned and produce a magnetic field around that is represented by black arrows. Depending on the position (either in the gyrus or in the sulcus), the magnetic field produced is recorded either at the surface or in deeper location within the cortex.

Sharp probes penetrate easily in tissues to be as close as possible to the sources (i.e ionic currents flowing within neurons). One of the disadvantages of getting close to the sources is that the sensing element size must be similar to the target (i.e neurons) meaning a small sensor surface (few μm^2) which increases the noise level at low frequencies (see 3.2). Moreover, needle shape (tip is 100 µm width) and thin substrate (from 100 µm up to 200 µm) make sharp probes technologically challenging and requires cautious manipulation.

On the other hand, planar probes microfabrication can be easily achieved since the tech-

nology is very well known (spin valve on standard silicon substrate) and the final probe shaping is a rectangle or a meander. In addition, planar probes do not penetrate into the tissues making no damage and are less invasive than sharp probes. The large volume of the probe (up to few mm^2) extends the field sensitivity and the noise level at low frequencies remains low (high SNR).

In the following section, sharp and planar magnetrodes design and microfabrication will be described.

3.1.1 Sharp probe

3.1.1.1 Probe design

Sharp probes were designed in a needle shape similar to electrode design used for electrophysiology [70, 71]. Several successive designs were used for the probe fabrication; containing either one or two GMR sensors (enabling gradiometric measurements) close to the tip of the probe, deposited on very thin silicon substrate (from 100 to 200 µm) in order to be less invasive as possible. The chosen substrate (silicon with an insulating silicon oxide layer) was a good candidate due to its standardization in GMR sensors deposition and its low price compared to other substrates like sapphire. GMR stack are generally deposited on large wafer substrate (6 to 8 inches) with a good planarity which easily foresee wafer thinning (mechanically and/or chemically)[72]. Silicon substrates used for sharp magnetrode are actually thinned down to the desired thickness by grinding either before or after the SV stack deposition.

Probe's tip size and sharpness were chosen according to electrophysiology probes dimensions as followed:

In vivo The length (2 mm) and the width (100 µm) of the tip were defined with respect to the size of the cortex (2 mm in the cat) and similar to classical electrophysiology cat's extracellular probes respectively. The penetration angle (18°) is the same than the one used for shaft electrodes [71]. GMR elements were patterned close to the tip of the probe (at around 50 to 100 µm) in order to sense signals coming from deep layers (layer IV/V) to higher layers neurons in the cortex (layer II/II). One of the main design constraints was to have a space large enough for contacting GMR element with respect to size characteristics. The space between the tip and the sensor was also an important characteristic to be taken into account: the sensor must be as close as possible from the tip to avoid more damage within tissues; several designs were drawn trying to reduce this space.

In addition to magnetic measurement by GMR sensors, an electrode made of platinum (Pt) or titanium/ gold (Ti/Au) is deposited next to the sensors to offer an electric measurement. Figure 3.3 shows one of the first sharp probes used for *in vivo* measurements.

One interesting new design would be to add one or several GMR elements in the upper part of the probe beneficial to gradiometer measurement or simultaneous recordings at different locations.

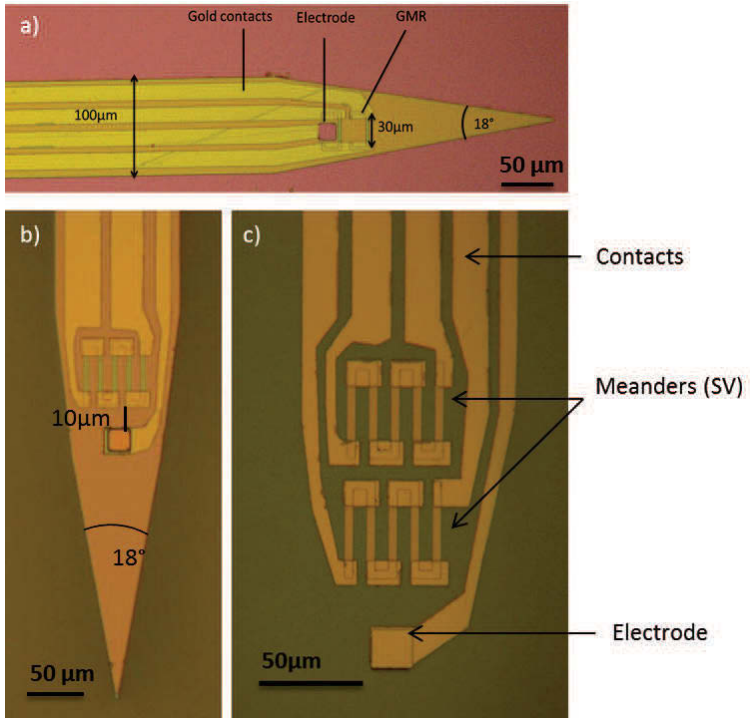

Figure 3.2: Sharp probes for *in vivo* recordings. a) First set of processed sharp probe (before cutting): two yokes (30x3 µm) contacted in two points with a common ground and an electrode point contact (Ti/Au). The penetration angle is 18° (#M8c) b) Single meander 30x4 µm with an electrode (the pink color on the electrode is a resist pads which has not been fully lifted off) (#M19Meldhau). c) Second set: two meanders 30x4 µm (short circuited at the edges by the same Ti/Au bilayer as the one used for the contacts) allowing to record in gradiometer configuration or two channels separately. A platinum electrode is deposited (see 3.1.1.5) (#M19 Petrucciani)

In vitro Two *in vitro* sharp probes were developed to record both close to the surface of the slice and inside the slice to get two different directions (tangential or radial to the

surface) of the magnetic field created by neurons network (see Chapter 4). The length of the tip is comparable in size to those used for *in vivo* and the substrate thickness is also of the order of 200 µm. One has a flat tip (#Peterson probe - Figure3.3a)) with the GMR element near the edge of the tip, enabling probe position at the top of the slice to record magnetic field in the tangential direction to the surface.

#Peterson probe does not contain an electrode because it is meant to stay at the surface of the slice. Another one has a sharp tip (#Parker probe - 3.3b)) with a larger angle than sharp *in vivo* probes since the penetration angle for slices does not need to be as sharp as for the cortex. Another key element design was to get the sensor element as close as possible from the tip, essentially due to the thin slice thickness (about 500 µm); several designs were tried so far to reduce this space, playing with the penetration angle as well as reducing contacts width. Figure 3.3 shows probe's dimensions.

New design are with flat probes containing more segments to record on larger length and some other ones with one meander instead of yoke.

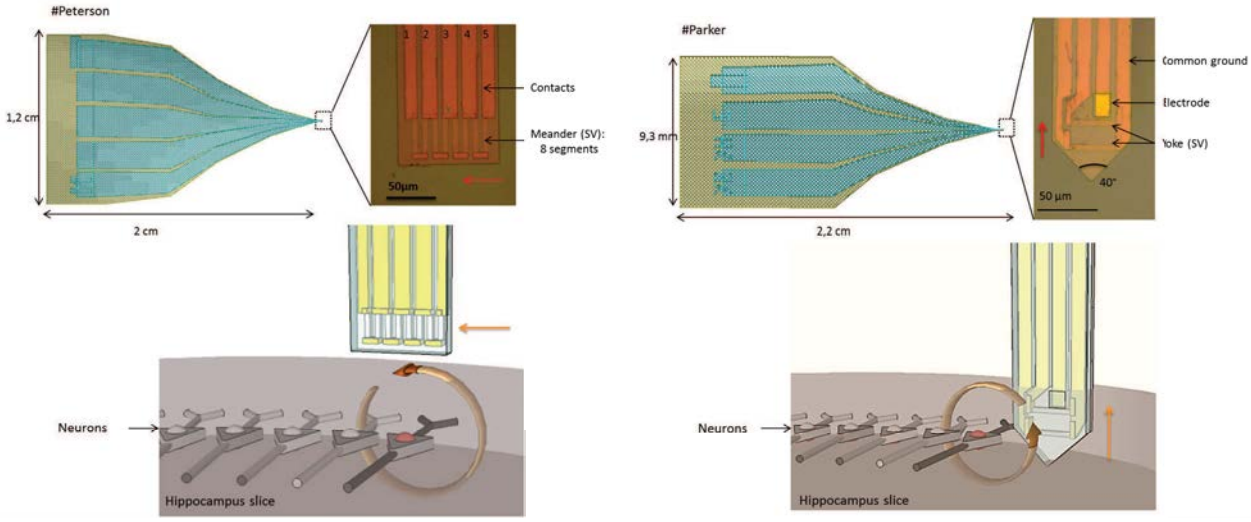

(a) #Peterson probe (b) #Parker probe

Figure 3.3: Sharp magnetrode for *in vitro* recordings. a) #Peterson probe: the GMR sensor (spin valve) is designed as a meander shape (6x40 µm) with 8 segments short-circuited at the edges. One can record either on the full length (between 1 and 5) or between segments part at the surface of the hippocampus slice. This probe can also be used for ECoG-like measurement *in vivo* b) #Parker probe: two yoke sensors are contacted with a common ground with an electrode (Ti/Au) close to the sensors (10 µm distant) to record within the tissues. The field sensitivity direction is indicated by the red arrow.

3.1.1.2 Sensor design

The first magnetrode designed was containing a 3 µm wide yoke, which was a bit too small in terms of sensitivity (cf Chapter 2 and section 3.3.2). Several GMR shapes were investigated to better achieve a good sensitivity with a large enough width to inject a strong current and a small volume of GMR to keep a size comparable with the target element.

The yoke geometry provides most of previously cited conditions but it does not permit to inject a strong current (1 mA max) due to its thin width (3 µm). To solve this point, I fabricated a second set of sharp probe with a meander shape of 4 and 5 µm widths.

The meander is short circuited by contact pads on the edge of each meander segments to avoid any magnetic domains formation that translate into magnetic noise. Additionally, a meander has a higher volume than a yoke, allowing injecting higher bias current (up to 3 mA) within the GMR. Picture 3.2b) shows a sharp probe with two GMR with a meander shape.

3.1.1.3 Probes microfabrication

Spin valve stacks Two SV types of stacks have been used for magnetrode processing: the first one (figure 3.4), deposited by INESC-MN is a simple SV, deposited on 150-200 µm silicon substrates. These stacks were used for the first sets of sharp magnetrodes, but their final sensitivity was shown to be too low to be used in the *in vivo* and *in vitro* recordings.

The second type of stacks is a Synthetic Anti-ferromagnet based GMR, deposited on standard 700 µm thick silicon substrate by AllegroMicrosystems. It has been used for the planar probe, and the substrate has been grinded down to 200 µm after stack deposition for the sharp probes.

Photolithography Photolithography is used to reproduce geometric patterns on a sample by using UV light passing through a mask. Patterns are defined on an optical mask made in quartz allowing UV light to shine through and opaque area made in chromium stopping UV light. All optical masks were designed with a homemade software and fabricated by an external company (Toppan). The sample is carefully cleaned with solvents then spin coated with a light-sensitive polymer resist (or photoresist) before being exposed to light. If the photoresist is positive, a developer removes the exposed area while areas hidden by chrome reveals desired patterns. All lithography processes developed for magnetrodes were done in the clean room of SPEC/Saclay and follow the steps below:

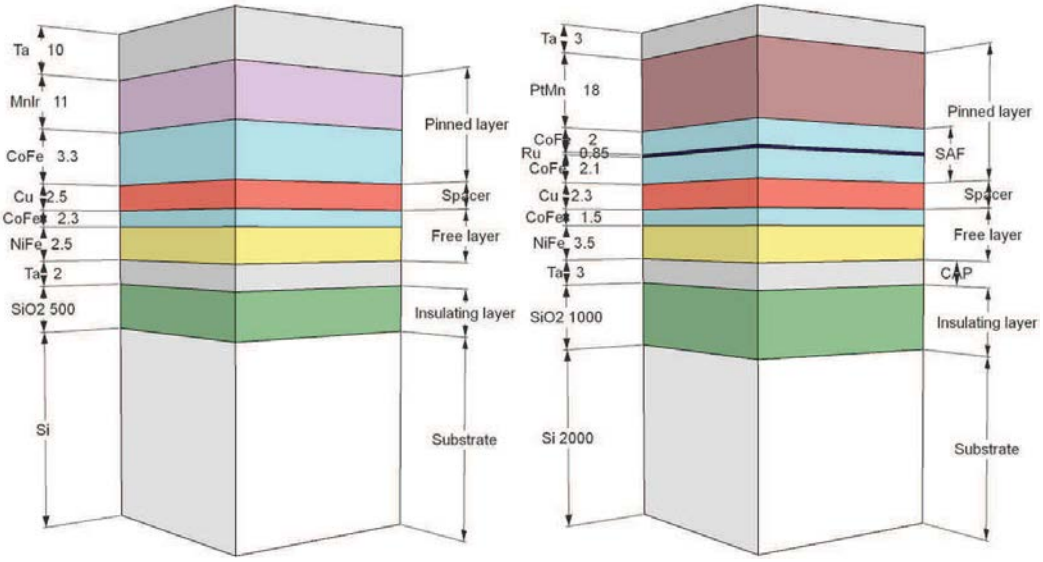

(a) (b)

Figure 3.4: Spin valve stacks used for magnetrode process a) SV stack used for the first set of sharp magnetrode process (from INESC-MN) b) SV stack used for the second and third set of both sharp and planar magnetrode process (from AllegroMicrosystems). Thicknesses are given in nm.

1. Sample preparation: in order to remove any particules contamination and obtain a good resist adhesion as well as an uniform coating, the sample was cleaned in acetone and isopropanol in an ultrasound bath heated at 70°C. Ultrasounds were not used for substrates thinner than 200 µm to avoid breaking it. All samples are then rinsed with deionized water to remove any alcohol traces.

2. Spin coating: after a proper drying, the sample is coated with a positive photoresist chosen according to its thickness properties. The first lithography in sharp probe process is dedicated to reproduce GMR sensor pattern on the thin substrate. Since the total SV stack thickness is lower than 50 nm, we used S1813 photoresist which deposits a thin film of 1.3 µm resist for coating speed of 5000 rpm. The sample is held by vacuum on a spinner chuck and photoresist is deposited on the surface to uniform thickness by spin coating. Both viscosity of the photoresist and spinner rotational speed define the resist thickness by the help of a high speed centrifugal system.

3. Soft baking: Once resist is spin coated, the sample is softly baked at 110° C for 3 minutes on a hot plate to evaporate the coating solvent and densify the resist.

4. Mask alignment: The exposure process is realized on a MJB3 or MJB4 mask aligner that makes physical contact between photomask and sample. Both aligners have a wavelength of 365 nm and 5 mJ/cm^2 and 10 mJ/cm^2 power respectively.

5. Exposure and development: Before contact printing, sample and mask have to be aligned under binocular microscope with the help of alignment landmarks. Alignment is performed with a micromanipulator of three degree of freedom (x,y,θ). Exposure dose depends on lamp power, resist type and thickness, sample surface reflectivity and development conditions. The exposure time is defined according to lithography steps (GMR, contacts, passivation or cutting) (see Table 3.1). The sample is then immersed into a developer (MF319) for 30 to 45 seconds to remove resist from exposed areas and reveal latent pattern. To stop the process the sample is rinsed in deionized water and dried.

6. Hard baking: the sample is shortly annealed on a hot plate at 110° C for hardening of resist.

All these steps will be repeated for the etching, contacts deposition, electrode deposition and passivation layer deposition steps. Figure 3.5 shows a scheme of the GMR lithography steps and Table 3.1 gives the lithography parameters used in the processes.

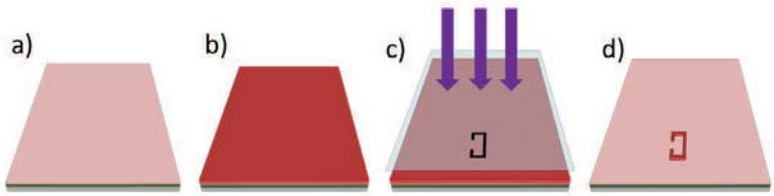

Figure 3.5: Photolithography process of a yoke. a) GMR stack on thin silicon substrate b) Spin coating/photoresist deposition c) Mask alignment and UV exposition (violet arrows) reproducing the pattern (here a yoke) d) GMR pattern after development into MF319.

	GMR	Contacts	Electrode	Passivation	Deep RIE
Photoresist	S1813				AZ4562
Developer	MF319				AZ400K + H_2O (1:4)
Spin coating	5s 500 rpm-60s 5000 rpm				30 s 2000
Exposure	13 s	15 s	10 s	20 s	60 s
Development	45 s				240 s
Baking 1	4 mn 110°C	3 mn 110°C			60 mn 90°C
Baking 2	3 mn 110°C	3 mn 110°C			-

Table 3.1: Photolithography parameters

3.1.1.4 Dry etching

GMR etching Dry etching refers to the removal of material by plasma based process in a vacuum environment. After defining GMR pattern by UV lithography, etching is realized by Ion Beam Etching (IBE) under vacuum environment (10^{-8} mbar) to remove the exposed part of the resist. The sample is set on a ground electrode and an RF field (13.56 MHz) is applied between both electrodes to initiate the plasma. The sample is then exposed to a bombardment of ions generated by the plasma of a neutral gas (Argon in this process). Etching parameters are given in table 3.2.

Power	Beam current	Argon Pressure	Surface	Time
90 W	7 mA	10^{-4} mbar	25 cm^2	20 mn

Table 3.2: IBE etching parameters

Lift-off In order to remove the non-exposed resist of GMR lithography, the etched sample is immersed into acetone to dissolve the resist. This step can take few minutes since GMR patterns are micrometric size. Low ultrasounds can be applied to speed up lift-off process by paying attention to avoid breaking the sample (depends on the substrate thickness (cf 3.1.1.1). When ultrasounds cannot be used, the lift-off may take longer time (up to few hours).

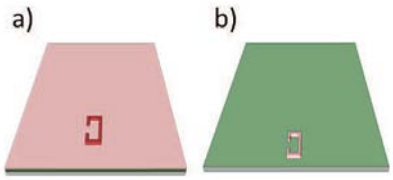

Figure 3.6: Sample after GMR etching and lift-off. a) Sample after photolithography. b) GMR etching has removed the exposed part of the resist and a lift-off step after the etching removes the resist on the pattern. The green color shows the substrate.

3.1.1.5 Deposition techniques

Once the GMR pattern is defined on the sample, contacts and passivation layers are deposited in thin films by two techniques: evaporation and sputtering, both techniques used at SPEC in the Meca 2000 system. Contact, electrode and passivation steps are preceded by a short pre-etching (typically 30 s).

Evaporation

Contacts deposition In the magnetrode process, gold contacts pads are deposited by electron beam evaporation, a thin film deposition technique achieved in vacuum (10^{-8} mbar) to insure the free mean path of particles being without collision. A thin layer of titanium is first deposited to facilitate gold adhesion on the substrate. A crucible, containing the material to evaporate, is heated up by an electron beam emitted by a charged tungsten filament controlled by a high voltage source (9 kV). To insure a good conducting layer with a low resistance contacts, a 200 nm thickness of gold is deposited. Deposition parameters are described in table 3.3; Figure 3.7 shows the contacts deposition steps.

Materials	Pressure	Current	Layer thickness
Titanium (Ti)	10^{-7}mbar	65mA	15nm
Gold (Au)	5.10^{-7}mbar	330mA	150nm
platinum (Pt)	6.510^{-7}mbar	300mA	200nm

Table 3.3: Evaporation parameters for the contacts and the electrode deposition.

Contact deposition is followed by a lift off process to remove the photoresist that was covering the unexposed part of the sample (see figure 3.10).

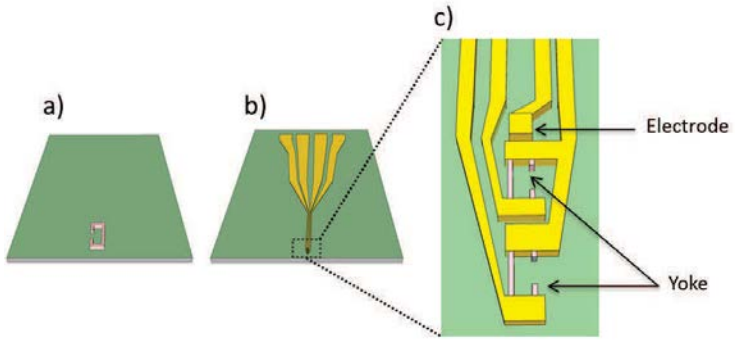

Figure 3.7: Sample after contact deposition. a) sample after GMR etching b) sample after contact deposition, previously lithographied as explained in 3.1.1.3; the resist is spinned and exposed where contact pattern is defined c) a zoom-in of the tip with two yoke sensors and an electrode point contact to measure the electric potential within tissues (in this exemple the electrode is made out of Ti/Au, in the same deposition step as the contacts).

Electrode deposition Once contacts are deposited by evaporation, the sample experiences a third lithographic process to delineate the electrode contact pad. After a pre-etching step the electrode is deposited by evaporation (cf parameters in Table 3.3).

This electrode is meant to record almost at the same location as the GMR sensors the electrical activity of the surroundings neurons (in particular LFPs and potentially spikes of closest neurons). Amplitude and shape of neuronal activity can be analyzed in real-time with only few acquisitions (see Chapter 5). Electrode dimensions and materials have been chosen with respect to ones used for electrophysiology [71, 20, 73]: typically the electrode pad is 20x20 µm and the chosen materials is a bilayer of gold and platinum to insure a good conductivity (Figure 3.8).

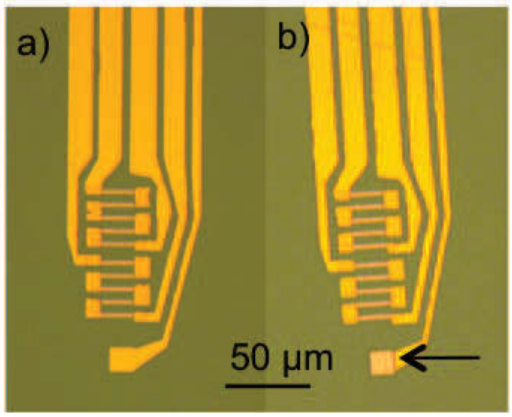

Figure 3.8: Electrode deposition on sharp probe (#M20 Camilo). a) a gold electrode is previously deposited during contacts deposition and then a 200 nm layer of Pt is deposited to insure a better conductivity (b); the black arrow indicates the Pt electrode.

Sputtering The passivation layer is deposited by sputtering, which is a thin film deposition method that uses magnetron sources with high electric and magnetic fields to confine a charged plasma in a vacuum environment (10^{-8} mbar). By applying high voltage to the target, a plasma is created in the chamber, previously filled with an inert gas like Argon.

Both sharp and planar magnetrode are passivated by an insulator bilayer to ensure a proper electrical insulation with the medium. The bilayer is deposited on the whole probe except on contact pad where the sensor is connected by wire bonding. The insulator bilayer is composed by Aluminium oxide (Al_2O_3) and silicon nitride (Si_3N_4). Sputtering parameters are given in Table 3.4. All the probes designs are giving in Annexe 1.

Materials	Pressure	RF Power	Layer thickness
Al_2O_3	5.10^{-3} mbar	200 W	150 nm
Si_3N_4	5.10^{-3} mbar	200 W	150 nm

Table 3.4: Sputtering parameters

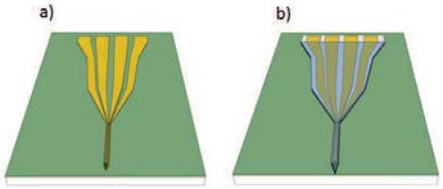

Figure 3.9: Sample after passivation layer deposition. a) sample after contacts deposition b) after insulator bilayers (passivation).

3.1.1.6 Final probe shape

Deep Reactive Etching (DRIE) For planar probe, after passivation deposition, the sample is diced in a square or rectangle shape with a diamond tip scriber along the crystallographic axis of silicon. For sharp probe, as the needle shape does not follow the crystallographic axis, dicing cannot be used and the whole silicon substrate needs to be etched at the outer desired shape.

We used Deep Reactive Ion Etching (DRIE) to define the tip of the probe in a needle-shape by etching silicon substrate. Deep etching uses Bosch process [74], also known as time-multiplexed etching, that alternates repeatedly etching and passivation modes to create deep vertical penetration with a high anisotropic profile as seen in Figure 3.11. Etch mode consists of a plasma that etches the sample from a nearly vertical direction by using a mix of sulfur hexafluoride (SF_6) and oxygen (O_2). Passivation mode is a chemically inert passivation layer deposition (octafluorocyclobutane (C_4F_8). Deep Etching was performed in the MINERVE platform at Institut d'Electronique Fondamentale; the parameters are given in Table 3.5.

Materials to removed	Gaz	Step	cycles
SiO_2	CHF_3	Etching	1
Si	SF_6/C_4F_8	Etching/Passivation	400

Table 3.5: DRIE parameters.

Figure 3.10 shows the final shape probe after DRIE and some Scanning Electron Microscopy (SEM) images are shown in Figure 3.11.

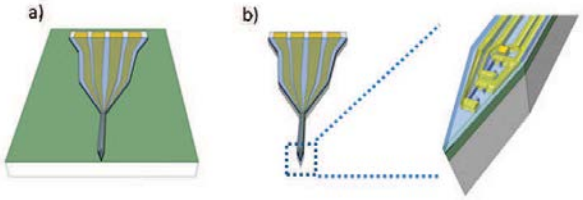

Figure 3.10: DRIE step. a) sample after passivation layer deposition b) DRIE: the silicon substrate is removed to get the final needle shape of the probe.

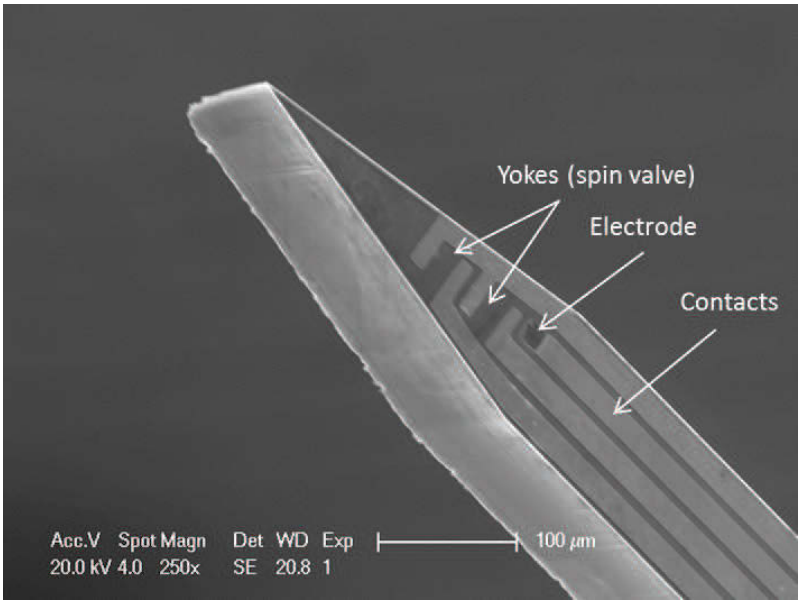

(a) SEM picture of a spin valve deposited on a 150 µm silicon substrate and containing two yokes (30x3 µm) with a gold pad electrode.

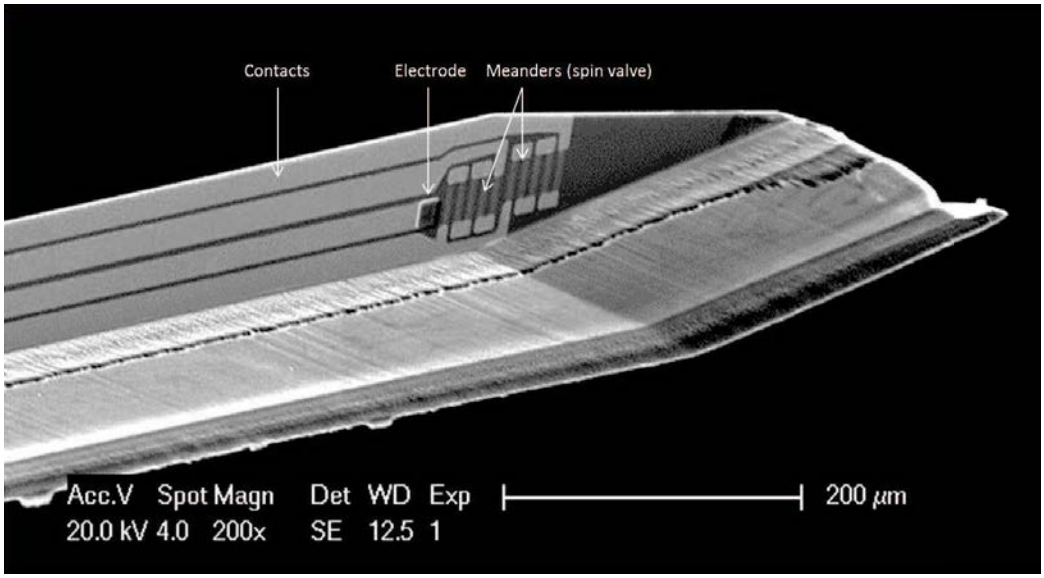

(b) Spin valve deposited on a 200 µm silicon substrate

Figure 3.11: Final shape of sharp magnetrode seen by SEM.

3.1.2 Planar probes

3.1.2.1 Probe design

In parallel to sharp probes, we developed planar magnetrodes to record at the surface of the tissues. We used planar probes for both *in vitro* and *in vivo* experiments with a different design in each case. The required conditions and constraints for planar probes were different from those for sharp probes in terms of size and probe packaging, especially because planar probes are ECoG-like and do not penetrate biological tissues. Planar probes contain a more or less large GMR element deposited on a conventional 700 µm-thick silicon substrate with large contacts area, useful for reducing the contact resistance and decreasing the 1/f noise. Additionally, planar probes require inserting a rather small bias magnet to compensate the coercive field created by the large sensing area (see 3.2).

The fabrication of planar probes is similar to the sharp ones without the final silicon DRIE step. Two planar probes have been developed for *in vitro* and *in vivo* setup as followed :

In vivo Two types of planar *in vivo* probes were fabricated: ones are dedicated to measure either the neuromagnetic field produced by a gyrus (parallel to the surface of the cortex) or the field coming from a sulcus (perpendicular to the surface of the cortex). Both ECoG-like probes have been tested *in vivo (*See Chapter 5).

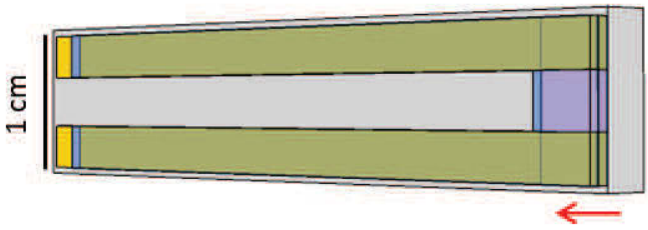

Figure 3.12: Planar or ECoG magnetrode for *in vivo* experiment. The GMR is designed as a rectangular shape with 400x800 µm. The red arrow indicated the field sensitivity axis.

In vitro As described in Chapters 4, we realized two types of *in vitro* experiments. The first type of recordings is performed on the soleus muscle of a mouse to study the magnetic

field created by muscular fibers. The second one is dedicated to measure the neuromagnetic field coming from a hippocampus slice from mouse's brain. Both experiments require two different designs for planar magnetrode that are described below:

Muscle experiment specifications During the experiment, the nerve is hold in a micro-pipette by suction in a conductive liquid (Krebs solution). The main initial idea was to record magnetic fields created both by the nerve and the muscle in order to reconstruct the travelling magnetic action potential in the system. A flat sensor is placed below the muscle, itself attached by insert pins hammered in a silicone gel to hold the muscle.

The first planar probe design was containing two GMR elements, one for each measurement (nerve and muscle). As described in Chapter 4, we focused on muscle response after several ineffective trials. Two types of flat probes dedicated to muscle recordings have been redesigned and fabricated (see Figure 3.13): the first probe is a long rectangular GMR with 4 contacts to record either on the full length of the sensor or on part of it. As the sensor length is 7 mm, it can be located under the muscle, covering the whole length of the muscle.

The second type of probe (right panel on figure 3.13) contains a GMR sensor shaped in meander of 1x1 mm, in an embodiment to measure the muscle with respect to the probe, so measurements at various locations can be performed. Both probes are passivated with a 200-300 nm thick dielectric layer (the same than for sharp probes). The sensor is surrounded in a silicone gel to keep it motionless. The silicone gel is baked at 60-70°C for 8 hours after probe and contact cable insertion.

The full setup scheme, the acquisition setup as well as results will be explained in Chapter 4.

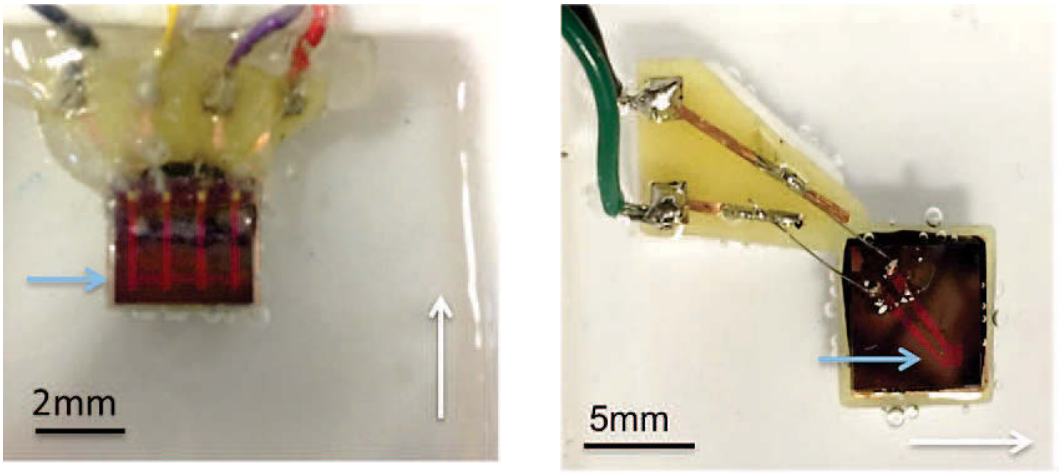

Figure 3.13: Schematic of the flat probes. Left: Rectangular GMR element of 3x1 mm with 4 point contacts. Right: Meander GMR element of 1x1 mm with two contacts. The blue arrow shows the GMR sensor location and the white arrow gives the field direction sensitivity.

Slice setup Planar probes were designed for *in vitro* slice recordings setup (Figure 3.14). In this experiment, we developed very small planar probe designed according to slice's size: GMR size is 400x600 µm (figure 3.14). The slice is deposited on top of the sensor.

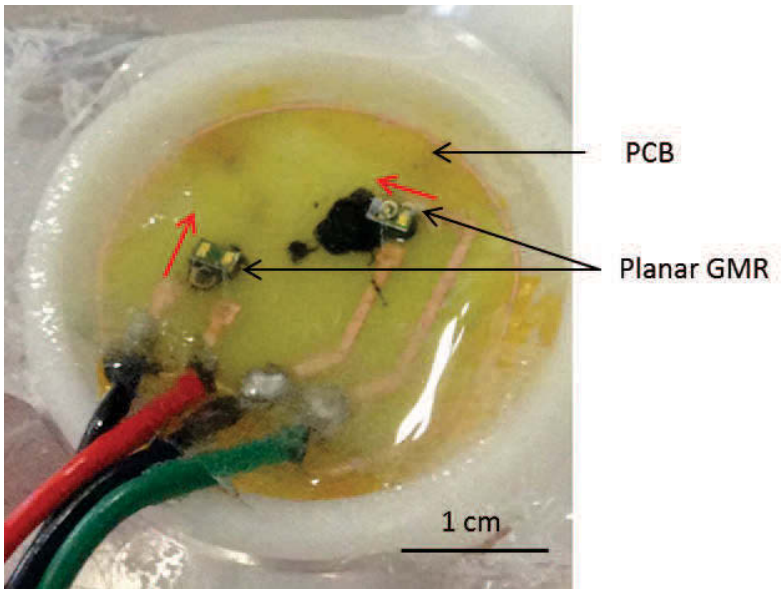

Figure 3.14: Planar magnetrode for slice recordings.

3.1.2.2 Planar probe fabrication

For planar probe, GMR are deposited on 700 µm silicon wafer. After GMR defined pattern (either segment or meander shape) done by photolithography, the sample is etched by IBE (same parameters than in section 3.1.1.4) and then placed in acetone to remove the resist (lift off) leaving the patterned material (picture b) on figure 3.15). To define the contacs pads of the sensor, a photolitography step is realized on the sample and a bilayer of Ti/Au is deposited by evaporation (picture c) on 3.15). Last, the probe is passivated with a bilayer of Aluminium oxide (Al_2O_3) and silicon nitride (Si_3N_4) deposited both by sputtering (3.1.1.5). According to the experiments, the flat probes are cut out either by diamond saw or by laser cutting.

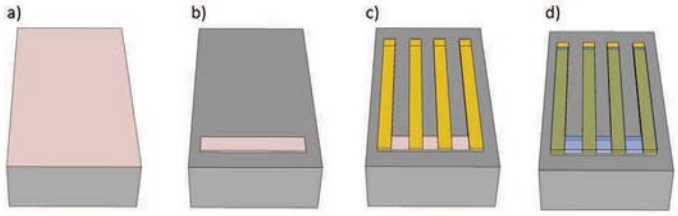

Figure 3.15: Planar probe fabrication. a) GMR SV on silicon substrate (700 µm thick) b) GMR sensor (rectangular) after Ion Beam Etching c) Gold contacts pads layer deposited by evaporation d) Passivation bilayers deposited by sputtering covering GMR sensor and contact area exposed in the conductive solution. Pads contacs at the edge of the probe are uncovered to allow wire bonding.

3.1.3 Probes packaging

3.1.3.1 Connection

Most of the probes (planar and sharp) are contacted by wire bonding on the non-passivated pads contact area to copper lines printed on a Printed Circuit Board (PCB). Wire bonding can be either made with aluminum or gold with 50 µm diameter wires. To reduce the noise contribution, several wires bonding (typically 3 wires) were used on each contact pad. Wire bondings are finally protected by covering the contact pads by a dual component epoxy.

Another contact system has been tried for planar *in vivo* probes which consist in soldering a thin tin-plate copper directly from probe contact pad to the PCB. The weld allows a larger grip contact.

3.1.3.2 Packaging

The sensors are glued with wax on a PCB, previously cut with respect to the sample shape. To insure perfect contacts insulation, two components of expoxy are deposited on wire bonding and on copper paths. Figures 3.16 and 3.17 show both planar and sharp packaged probes for *in vivo* and *in vitro* respectively.

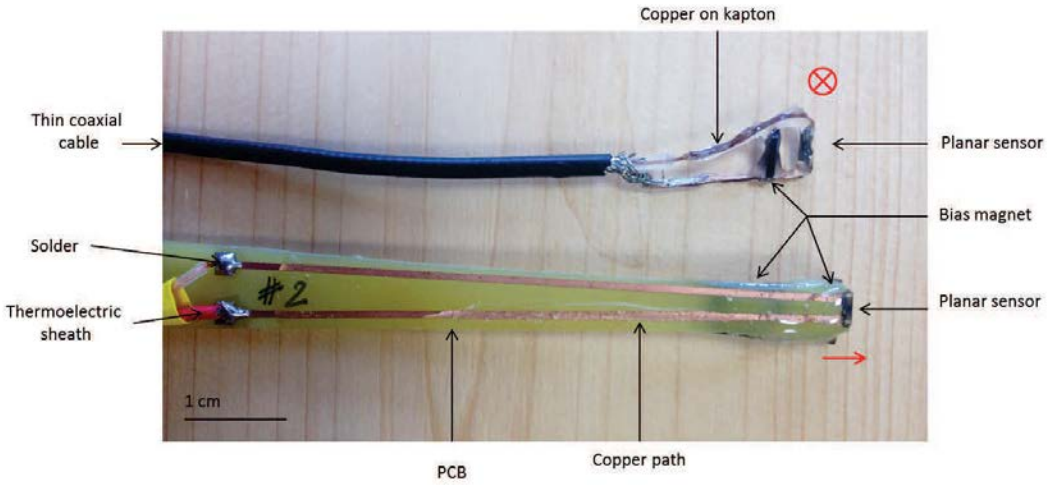

Figure 3.16: Planar probes for *in vivo* recordings. The probe on top contains a planar GMR sensor connected with weld soldering to the copper lines of a flexible kapton and then send to a coaxial cable. On the bottom planar probe, the GMR sensor is glued to a PCB; its contact pads are wire-bonded to the copper lines (protected by an epoxy) and soldered (left handside) to a coaxial cable. Both probes integrated a small permanent magnet meant to linearize the sensor's response around zero field (see 3.2.3.1). The sensitive direction of the sensors is indicated by red cross and red arrow.

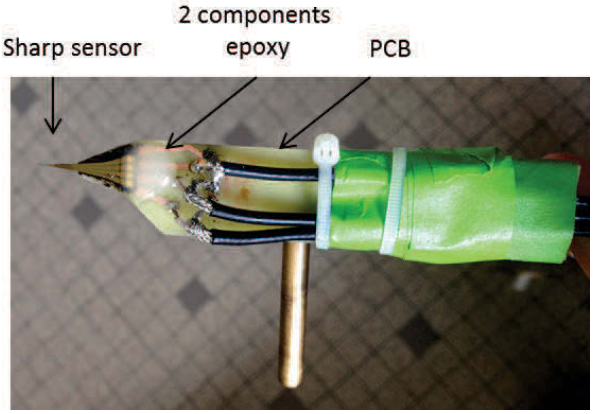

Figure 3.17: Sharp probe for slice recordings. The sensor is fixed on a PCB and the contact pads are wire-bonded and isolated by a 2-components epoxy. The brass rod on the back of the PCB is later fixed to a micromanipulator for precise positioning on the sensor when inserted in the tissues.

3.2 Measurement methods and probe characterization

Neuromagnetic field detection involves very weak signals measurement and localization, thus is it essential to previously characterize the sensors to precisely know their performances. Sensor characterization gives sensor behavior under a known and calibrated magnetic field. To fully characterize the sensor, two types of transport measurements were performed on the sensors; magneto-transport, which gives the sensitivity, the magnetoresistance ratio and the linearity of the sensor, and noise measurements, which lead to the field equivalent noise in the frequency range of interest (here between 1 Hz and few kHz typically). The methods used and the obtained performances on the probes are shown in this part.

Finally, in order to mimick neurons behavior, we developed a phantom which consists of reproducing small neuromagnetic field distribution in a conductive solution close to the one present within biological tissues. Phantom experiments were also performed to test sensors biocompatibility.

3.2.1 Magneto transport characterization methods

3.2.1.1 $R(H)$ transfer curve

The response of unpatterned and processed spin valve sensors is obtained by applying an external magnetic field along the sensing direction, i.e. parallel to the hard layer of the spin

valve (cf Chapter 2); the response is a transfer curve $R(H)$ that gives the resistance variation as function of the applied magnetic field whence instrinsic properties of the sensor can be deduced (MR ratio, sensitivity, linearity). The experimental setup is described below.

Setup Two identical circular Helmholtz coils are powered by a DC current source (Kepco operational Power supply amplifier) to generate uniformly the magnetic field at the center of the coils, where the sensor is located; a commercial current source (Keithley 6221, DC and AC modes) is used for sensor biasing (typically 200 µA to 1mA for the sharp probes and 1-5 mA for the planar probes) and the sensor output voltage is sent to a low noise pre-amplifier SR560 (Stanford Research Systems) with a low-pass filtering (f_c = 30 Hz). The output signal is sent to an acquisition card. The whole experiment (magnetic field scan and data acquisition is driven by a homemade software. The $R(H)$ transfer curve is obtained by swiping the magnetic field typically between -10 mT and 10 mT, i.e. to covers the stack or the sensor response from antiparallel state to parallel state (cf Chapter 2). A schematic of the $R(H)$ setup is shown in Figure 3.18; MR, sensitivity and coercive field can be deduced from this measurement.

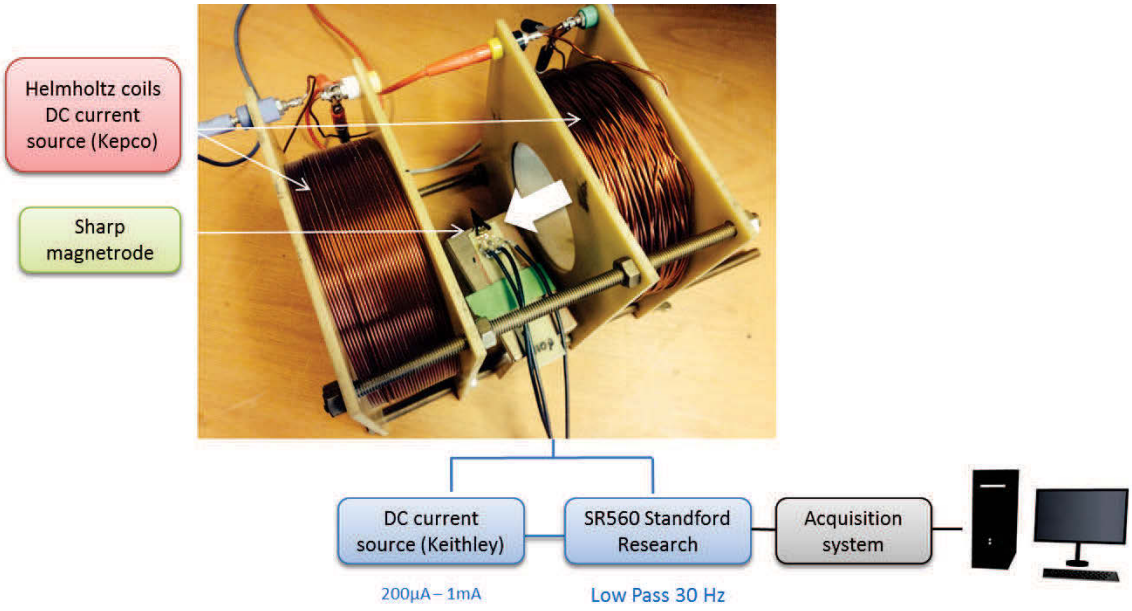

Figure 3.18: Setup for $R(H)$ measurement. A sharp magnetrode is inserted at the center of the Helmholtz coils (red circles). The sensor is powered by a DC current source while the output is low-pass filtered and sent to the acquisition system (laptop screen).

3.2.1.2 Response

In all the experiments, we are measuring very small signals around zero field. Hence, the GMR response is almost linear and can be written as:

$$V_{GMR} = [R_0 + R_1 H]\, I \tag{3.1}$$

where V_{GMR} is the output voltage of the GMR, I the feeding current, H the field of interest and:

$$R_1 = \frac{\Delta R}{\Delta H} \tag{3.2}$$

is the sensitivity of the GMR element (the slope of R(H) curve at H= 0), R_0 is the value at 0 field.

3.2.1.3 Noise

Magnetic sensor performances can be estimated by noise measurement which gives information on the voltage noise level and the corresponding field equivalent noise over a given frequency range. Noise measurements are achieved by applying a calibrated magnetic signal on the sensor while measuring the GMR output through an acquisition chain that will be described below. In the frequency range of interest (below 5-10 kHz), the noise sources present in a GMR sensor are thermal noise, 1/f noise, and Random Telegraphic noise (mostly linked to magnetic noise) (cf Chapter 2).

GMR noise level can be either measured by injecting a DC or an AC bias voltage in the sensor (see 3.2.2). Instead of measuring directly the GMR element output voltage variation, which contains a strong resistance offset component, one records the variation of resistance of the GMR element balanced by an equivalent low noise resistance.

Therefore the amplification scheme can be applied only to the useful content, i.e. the variation around the mean value (see Figure 3.20). This voltage variation is recorded in the time domain and Fourier Transform is applied to obtained the voltage Power Spectrum Density (PSD) over the corresponding frequency range.

A calibrated magnetic field signal, generated by an AC current sent in a coil at a specific frequency (30 Hz), is applied to the sensor which allows extracting the field equivalent noise S_B in $T/\sqrt{Hz}$). The calibration coil used in these measurements generates an rms signal of 850 nT_{rms} (2,42 μT_{pp}) for 1 mA bias current.

Noise measurements done in the laboratory without shielding show a noise intensity of about 10 nT at 1 Hz; this noise level measured through GMR sensors corresponds mostly to the laboratory noise and screens the intrinsic sensor's noise. Therefore noise measurement on the magnetrodes have been all performed in the Magnetically Shielded Room (MSR) of the ultra-low noise building at SPEC in order to get only the intrinsic noise sources from the sensor itself without external noise sources. The MSR (figure 3.19) is a Faraday cage made of alternating sheets of aluminum and mu-metal (NiFe with a high magnetic permeability). Residual magnetic fields are in the order of 0.02 fT at 100 Hz.

All the equipments (pre-amplifier, acquisition system, power supply lines) are placed outside of the shielded room to avoid magnetic external noise coming from power supply line (50 Hz), low consumption lights or 1/f magnetic external noise that could disturb noise measurements and polarize the mu-metal layer. The only magnetic field present is the one created by the test coil which generates a very weak homogeneous field (at maximum of few µT).

Figure 3.19: Magnetically shielded room at SPEC/CEA Saclay.

3.2.2 Measurement methods

Recordings of the output signals of the various sensors developed were achieved through two main modes; DC and AC mode, which are described below.

3.2.2.1 DC measurement

The electronics for the output signal measurement comprises a biasing source (current or voltage), a pre-amplifier stage and a spectrum analyzer (acquisition system and amplification stage). To avoid noise contributions from biasing sources, all the devices (bias sources and pre-amplifier) are supplied with batteries. Each GMR sensor is mounted on a half Wheatstone bridge configuration, with two metal film fixed resistors and a variable resistor to equilibrate the bridge. The 1/f noise of the variable resistor has been measured and it is much lower than the GMR noise.

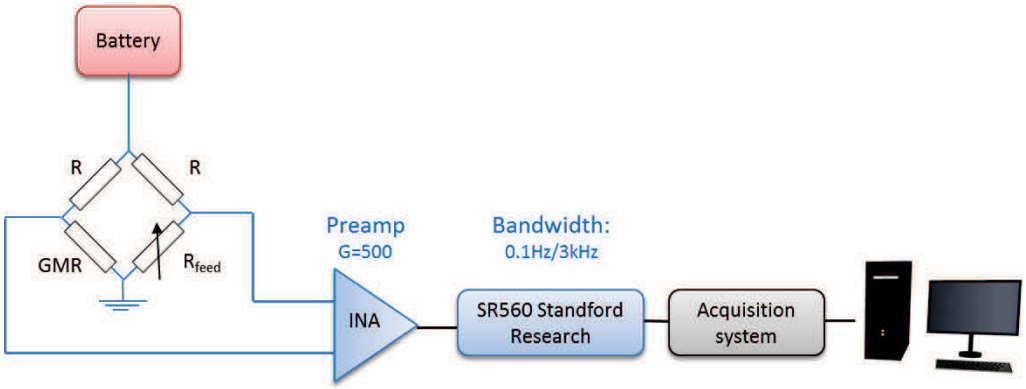

Figure 3.20: Half Wheatstone bridge configuration for a single GMR element measurement. The sensor is fed with a 9 V battery to limit the noise brought by sources powered by the main supply. The sensor is mounted on a half bridge configuration where the equivalent resistance $R_{feed} = R_{GMR}$ to easily balance the bridge output and $R \gg R_{GMR}$.

The output voltage V_{DC} is sent to the very low noise low distortion amplifier (INA103 with voltage noise of 1.2 nV/$\sqrt{Hz}$) and a gain of typically G= 500. The amplified signal is then filtered by a low noise pre-amplifier SR560 (Stanford Research Systems): the filtering stage is fitted according to the desired working bandwidth.

For magnetrode noise measurement we use a low-pass filtering at 3 kHz for avoiding spectral aliasing and a high-pass filtering at 0.1 Hz that suppress DC offset due to static fields. One can notice that the chosen filtering corresponds to the targeted signal duration range typically from 1 ms to hundred of ms (i.e from Local Field Potential to Action Potential) which means a sensor operating from DC to few kHz. The data can be either sent to an oscilloscope or are digitally processed, analyzed and recorded by a homemade acquisition software with a typical sampling frequency of 16384 Hz.

In half bridge configuration, the measured voltage V_{bridge} is simply given by:

$$V_{bridge} = R_1 H I \tag{3.3}$$

where I is given by $V/(R + R_{GMR}) \approx V/R$

3.2.2.2 Capacitive coupling

Previous work on GMR sensors used for magnetophysiology have shown electrical coupling between the living tissues and the magnetoresistive sensors [37]. This is due to the fact that when immersed in the nutrient solution (*in vitro*) or in the cortex (*in vivo*), the magnetic sensors are not perfectly electrically isolated from the surrounding medium, and can be exposed through capacitive coupling to the electric signals that crosses the medium. These signals can be either due to the electrical artefact when electrical stimulation is used *(in vitro* slice and muscle experiments*)* or to the electric physiological signal itself (LFP or AP *in vitro* and *in vivo*).

The output voltage of the sensor is then composed of both the signal of interest and the capacitive coupling (equation 3.5 and Figure 3.21) which may be higher in amplitude than the signal of interest created by ionic currents flowing within living cells. In the frequency range of the physiological signals (dc to few kHz), direct inductive coupling between the local electrode and the magnetrode is neglig

$$V_{bridge} = [R_1 H]\, I + capacitiveterm \tag{3.4}$$

For clarity purpose, we take the example of a signal of interest at the given frequency ω_H and a capacitive term C at the same frequency:

$$V_{bridge} = [R_1 H_0 \cos(\omega_H t)]\, I_0 + C \cos(\omega_H t + \varphi) \tag{3.5}$$

The square root of Power Spectral Density (PSD) associated is shown in Figure 3.21.

One of the main challenge is to separate this coupling from the physiological magnetic signal. For this purpose we used a dedicated frequency modulation/demodulation scheme.

3.2.2.3 AC measurement (frequency demodulation)

In that configuration, we are using also a half bridge configuration and a very low noise pre-amplifier but the biasing of the bridge is AC voltage at a high frequency $\omega_0 \gg \omega_H$. around 30 kHz.

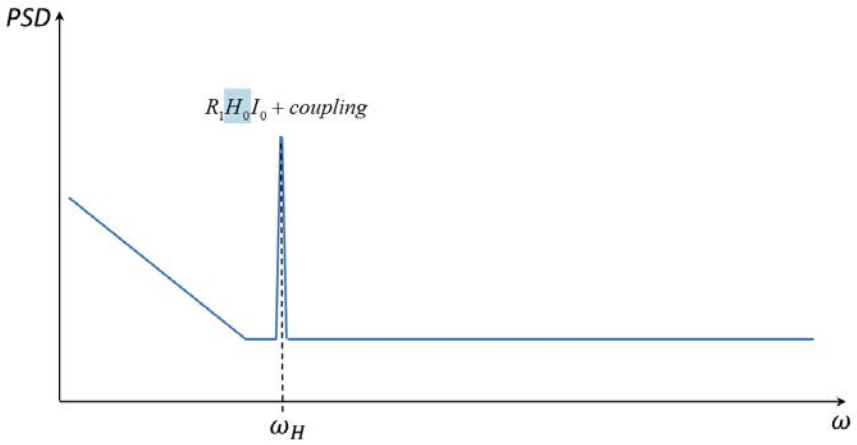

Figure 3.21: Square root of PSD of V_{bridge} with a DC feeding current. The signal of interest, H_0 (highlighted with the green square) is coupled with the capacitive (or inductive) coupling.

An alternative bias current $I = I_0 \cos(\omega_0 t)$ is seen by the GMR (modulation) at high frequency. By injecting I in 3.5 the modulation GMR output signal becomes:

$$V_{bridge} = [R_1 H_0 \cos(\omega_H t)] I_0 \cos(\omega_0 t) + C \cos(\omega_H t + \varphi) \tag{3.6}$$

with $\varphi$the phase difference.

$$V_{bridge} = \frac{R_1 H_0 I_0}{2} \cdot [\cos(\omega_0 - \omega_H) t + \cos(\omega_0 + \omega_H) t] + C \cos(\omega_H t + \varphi) \tag{3.7}$$

The square root of the PSD associated is shown in Figure 3.22

We use a two channel demodulation scheme to recover the information content. It consists on multiplying the modulated signal 3.7 with a cosine signal or a sine signal at the carrier frequency:

$$V_{dem} = V_{bridge} \cdot \cos(\omega_0 t) \tag{3.8}$$

One obtains:

$$V_{dem} = \frac{R_1 H_0 I_0}{2} \cdot [\cos(\omega_0 - \omega_H) t + \cos(\omega_0 + \omega_H) t] \cdot \cos(\omega_0 t) + C \cos(\omega_H t + \varphi) \cdot \cos(\omega_0 t)$$

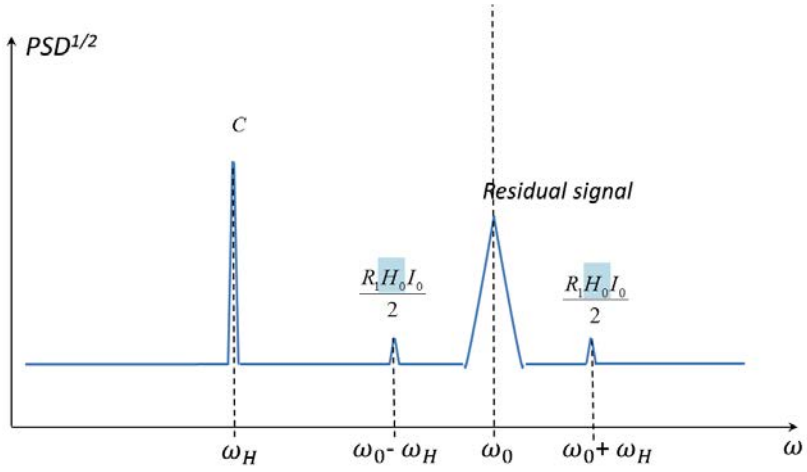

Figure 3.22: Square root of PSD of V_{bridge} with a AC feeding current often a signal at ω_0 is seen due to the non perfect compensation of R_0.

+

$$V_{dem} = \frac{R_1 H_0 I_0}{2} cos(\omega_H t) + \frac{R_1 H_0 I_0}{4} \cos\left(2\omega_0 - \omega_H\right) t + \frac{R_1 H_0 I_0}{4} \cos\left(2\omega_0 + \omega_H\right) t + C \cos\left(\omega_H t + \varphi\right) \cdot \cos\left(\omega_0 t\right)$$

The square root of the PSD associated is shown in Figure 3.23. We can easily see that the capacitive coupling is shifted at the frequency ω_0 and half of the signal is recovered and half of the signal is modulated at $2\omega_0$.

We also demodulate by a sine signal (out of phase, 90°). The expression is then given by

$$V_{demquad} = \frac{R_1 H_0 I_0}{2} \cdot \left[\cos\left(\omega_0 - \omega_H\right) t + \cos\left(\omega_0 + \omega_H\right) t\right] \cdot \sin\left(\omega_0 t\right) + C \cos\left(\omega_H t + \varphi\right) \cdot \sin\left(\omega_0 t\right)$$

+

$$V_{demquad} = \frac{R_1 H_0 I_0}{4} \sin\left(2\omega_0 - \omega_H\right) t + \frac{R_1 H_0 I_0}{4} \sin\left(2\omega_0 + \omega_H\right) t + C \cos\left(\omega_H t + \varphi\right) \cdot \sin\left(\omega_0 t\right)$$

After the demodulation of the signal, a low pass filtering is applied to cut the contamination due to the carrier frequency main signal. The filter is typically of 3 kHz. General schematic of the demodulation module is shown in 3.24.

The output signals are the in phase signal, which relates only to the resistance variations, i.e. to the magnetic signal, and the quadrature signal (out of phase of 90° with respect to the in-phase signal) which should be 0.

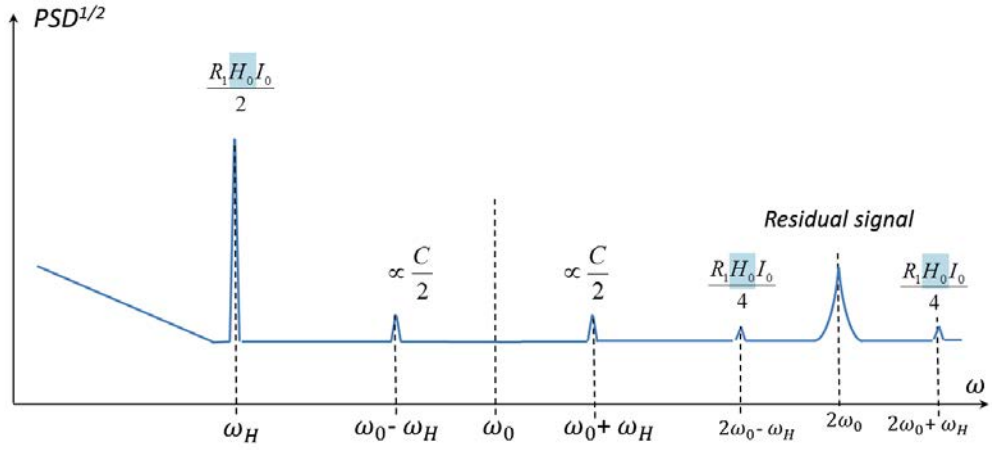

Figure 3.23: PSD after the demodulation step.

In fact, we often observed a non-zero out of phase signal. A first obvious reason is the existence of a capacitance in parallel to the GMR resistance which induces an out of phase and hence a non zero quadrature signal. However this capacitance is measured and typically in the range of 1 nF which induces a small out of phase signal, typically 3-4 % of the in phase signal. However, it should be noted that if there is a small change of capacitance or conductance inside the solution (or the tissues) during the neuronal activity, an out of phase signal may appear.

3.2.2.4 Sensitivity measurements

The sensor sensitivity can be either determined from the R(H) transfer curve, or directly measured on the oscilloscope from the amplified output signal while the magnetic reference signal is applied to the sensor (Figure 3.25).

If V_{OUT} is the output peak-to-peak signal, $V_{outGMR} = \frac{V_{OUT}}{G}$. The corresponds rms signal is then $V_{outGMRrms} = \frac{V_{outGMR}}{2\sqrt{2}}$.

In the example shown in 3.25, with a gain of 500 on the pre-amplifier and 500 on the SR560, $V_{outGMRrms} = \frac{2.7}{2\sqrt{2}\times 500\times 500} = 3.84$ µV.

The reference signal being 850 nT_{rms}, the sensitivity is therefore:

$$Sensitivity = \frac{V_{outGMRrms}}{signal} = \frac{3.84\ \mu V_{rms}}{850\ nT_{rms}} = 4.51\ V/T$$

The GMR resistance measured is R_0= 1 kΩ so the voltage thermal noise corresponding is: $S_{Vnoise}^{1/2} = \sqrt{4 \times 300 \times 1.38 \cdot 10^{-23} \cdot 10^3} = 4.06\ nV_{rms}$ which corresponds to a field equivalent

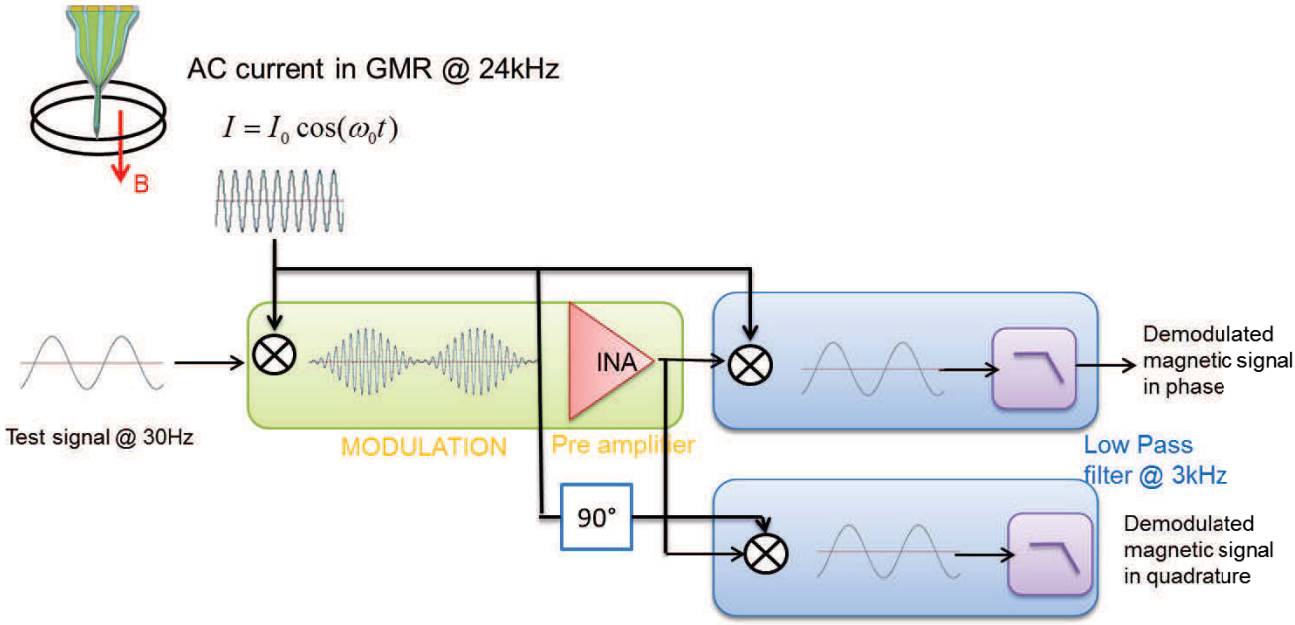

Figure 3.24: Modulation/demodulation frequency principle.

noise of 900 pT_{rms} ($S_{Vnoise}/Sensitivity$) in the thermal noise regime. The given sensitivity in V/T can be compared to the one obtained by the $R(H)$ curve (in figure 3.26) by dividing the sensitivity obtained by noise measurement by the sensor feeding voltage (equation 3.9).

$$\frac{Sensitivity}{V_{inGMR}} = \frac{4.51\ mV/mT}{250\ mV} \cdot 100 = 1.8\ \%/mT \tag{3.9}$$

If we increase the current inside the GMR, the signal increases by the same factor and hence the field equivalent noise becomes better but as the 1/f noise is also increases, the best working position is to increase the current up to a point where the 1/f noise is always larger than the thermal noise.

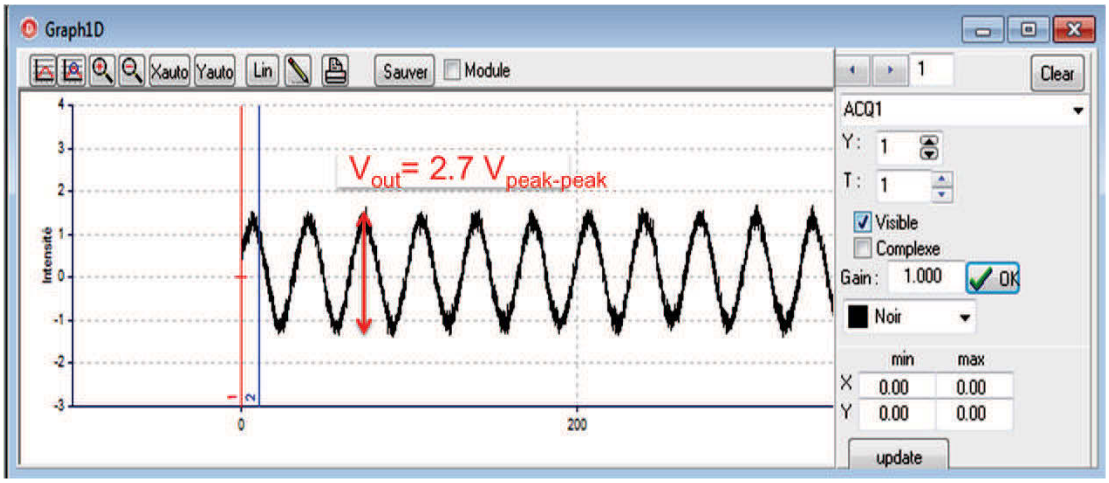

Figure 3.25: Screen shot of acquisition system while applying a test signal of 850 nT_{rms} at 30 Hz on the sensor and measuring V_{GMR} output amplitude as function of time in a DC noise configuration (Probe #Peterson2 *R15*).

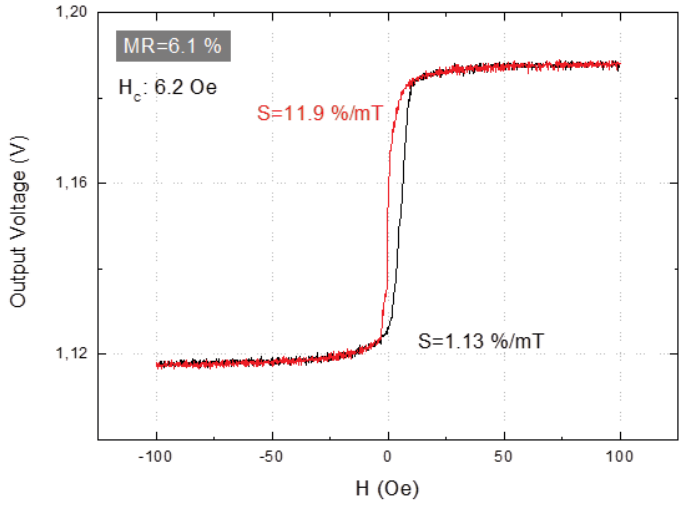

Figure 3.26: $R(H)$ of the sharp probe (#Peterson2 *R15*). The current injected in the GMR is 200 µA with a low-pass at 30 Hz. Note that the sensitivity at zero field is greatly different on the black curve and on the red curve at 0 field, because of the coercive field (6.2 Oe).

The same calculations can be done with AC noise measurement (frequency modulation).

3.2.3 Probes characterization

The magnetrodes are characterized in sensitivity, coercivity, noise (PSD and field-equivalent PSD) from the schemes previously described before being selected and used in the *in vitro* and/or *in vivo* experiments.

Main features of the planar and sharp probes are given below, while detailed characteristics of planar and sharp probes that have been used for the recordings shown in Chapter 4 and Chapter 5 are given in Table 3.9 and in Table 3.10 at the end of this chapter.

3.2.3.1 Planar probes

R(H) Two types of planar probe have been developed for both slices and muscle experiments. Two shapes have been explored: one with a meander shape and the other with a segment shape allowing to measure at various location along a line-shape sensor. Figure 3.27 gives the $R(H)$ response for segment probe (a) and for meander probe (b). Because of the large size (length and width) of the processed planar samples, the rotation of the soft layer is very abrupt and exhibits an hysteresis, which is close to the full stack (unprocessed) behavior, and which is not ideal for sensing purpose. On contrary on small size devices (sharp probes) the shape anisotropy allows having a more linear and hysteresis free behavior.

To add linearity to the response and to reduce the hysteresis in such a way that around zero applied field the sensor sensitivity is maximal, a bias field can be applied to create an anisotropy at 90° of the pinned layer: a small bias magnet can be added with the aim of reducing the hysteretic behavior of the $R(H)$. Bias magnet creates a small magnetic field H_{bias} perpendicularly to the pinned layer (i.e perpendicular to the external field H_{ext}) to align magnetic moments of the soft layer in the direction of H_{bias} while H_{ext} is zero.

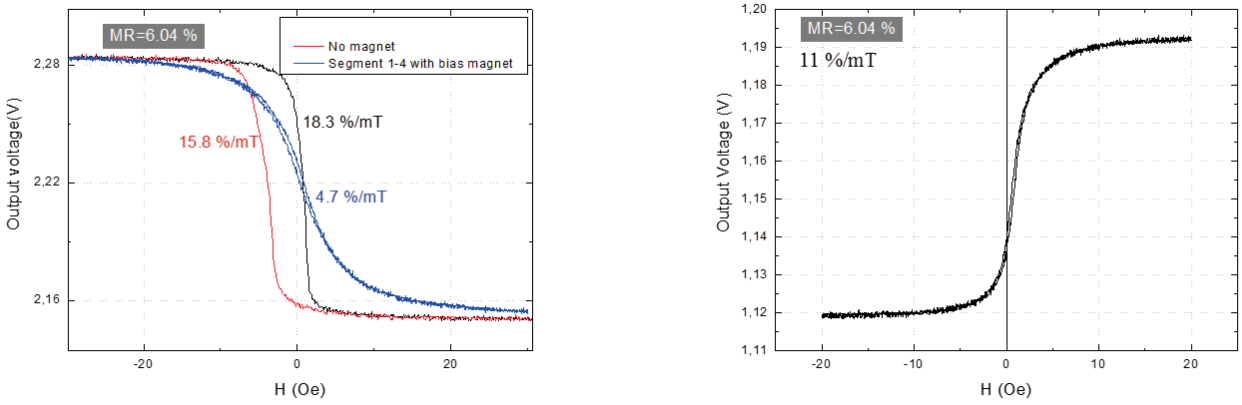

(a) (b)

Figure 3.27: $R(H)$ response of two planar probes. a)$R(H)$ response of a planar rectangular probe (6.5 mm long and 450 µm wide). The initial curve exhibits a coercive field of ∼4 Oe, with low sensitivity at 0 field (1.3 %/mT on red curve). After bias field compensation with the help of a small magnet placed under the sensor PCB holder, the coercive field tends to be closed to zero (blue curve). The corresponding sensitivity is 4.7 %/mT. b) $R(H)$ for a meander shape planar probe (1 mm long and 580 µm wide) and integrates a magnet on the back side of the sample holder to linearize the response and reduce the coercivitiy. The sensor exhibits a sensitivity of 11 %/mT with a coercive field $>$ 0.5 Oe and well centered. The MR ratio is 6.04 % for both probes.

Planar probes are characterized in $R(H)$ after processing and after positioning the bias magnet (usually on the back side of the substrate or on the sensor holder).

Noise Noise measurements of planar probes have been realized in the shielded room, both with DC source and AC source. Figure 3.28 shows PSD of the noise (voltage and field) for meander planar probe. The resistance of the sensor is 250 Ω, leading to a thermal noise of 2 nV/$\sqrt{Hz}$; the measured thermal noise from the voltage PSD is 3.2 nV/$\sqrt{Hz}$ which takes into account the noise coming from the pre-amplifier. The feeding current varies from 0 to 20 mA (5 V) to observe the GMR behavior, especially at high voltage where the 1/f begins to appear; it can be deduced the best operating voltage/current which combines large feeding current, which increases the output signal, and low 1/f noise depending on both the working bandwidth and the targeted frequency signal (either fast event as AP or low event such

LFPs). The main parameter is here to operate in the voltage/current conditions which lead to the higher SNR in the frequency range of interest.

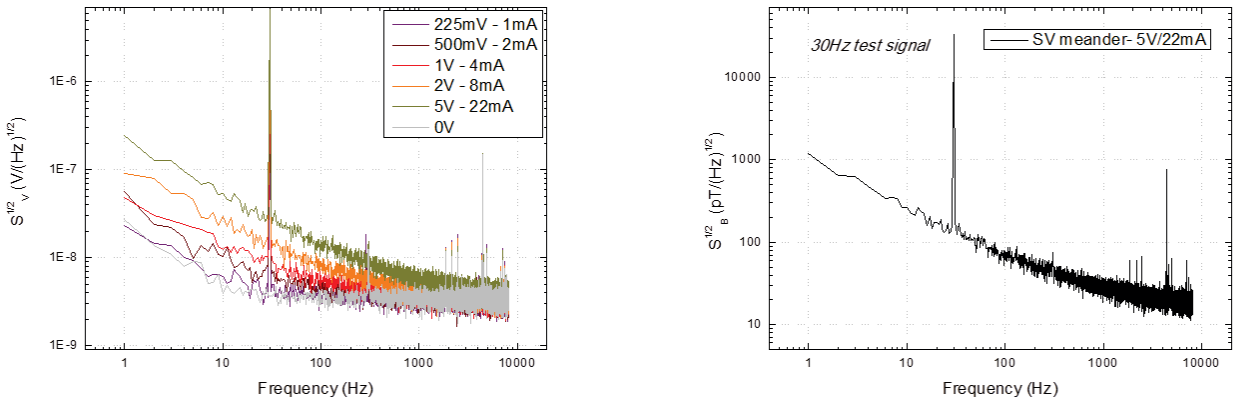

(a) (b)

Figure 3.28: Noise measurements on meander planar probe with DC setup. A test signal of 850 nT_{RMS} at 30 Hz is sent to calibrate the sensor. a) S_V corresponds to the PSD of the voltage noise as a function of frequency for various bias voltages. b) Corresponding field equivalent noise S_T expressed in $pT/\sqrt{Hz}$ as a function of frequency.

3.2.3.2 Sharp probes

R(H) Compared to planar probes, sharp probes exhibit a lower sensitivity since their contact resistance is higher, because of the smaller allowable size on the overall surface. The GMR sensor being also of much smaller size, the volume is reduced and the probes are subjected to a higher 1/f noise. The resistances being in the range of few 100 Ohms to few kOhms, the thermal noise is between 2 to 4 times larger. On the other end, these sharp probes are meant to be closer to the signal source and can experience higher magnetic signals.

The first set of sharp magnetrodes fabricated contained two yokes (3x30 μm) either sensitive to the direction along the length or perpendicular to the length of the probe. A typical $R(H)$ from a sharp probe processed is shown in Figure 3.29 with a MR ratio of 5 % and a sensitivity of 0.6 %/mT. Because of the shape anisotropy given by the dimensions of the

sensor, one can note that the $R(H)$ response shows a linear, centered, free of hysteretic behavior and of jumps, which is suitable for our applications (cf Chapter 2). Nevertheless, the sensitivity of this set of probes was too low for very weak magnetic field detection. Sharp probe with yoke parallel to the length has the same sensitivity range (around 1 %/mT). Some of them occasionally present jumps in the $R(H)$ response (figure 3.29) or are not well centered (around zero) which can be an issue because the signals of interest have a very low amplitude (pT to nT range).

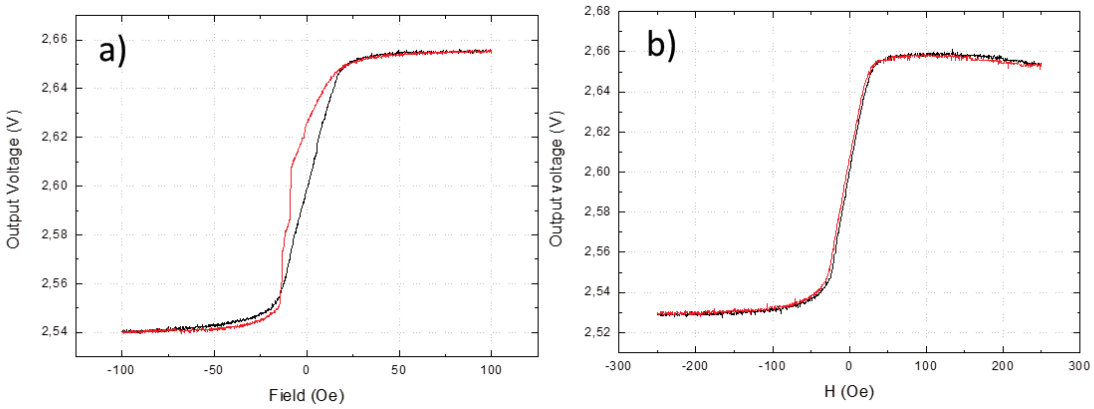

Figure 3.29: a)$R(H)$ response of a yoke with 200 µA feeding current, presenting some jumps due to magnetic domain switching. b) $R(H)$ response of a yoke for a 200 µA feeding current and with a low-pass at 30 Hz.

The second and third sets of sharp magnetrodes have been improved in terms of sensitivity and noise reduction, mostly thanks to the use of a slightly different spin valve stack (SAF stack) and a higher GMR volume . New designs have been drawn with both meander and yoke with a larger width (4 µm instead of 3 µm). The $R(H)$ response for two 4 µm meanders is shown in Figure 3.30. The sharp probe shows a sensitivity of 3 %/mT and a MR ratio of 6 % which is five times better than the first probe set. The field response exhibits a linear and centered curve.

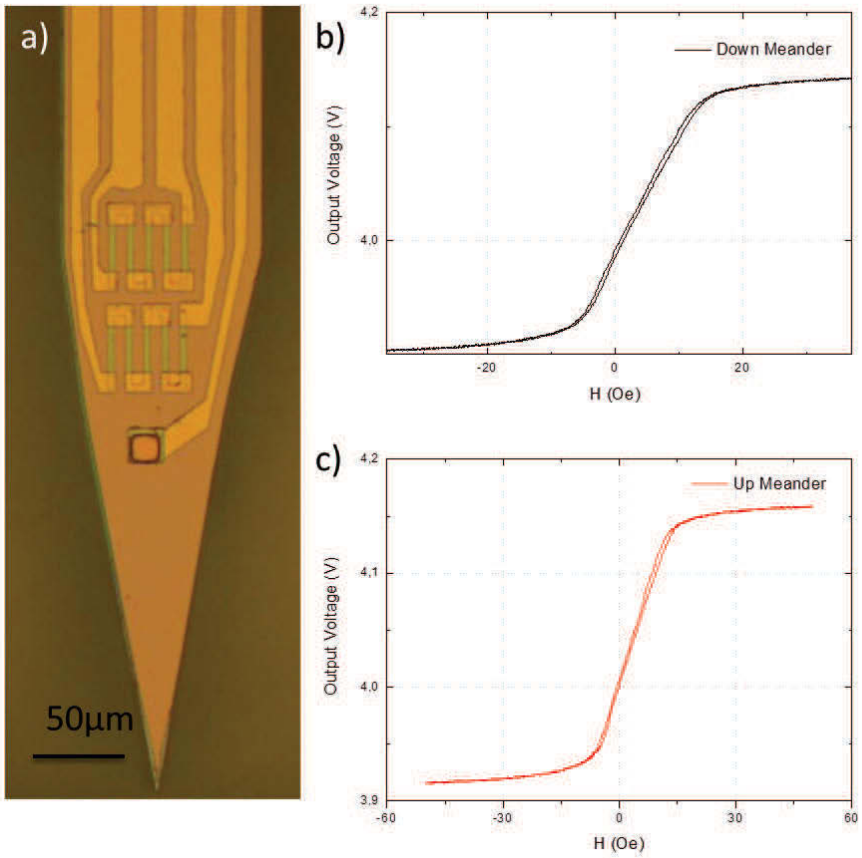

Figure 3.30: Sharp probe (#M24 Meldhau) a) Fully processed probe. b) and c) $R(H)$ of both meanders. The sensitivity of the lower meander is 2.9 %/mT and 2.7 %/mT the upper meander. The MR ratio is 6.1 % and 5.9 % respectively.

Noise The main limitation in sharp magnetrodes is coming from the 1/f noise, which limits the SNR and though the field detection at low frequencies. Therefore, efforts have been done to reduce this component, mostly by increasing the size of the sensor. Figure 3.31 shows the voltage PSD for one of the first sharp probe that contains two yokes with 3 µm width and 30 µm long, the resistance of the yoke being 440 Ω. The 1/f noise is largely dominant below 1 kHz, even for small feeding current. On such a device, the field equivalent noise at 10 Hz and 0.5 mA is of the order of 800 nT/$\sqrt{Hz}$, and of 7 nT/$\sqrt{Hz}$ at 1 kHz.

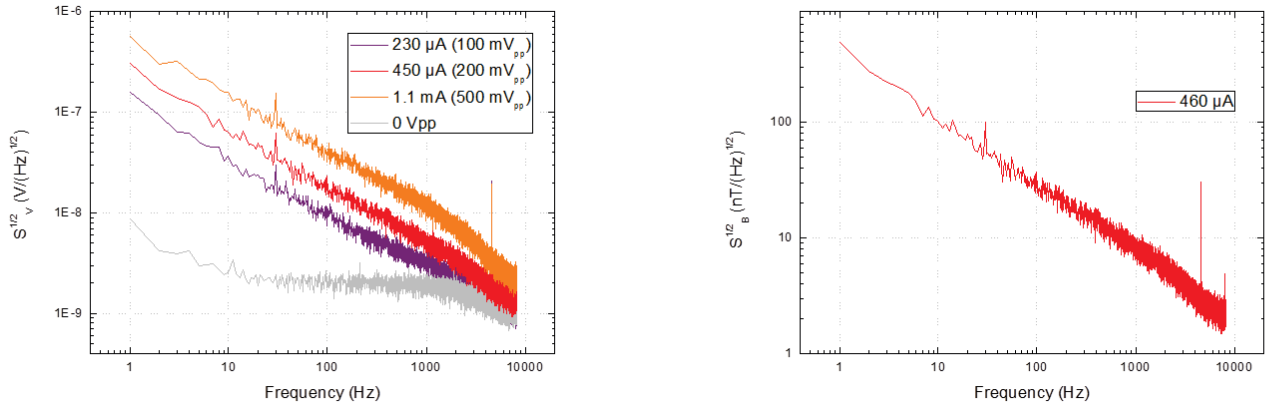

(a) (b)

Figure 3.31: DC noise measurements of the sharp magnetrode #M8a (30x3 µm yoke- 440 Ω) with DC noise measurement. The frequency bandwidth is 0.3 - 3 k Hz. An AC signal test at 30 Hz produced a magnetic field of 100 nT_{rms} that is measured by the sensor (seen in the PSD). Noise measurements were achieved in the shielded room. a) PSD of the voltage noise for several bias currents. b) Field equivalent noise (detectivity).

Additionally some probes display a strong magnetic noise as can be seen in figure 3.32: a reference magnetic signal at 30 Hz is applied on the GMR to get the voltage noise response (red line); in order to evaluate the magnetic noise component, the sensor is switched to its saturated state by adding a bias magnet; the output GMR response is shown in green, displaying a less noisy response that reveals magnetic instabilities and therefore magnetic noise in the sensor. One can note that the reference signal is not detected by the GMR when on its saturated state. Table 3.6 gives the noise level for each case at different frequencies.

	1 Hz	30 Hz	1 kHz
S_V (nV/$\sqrt{Hz}$) without bias field	388	72	10
S_V (nV/$\sqrt{Hz}$) with bias field	300	30	5

Table 3.6: Voltage noise level with and without bias field.

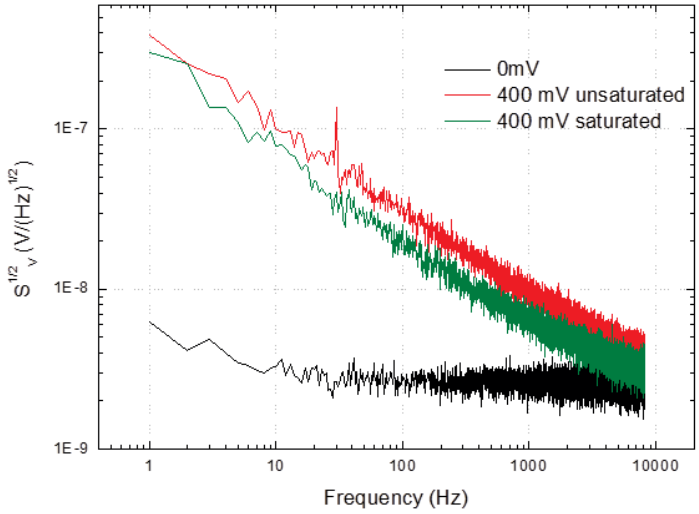

Figure 3.32: S_V as function of frequency for a 3 μm width yoke with R = 250. The bias voltage (DC measurement) is 400 mV (1.6 mA) and a magnetic signal of 1 μT at 30 Hz is applied on the sensor to get the sensor output under a weak magnetic field. Black curve is the spectrum without GMR feeding current (V= 0 V). The red curve corresponds to the PSD of the output GMR with a 400 mV bias voltage. The green curve is obtained by attaching a small bias magnet under the sensor in order to saturate the GMR to see whether magnetic noise appears (especially at low frequencies); the sensor is thus in the saturation regime and no signal (30 Hz) is detected. (#M4b)

Sharp probes model comparison The first set of sharp magnetrodes were containing two yoke (3x30 μm) either sensitive to the direction along the length or perpendicular to the length of the probe. Typical MR ratio was 5 % and a sensitivity between 0.5 - 2 %/mT. The R(H) responses were linear, centered, without jumps neither hysteretic behavior which is suitable for our applications. Nevertheless, the sensitivity of this set of probes was too low for very weak magnetic field detection. The following sets of probes have an improved detectivity of one order of magnitude as shown in Figure 3.33. These sets have been used for *in vivo* experiments.

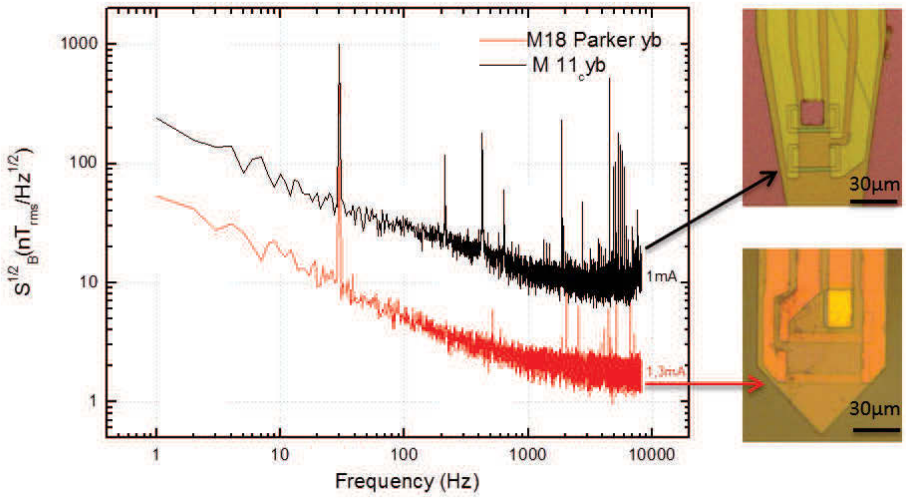

Figure 3.33: S_B as function of frequency for sharp model 1 (#M11) with 2 yokes (3x30 µm) and sharp model 4 (#M18Parker) with 2 larger yokes (4x40 µm).

3.3 Phantom

Mimicing the behavior of a neuron to test the probes concept before experimenting on real biological tissues is a preliminary experiment useful to test the magnetrode in a biological-like environment (especially the passivation stability under a nutritive solution).

To do so, a phantom has been realized with a thin wire copper dropped into a conductive solution (Artificial Cerebro Spinal Fluid - ACSF). The sensor is positioned with micromanipulators close enough to estimate the magnetic signature of the wire. The phantom was also used for testing the electronics readout scheme that have been developed in conditions close to those of the tissues, and to evaluate the stability of the probe response in a ionic and aggressive liquid. A simple wire in a conductive solution was the first phantom developed to test the electronics setup as well as the stability of the probe.

3.3.1 Setup

A small AC current is sent through a thin wire dropped into an ACSF generating a small electromagnetic field (EM) comparable in amplitude to those emitted by neurons.

The ACSF has the following composition:

KCl	NaCl	NaHCO3	NaH2PO4
2.24 g/l	73.36 g/l	21.84 g/l	1.72 g/l

Table 3.7: ACSF composition

The solution is diluted in deionized water at 1/50 to reach a conductivity of 4 mS/cm (250 Ω) which is close to the brain conductivity [75].

A sharp magnetrode is placed close to the wire to detect the EM field. The wire diameter is 50 μm, 5 times larger than the typical axon diameter of a pyramidal neuron and the AC current was calculated to produce a magnetic field in the range of hundreds of pT to few nT at several frequencies (cf Table 3.8). The EM field is measured by the sharp magnetrode at several locations giving rise to the produced magnetic field map shown in 3.3.2. The setup is composed by a small piece of printed circuit board fixed into a plastic box where the thin wire is dropped into the conductive solution. The current is sent through the wire by a current source (Keithley) at different frequencies. A scheme of the setup is described in figure 3.34

$$\nabla \wedge \overrightarrow{B} = \mu_0 \overrightarrow{J} \tag{3.10}$$

where B is the magnetic field produced by a current density J and μ_0 is the vacuum permeability ($\mu_0 = 4\pi \cdot 10^{-7}$ A^{-2}.m.kg.s^{-2} or H/m). The integral form of equation 3.10 is given by:

$$\oint \overrightarrow{B} \cdot \overrightarrow{dl} = \mu_0 \cdot I \tag{3.11}$$

Once can deduce the Biot and Savart law applied on a wire:

$$B = \frac{\mu_0 I}{2\pi r} \tag{3.12}$$

The injected current I was 100 mA at 30 Hz and the distance r was varying between 1 mm $\leq$ r $\leq$ 1 cm.

For a r = 1 mm distant from the wire, the magnetic field B produced is then:

$$B = \frac{4\pi \cdot 10^{-7} \cdot 100 \cdot 10^{-3}}{2\pi \cdot 10^{-3}} = 20\ \mu T \tag{3.13}$$

I (A)	B (T) at 1mm	Frequency (Hz)
200 µA	40 nT	30 Hz
100 mA	20 µT	30 Hz

Table 3.8: Parameters used in the wire in the phantom.

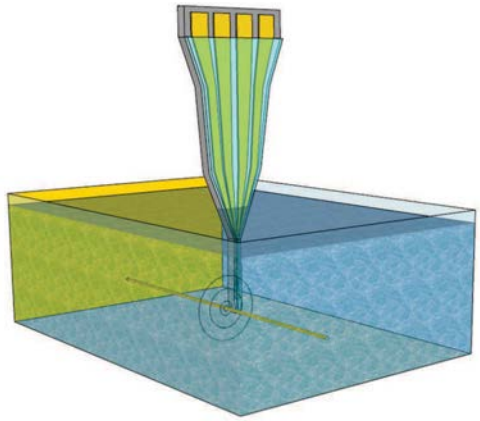

Figure 3.34: Phantom wire setup. A sharp magnetrode is inserted in a box filled with a conductive solution (ACSF). A signal at 30 Hz is sent into a thin wire and produce a small magnetic field detected by the probe.

3.3.2 Results

The measurements have been realized in a non-shielding environment and with both DC and AC measurement methods. The testing probe was a sharp processed magnetrode from the first set of magnetrode. The first important result is that the probe does not degrade over time in the liquid when submitted to a feeding current. This stability demonstrates that the passivation layer is enough to prevent corrosion from the liquid to the sensor. This is absolutely necessary in order to perform long time recordings that will be later on performed in vitro and in vivo. This setup allowed us also to test the AC modulation scheme and evaluate the good separation between direct inductive/capacitive coupling and magnetic signal.

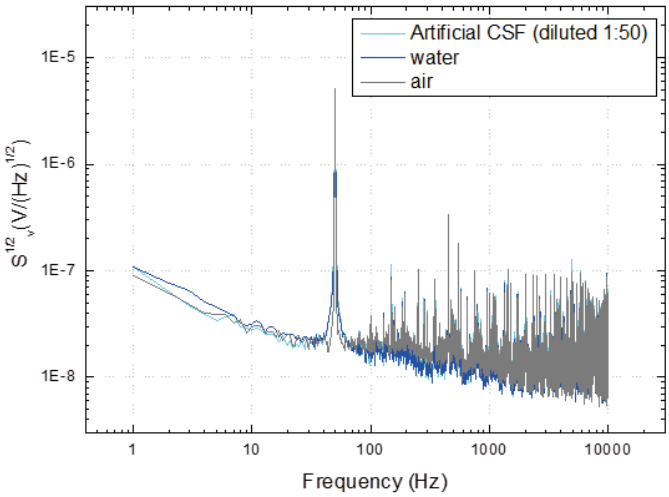

Figure 3.35: PSD of sharp magnetrode (#M4a-yb) with DC measurement in a wire phantom setup within different mediums. Note that the noise level is comparable according to the medium (air, water or ACSF) which is a signature of a well-insulated probe.

3.4 Conclusions

Two types of magnetrodes have been realized, according to processes that have developed and adapted to the specifications of the probes. Specific electronics scheme have been built to measure the probe responses, either in DC feeding mode or in AC modulation mode. All the fabricated probes have been characterized through magneto-transport, noise measurements and have been calibrated in terms in field-level response for a frequency range (DC -3 kHz) corresponding to the frequency where biological signals are expected. Additionally, some of the probes have been tested in a conductive liquid medium mimicking the tissues ionic composition, and have been shown to be stable in time.

Experiment	Slice	Cortex		
Probe	#M11G	#M19Evans	#M24Monk	#M19Camilo
Shape	yoke	single meander (5 segments)		2 meanders
Sensitivity direction	Along the tip	Perpendicular to the tip		Along the tip
Size	3x24 µm	4x30 µm	5x30 µm	2x 4x30 µm
Sensing area	72 μm^2	600 μm^2	750 μm^2	2x 600 μm^2
GMR stack	SV (INESC)	SV (Allegro)		
Substrate thickness	150 µm	200 µm		
Electrode	no	yes		yes
Resistance (Ω)	240	820	440	830
Sensitivity	1.2 %/mT	1.98 %/mT	5 %/mT	Mh 2.4 %/mT Mb 2.1 %/mT
MR	4.48 %	6 %	6 %	Mh 6 % Mb 5.8 %
Coercive field (H_c)	0 Oe		Mh 2.63 Oe Mb 0.76 Oe	Mb 3.6 Oe
R(H)	Centered, linear	Centered, jumps near saturation regime		
Bias voltage	500 mV	500 mV	1V	500 mV
S_B @ 10Hz	20 nT/$\sqrt{Hz}$	7 nT/$\sqrt{Hz}$	9 nT/$\sqrt{Hz}$	4 nT/$\sqrt{Hz}$
30Hz	11 nT/$\sqrt{Hz}$	4 nT/$\sqrt{Hz}$	6 nT/$\sqrt{Hz}$	2.5 nT/$\sqrt{Hz}$
1kHz	2 nT/$\sqrt{Hz}$	800 pT/$\sqrt{Hz}$	1 nT/$\sqrt{Hz}$	520 pT/$\sqrt{Hz}$
10kHz (thermal noise)	990 pT/$\sqrt{Hz}$	300 pT/$\sqrt{Hz}$	500 pT/$\sqrt{Hz}$	150 pT/$\sqrt{Hz}$

Table 3.9: Sharp probes characteristics

Experiment	Slice	Muscle					ECoG	
Probe	Slice	S1	S2	S3	M1	M2	1	2
Shape	Rectangle	Segment			Meander		Segment	
Size	200 x 400 µm	500x1800 µm			4 x (200 x 1000) µm		400 x 800 µm	
Sensing area (mm^2)	0,08	2,7			0,2		0,32	
Resistance (Ω)	30	172	172	105	225	28	28	28
Sensitivity (%/mT)	9.5	10.6	13	8	11	9.5	7.3	13
MR (%)	6	6	6	6	6	6	6.6	6.6
Bias voltage	-	300 mV	340 mV	340 mV	500 mV	330 mV	1 V	1 V
S_B @ 10 Hz ($/\sqrt{Hz}$)	-	800 pT	1.9 nT	1.3 nT	9 nT	660 pT	450 pT	1 nT
S_B @ 30 Hz ($/\sqrt{Hz}$)	-	640 pT	1.4 nT	1.3 nT	6.9 nT	350 pT	375 pT	850 pT
S_B @ 1 kHz ($/\sqrt{Hz}$)	-	600 pT	950 pT	820 pT	1.6 nT	154 pT	68 pT	109 pT

Table 3.10: Planar probes characteristics.

Chapter 4

In vitro recordings

All the recordings presented in this chapter have been realized at UNIC-CNRS with Gilles Ouanounou (muscle experiments), Apostolis Mikroulis (slice experiments) and Thierry Bal. Modeling have been performed by Francesca Barbieri and Gilles Ouanounou.

Animal care followed the European Union regulations (O.J. of E.C. L358/1 18 December 1986).

4.1 Muscle experiment

4.1.1 Context and Objectives

4.1.1.1 Nerve-muscle junction physiology

The neuro-muscular system is the junction between a motor neuron and a skeletal muscle; it is a well-studied and understood system for synaptic transmission mostly thanks to the basic features of chemical synaptic transmission, which involves a relatively simple mechanism: in contrast to central nerve cells which have convergent connections, muscle cells are mono-innervated with a single excitatory synapse (Figure 4.1). The nerve contains a hundred of axons and is connected to the muscle fibers by synapses that release neurotransmitters acetylcholine (ACh) to open voltage-gated Na^+, K^+, Mg^{2+} and Ca^{2+} channels located at the post-synaptic cell (i.e the muscle fibers). Contrary to cardiac and smooth muscles, skeletal muscle can be movement-controlled by nervous stimulation to trigger Action Potentials (APs), eliciting a post-synaptic potential at the level of the nerve muscle synapse that conducts to the propagation of an AP along the muscle followed by a contraction [3].

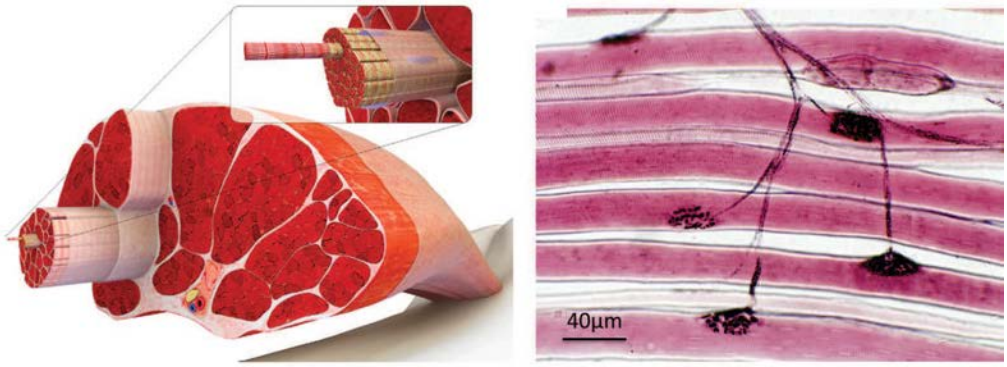

Figure 4.1: The neuro-muscular junction from a soleus mouse muscle. Left: the skeletal muscle is connected to the tendons by its extremities. The muscle is made of bundles of muscle fibers which are parallely arranged. Each fiber is surrounded by the sarcolemma which is the cell membrane. Right: microscope picture of a neuromuscular junction. The black dots are the synpapses at the nerve terminal which are connected to muscle fibers (pink lines). Adapted from [76]

4.1.1.2 Magnetic response modeling

Muscle and nerve share with neurons the ability to trigger synchronous APs and in both systems the internal gradients provide the force generating axial currents flowing along the intracellular space.

A single stimulation on the nerve which reaches the threshold induces a synchronous AP in all the muscular fibers. The muscular AP arises at the center and propagates towards the ends of the muscle. The openings on the Na^+ channels at the junction leads to an increase of the potential at $t = 0$ from its resting value (-90 mV) to the inversion potential (around +20 mV, which corresponds roughly to the contribution of the sodium conductance and to the leakage conductance). This potential decreases along the fiber length because of the membrane leakage through the potassium channels to reach the resting potential over a certain distance as represented in Figure 4.2. This non-isopotentiality in space leads to the immediate appearance of an axial current, which is directly the difference in potential multiplied by the intracellular conductance.

The muscle axial currents are supposed to be larger than the ones flowing into dendrites and axons because muscle fibers have larger diameter (30-40 µm compared to 2 µm for the nerve or for a neuron [3]), thus it should provide rather large Magnetic Field (MF). In addition, the neuro-muscular junction is a relatively simple model for experimentation, muscle cells being large enough to accommodate micro-electrodes needed for electrical recordings.

At $t = t_1$, other sodium channels are opened at a small distance from the center, on each side of the muscle, and the AP moves in space towards the end. At $t = t_2$, the AP is for instance at the middle distance between the center and the ends of the fiber. If one considers the potential distribution, it is at maximum at the location where the sodium channels open at t_2, it decreases according to a certain slope on the front part (towards the end) because of leakage, and it also decreases along a smoother slope on the back part, in direction of the central initiating point, due to the repolarization process. At $t = t_3$, the AP has traveled all the way to the end of the fiber.

Electrophysiological recordings in the extracellular medium give information on the variation of the external potentials, due to the transmembrane flux. Intracellular recordings leads to the measurement in time at a specific location of the AP, but none of these techniques or any other electrophysiological or optical tools allows the recordings of the axial currents.

Magnetic recordings are giving access to this value, since the axial currents associated to the intracellular potential changes during the AP propagation have a magnetic signature.

The expected shape of the magnetic AP has a bipolar shape as shown in Figure 4.2 taking into account the direction and value of the axial currents.

One can note that obtained magnetic signals depend on the size and of location of the magnetic probe. The signal is averaged over the probe length and the timing of the signal depends on the distance between the probe and the center of the muscle, where the signal is initiated. For example if the probe is positioned at the center of the structure, the signal propagating to one end will be exactly canceled by the signal traveling to the other end.

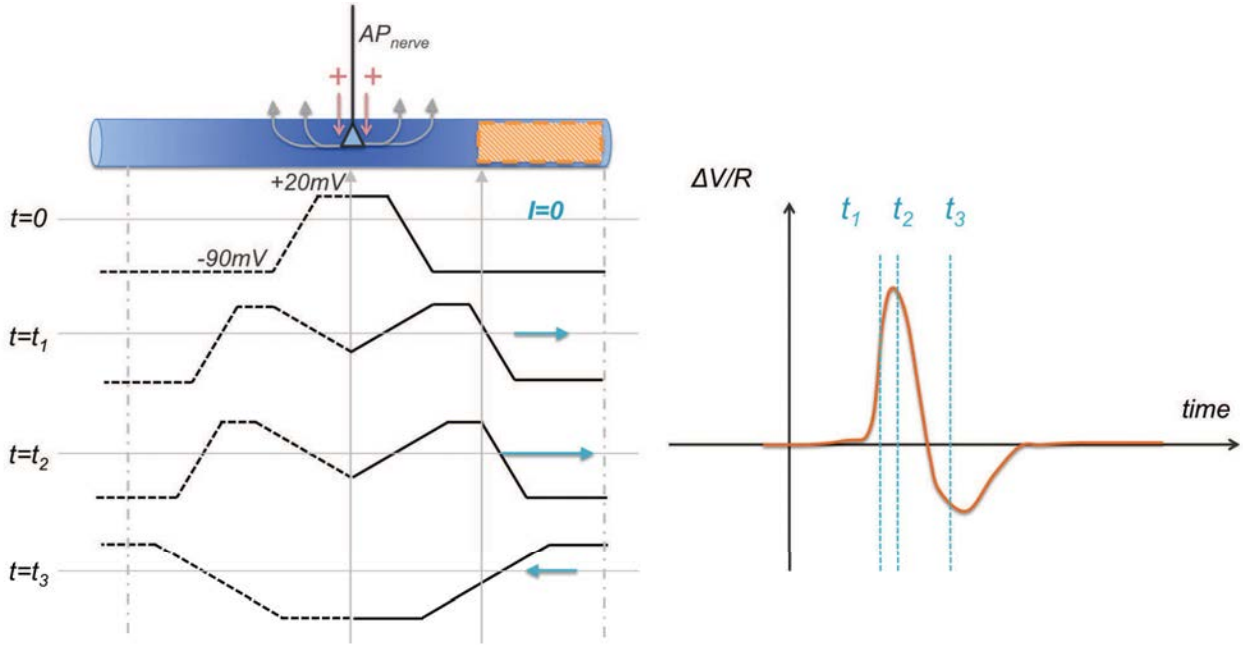

Figure 4.2: AP propagation within the muscle following the nervous AP. Left: Potential as a function of distance in the muscle for increasing time since the AP starts (at $t = 0$). The orange rectangle shows the physical position of the magnetic sensor. The blue arrows show the direction of current on the right part of the muscle. Right: Voltage gradients as seen by the probe over time, which leads to an axial current and therefore a magnetic field.

4.1.1.3 Objectives

So far, only one magnetic measurement on skeletal mouse muscle has been reported with a commercial SQUID gradiometer system [13]. Because of the magnetometer used (a SQUID), the measured signal corresponded to the tangential component of the magnetic field, which is not the direction where the magnetic field is supposed to be strongest. The shape of the signal has effectively an asymmetric bipolar shape and its strength is about 20 pT. The noise of the low Tc SQUID used is about 6 fT/$\sqrt{Hz}$.

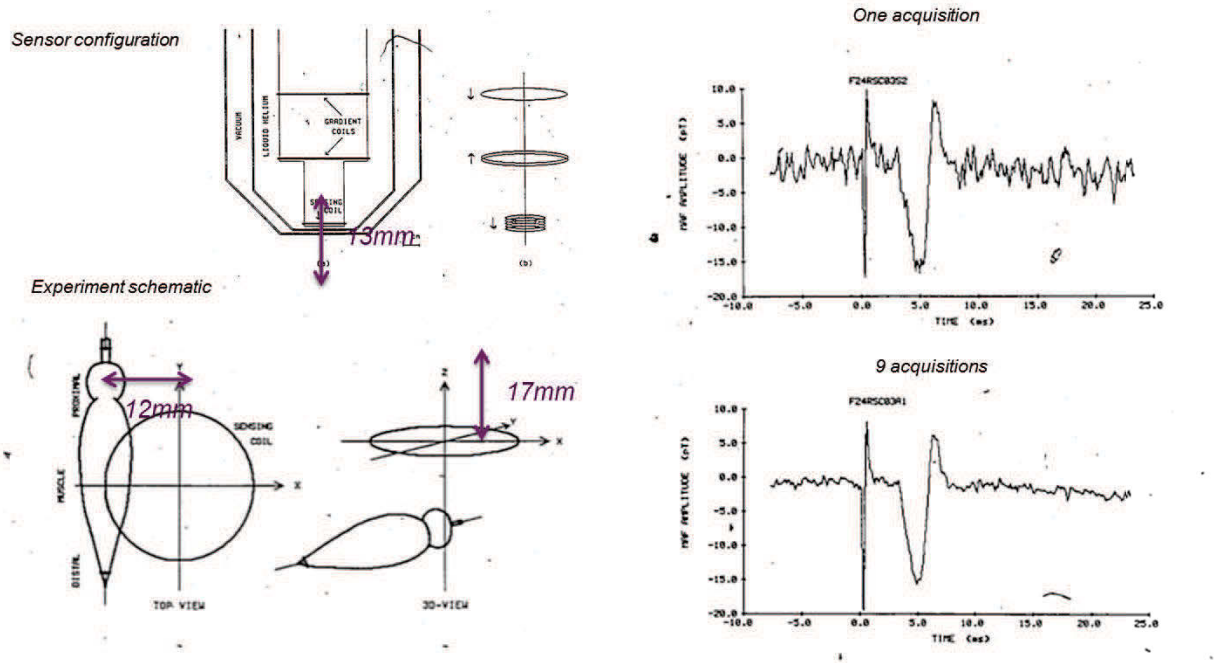

Figure 4.3: Summary of the main result obtained in ref [13]. The signal is measured by a SQUIDs at 4 K placed at 17 mm from a muscle of a Leopard frog.

In this work, we have targeted recordings of the magnetic signals induced by the AP, and linked these results to electrical recordings of the AP, and to LFP signals recorded in the extracellular medium by means also of electrodes. The model is muscle fibers of the mouse soleus. The main goal of this experiment is to test the magnetrode technology with a relatively simple model such as the mammalian nerve muscle junction. The large amount of muscle fibers (600-800 fibers) should produce relatively large amplitude signals (in the range of nT) at high frequencies (in the kHz range) since the investigated signals are in the ms duration range (APs), that is why we preferentially focused on muscle currents rather than on nervous electric signals. Muscle experiments present some advantages listed below:

- Well-known mechanisms
- Large physical dimensions of the muscle allowing large surface sensors, characterized by a good sensitivity and a low noise
- Synchrony of APs in muscle fibers allows to maximize summation on the entire muscle geometry
- Magnetic field component in the plane of the sensor

- Pharmacology can be used to confirm the origin of the recorded signals (see 4.1.3.4)
- External electric stimulation is feasible by applied high voltage by mean of two electrodes immersed in the Krebs solution within the chamber. This can be used in case of nerve damages for example or to induce an AP running from one extremity of the muscle to the other.
- Nervous stimulation can be patterned
- Electrophysiology can be realized (see 4.1.4).

4.1.2 Experiment / Methods

Experiments were performed *ex vivo* on nerve soleus muscle from 3- month old Swiss mice. Mice were anesthetized with isoflurane and cervical dislocated. Dissections of the mice leg were performed within 15 minutes in an oxygenated Krebs solution of the following composition (in mM): 145 NaCl, 3 KCl, 2 CaCl2, 10 HEPES (pH 7.4) and 11 glucose, at relatively low temperature (4°C) to reduce the effect of oxygen deprivation in the metabolism. After dissection, the nerve-muscle preparation was placed into a recording chamber filled with the same standard physiological solution, regularly oxygenated (figure 4.4). The measurements were done at room temperature.

The nerve is sucked up into a glass micro-pipette, of 300-400 µm diameter. The nerve is connected to the muscle through the neuro-muscular junction where synapses convey information (i.e the AP) that will bring the muscle to contract. The muscle, which stretches during the contraction, is held by its tendons with insert pins into the silicone chamber coating.

The nerve is electrically stimulated with 6V, 30 µs voltage steps applied into the suction glass pipette that triggers nervous AP into muscular AP. The muscular AP arises at the center of the muscle, when calcium is released into muscle fibers; this strong depolarization creates an axial current (ions flow) starting at the center of the muscle, propagating synchronously and symmetrically to both ends of the muscle. This current generates a null magnetic field contribution on average over the total length of the muscle, which is why the magnetic recordings are performed on a partial segment of the muscle (see Figure 4.10).

The planar GMR sensor is placed under the muscle to record the magnetic field created by the axial currents coming from the muscle. Sensor dimensions are given in Chapter 3 and were chosen according to the muscle dimensions (typically 1 mm wide and 8 mm length). As

the muscle is placed on top of the probe, the distance between the probe and the bottom of the muscle is of the order of one to few hundreds of um. Two kind of probes have been used for muscle experiments: segment probe which can record at several locations of the muscle, and meander probe which allows measurements on a smaller surface.

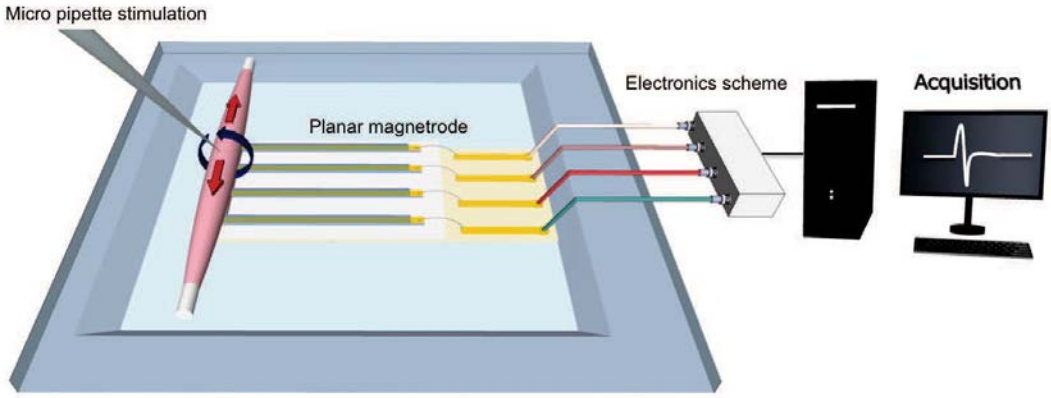

Figure 4.4: Full experimental scheme with planar probe for muscle recording. A nervous AP is generated in the nerve after an electric pulse has been applied within the micro-pipette stimulation. The AP propagates over the muscle, creating muscle contraction. The planar magnetrode is placed below the muscle to record the magnetic AP. The signal is sent to electronics and then to the acquisition chain (see Chapter 3).

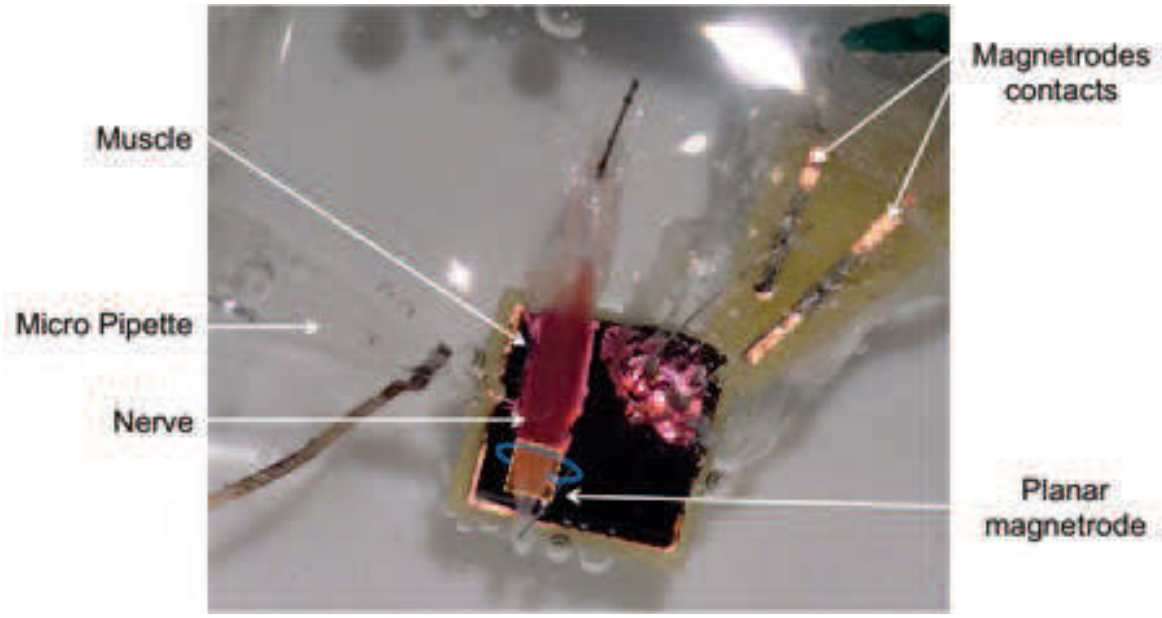

Figure 4.5: Picture of muscle recordings setup. The muscle is held by insert pins into a silicone chamber where the magnetic sensor is fixed on a PCB.

4.1.3 Magnetic recordings

When nerve stimulation occurs, an AP is generated and transmitted along the muscle fibers. The AP reveals local differences in the membrane potential along the fibers, thus generating intracellular axial currents. These currents induce the strongest contribution to the magnetic field but currents flowing within the confined extracellular medium between fibers have a smaller but non-negligible contribution. Extracellular currents flow in the opposite direction and therefore partially screen the magnetic field induced by the intracellular axial currents.

4.1.3.1 Magnetic sensors

Magnetic sensors used for muscle experiment were of two types: a first one has a rectangular shape (segment probe) which is 7 mm long and 500 µm wide with four contacts points to measure either the full length of the muscle or a partial segment; another one has a meander shape which is 1 mm long and 200 µm wide (Figure 4.6). The large physical dimensions of the muscle allow using large surface sensors which is beneficial since high GMR volume gives low noise and a good sensitivity.

Magnetic recordings have been performed either in DC or in AC mode. For the first one, the GMR is fed with a DC bias current (cf Chapter 3) and the output signal is filtered and

amplified on a [10 Hz, 100 kHz] bandwidth with a low-noise pre-amplifier (SR560 Stanford research system) then sent to the acquisition system.

In the AC mode, the GMR is fed with an AC bias current and demodulated at the carrier frequency (typically of 20 - 60 kHz) before being amplified and filtered with the same parameters than for DC measurement. In AC, two outputs were recorded: the magnetic phase that displays resistive variations and quadrature (90° shifted) corresponding to capacitive variations. The typical bias GMR current was chosen as high as possible to enhance the output voltage, the using values were typically 5-15 mA for both AC and DC measurements.

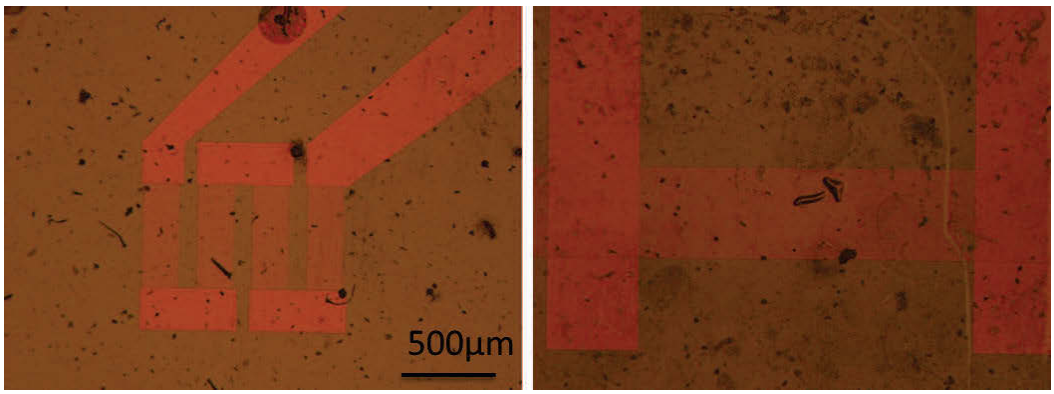

Figure 4.6: Planar probes used for muscle recordings. Meander (left) and a segment (S1) probes.

4.1.3.2 Magnetic signal recordings

Figure 4.7 shows the sensor output voltage as a function of time for two sets of 200 recordings on the same muscle with DC electronics scheme. The interstimulus interval was 1.5 s. A stimulation artefact appears at t = 5.3 ms, which provides a benchmark for upcoming signals; the AP arises about 3-5 ms after the artefact, depending on the trials, which corresponds to synaptic delay. The magnetic AP, generated by axial currents, corresponds to peak-to-peak amplitude of 8 nT in Figure 4.7 but can be reduced after several stimulations, as a consequence of muscle weakening. The biphasic nature of the signal arises from the spatial averaging over the muscle half length ($\sim$ 3 mm): the muscular AP starts at the center of the muscle and propagates along it.

In order to prove that the recorded signal is not an electrical coupling between the probe and the medium, a measurement with no bias current in the GMR was performed in DC

mode (Figure 4.8): the signal disappears when the current in the GMR is switched-off, which is a clear control of the magnetic origin. Nevertheless, a trial with a non-passivated probe was realized to evaluate the coupling amplitude; the results are shown in Figure 4.9 displaying the electrical signature, which is much higher than the magnetic signals seeing previously.

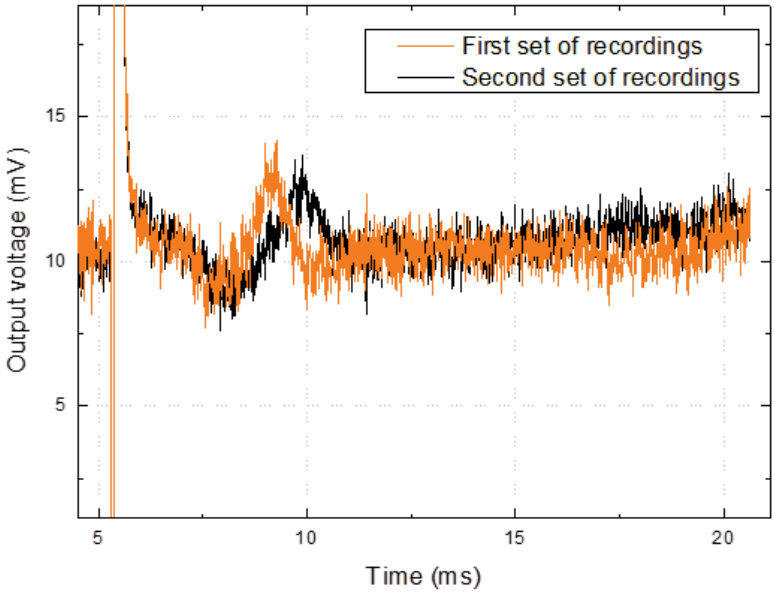

Figure 4.7: GMR output voltage as function of time for two sets of 200 recordings (DC mode) with 15 mA feeding current. The stimulation induces an artefact at 5.5 ms while the magnetic AP starts 2.7 ms after the stimulation. The orange lines were averaged at the beginning of the experimental session, the black one later on. The second averaged signal appears a bit later in time and is slightly smaller; this might be due to the fatigue in the fibers because of the large repetition of activation (few hundreds).

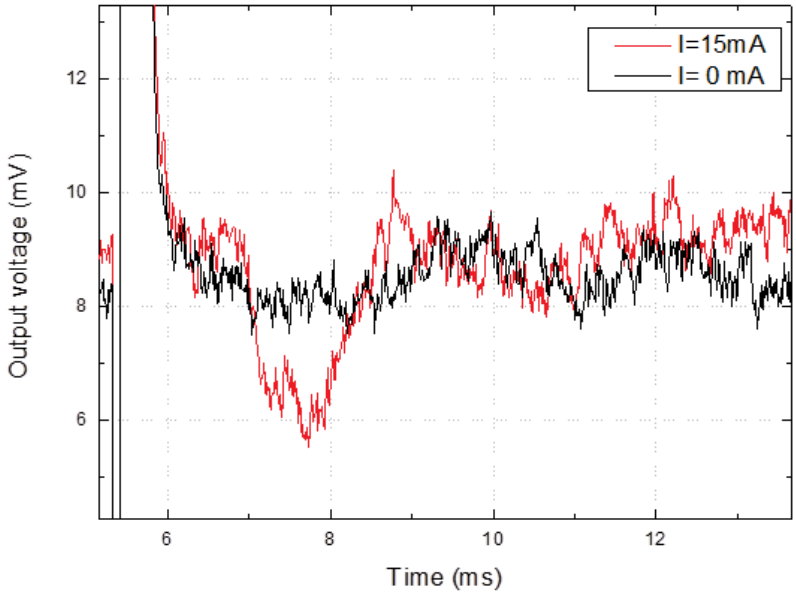

Figure 4.8: GMR output voltage as function of time for two sets of 500 recordings. The measurement has been performed in AC mode with 15 mA current in the GMR. The black line is the baseline where the current in the GMR was switched off, while the red line shows a magnetic AP recorded. One can note that no direct electric coupling appears in the I= 0 recordings.

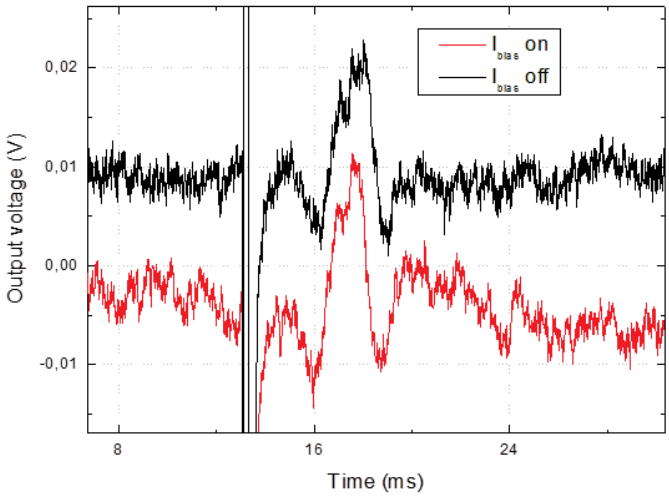

Figure 4.9: GMR output voltage for a sensor exhibiting a poor isolation to the nutritive medium. Here the AP signals is present both with a feeding current in the GMR and without, proving that here the signal is the direct electrical AP.

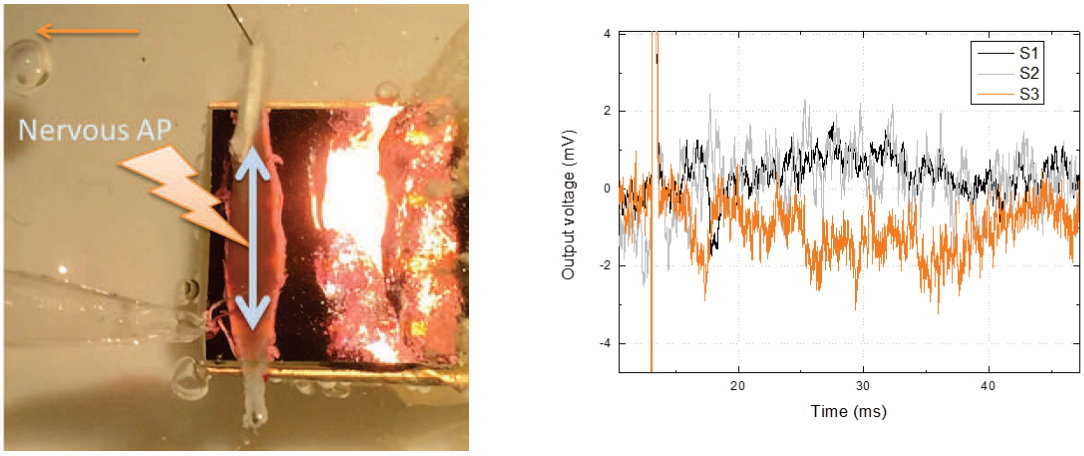

(a) (b)

Figure 4.10: Muscle magnetic recordings in DC mode. a) Picture of the experiment showing the soleus muscle positioned on top of on the planar probe (segments probe). The nerve is sucked up into the stimulation micro-pipette where the nervous AP is generated. The signal is transmitted through synapses (i.e the neuro-muscular junction) in the middle part of the muscle and is transmitted as a muscular AP, on both sides of the muscle where the probe divided into 4 segments is recording. b) GMR output voltage as function of time. S1 is the portion of the probe located on the upper side under the muscle that record a magnetic AP 5 ms after the artefact (black lines). S2 is the segment under the middle of the muscle, where the symmetry cancels out the signal, as it can be seen the response is flat (grey lines). S3 is the portion of the probe on the lower side of the muscle that records the magnetic AP in the opposite way.

4.1.3.3 Geometry study

The muscular intracellular currents are flowing along the y-axis, inducing therefore a magnetic field in the x-axis recorded by the GMR, also sensitive along this direction. Consequently, no magnetic field signal should be present in the y-axis. In order to confirm this field geometry, recordings have been performed with the sensor parallel and perpendicular to the muscle.

Figure 4.11 displays the results for different sensor locations: 0° corresponds to muscle's position where a magnetic field is measured (x-axis) and 90° is the muscle rotated by 90° with respect to the probe long axis. As expected, the magnetic signal disappears when measuring at 90°.

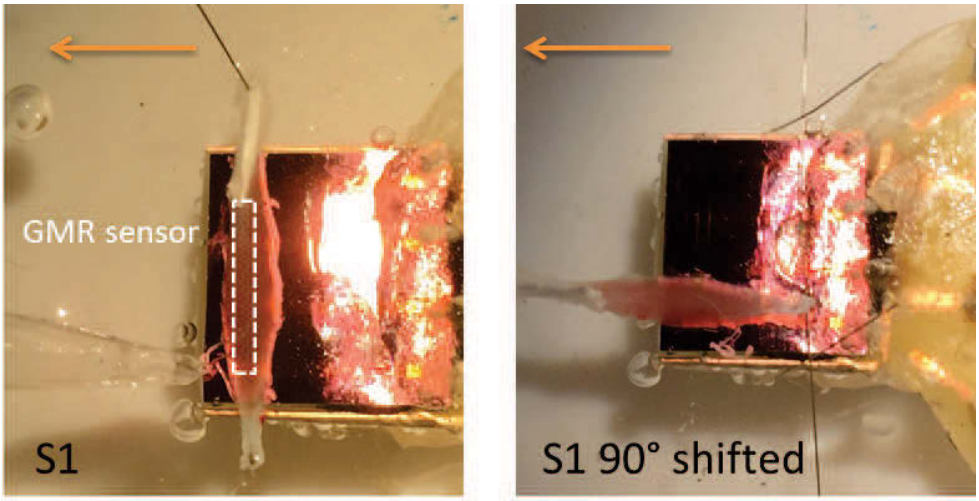

(a)

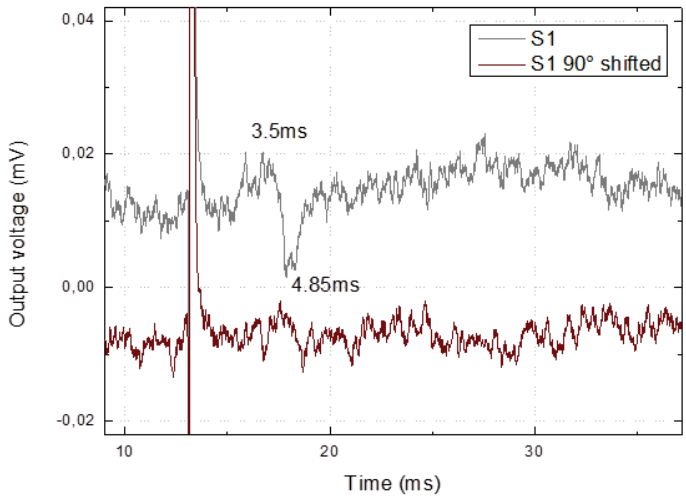

(b)

Figure 4.11: Mean output voltage as function of time (DC mode). a) Left: flat segment probe records the AP perpendicularly to the muscle, seeing the axial current, the corresponding output signal is the grey lines on b). Right: the same experiment with the sensor turned at 90° compared to the muscle, the absence of signal (brown lines on b)) is a clear geometry confirmation. b) the stimulation onset is at 13 ms where the artefact appears. Orange arrows show the sensitive direction of the probe. S1 (grey lines) reveals a magnetic AP with an amplitude of 4.3 nT peak-to-peak while recordings with the muscle at at 90° does not show any magnetic signal, as expected.

4.1.3.4 Pharmacology

Another type of validation has been tested by using pharmacology. A powerful drug, curare, is traditionally used to study the process of synaptic transmission at the skeletal neuromuscular junction. Curare affects the muscular contraction by blocking the binding of ACh to its receptor the end plate potential (i.e the EPSP), the effect leads to an absence of a muscular AP while keeping it in the nerve. Depending on the dose, curare can suppress partially the ACh receptors with low concentration or entirely with high concentration; the last case leads to an absence of AP transmission into the muscle [3]. For magnetrode testing, a high concentration of curare (50 µM) was externally applied into the chamber to block the contraction, the recordings signals are shown in Figure 4.12.

The curare effect is reversible by rinsing the muscle with Krebs solution. After rinsing off the curare, magnetic recordings show a positive response, correlated to the observation of a muscular contraction which was inhibited during the curare application.

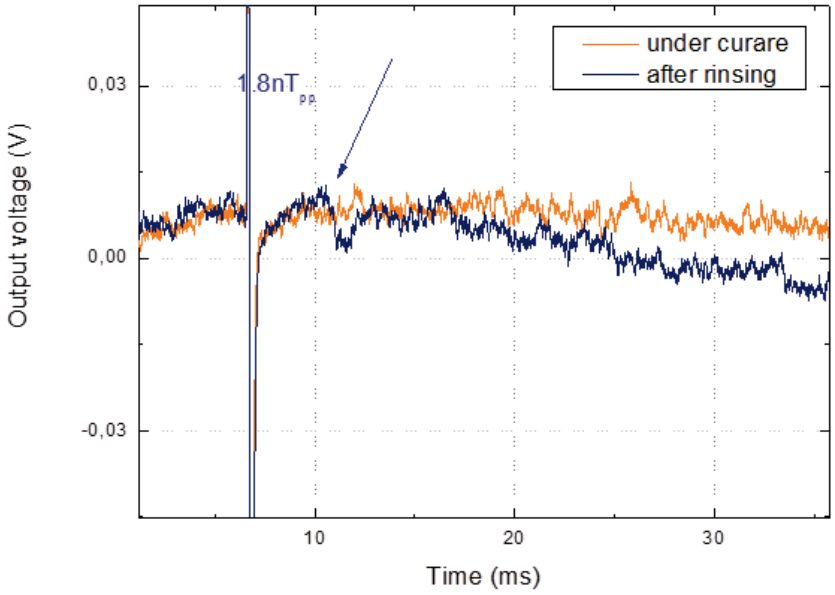

Figure 4.12: Output voltage as function of time on the curare experiment. The blue line corresponds to the magnetic AP recorded in DC mode with planar segment probe (upper side of the probe) after rinsing off curare and orange line displays a clear signal suppression resulting after external curare application. One can note on this experiment that the slow wave which appears after the AP and corresponds to the muscle motion over the probe is absent under current, as the contraction is also suppressed.

Another type of pharmacology could be used; ryanodine is a chemical that blocks the contraction of the muscle but not the PA. It should lead to a magnetic signal but without the slow wave coming from the muscle contraction.

4.1.3.5 Tetanus

Another experimental scheme has been applied, where electrical stimulation is applied to the nerve at a fast repetitive rate; this causes the AP to propagate but the muscle contraction cannot release and the muscle reaches the tetanus state. In the result reported in Figure 4.13 shows a magnetic signature of the order of 3 nT.

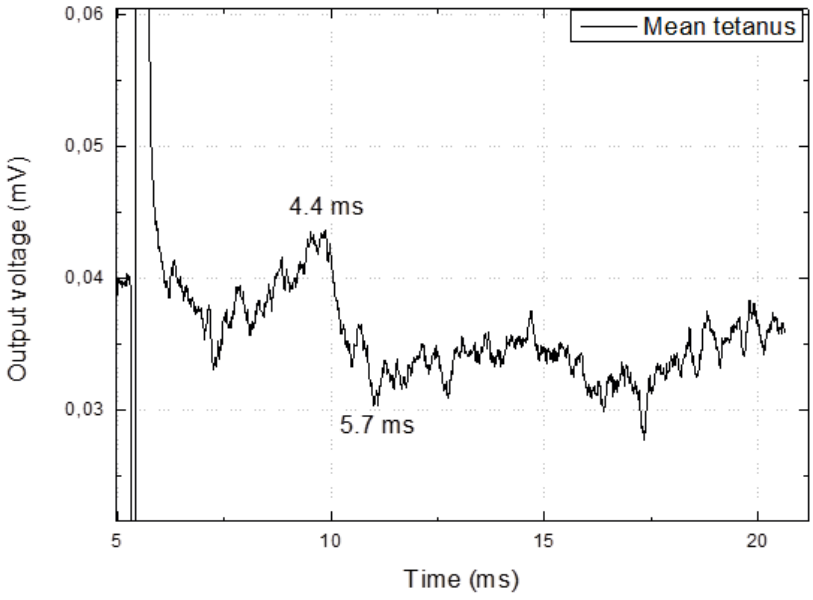

Figure 4.13: Output signal of the probe when the muscle is under tetanus. Very fast electrical stimulations are applied through the nerve, leading to a full contraction of the muscle, but where the AP is still propagating. In these recordings, the noise level recorded is quite high and the magnetic AP is detected because of its specific timing.

4.1.3.6 Artefacts

Muscle motion causes a strong capacitive coupling change between the sensor and the medium, seen on the recordings as a slow wave with high amplitude (Figure 4.14) in the magnetic output signal coming from the sensor. To prove that is was a non-physiological signala basic test was performed to reproduce the muscle motion by passing a cotton bud on the sensor while feeding the sensor in the same conditions than during the experiment. The output signal observed on the oscilloscope was similar in time and amplitude to the one seen during muscle recordings. The artefact was actually caused by a lack of a passivation layer, a protection that was supposed to covered copper paths within the PCB. One way to avoid this artefact was to add insulating layer on the sensor (in some of our experiments with a thin polish layer).

This slow wave appears almost in all the recordings, and can be distinct from the AP

since the muscle contraction appears consecutively to the AP propagation. This signal is also mainly present in the quadrature channel confirming its capacitive change nature. However, a residual magnetic component is observed which is presumably due to the motion of the sensor in the Earth magnetic field created by the muscle contraction.

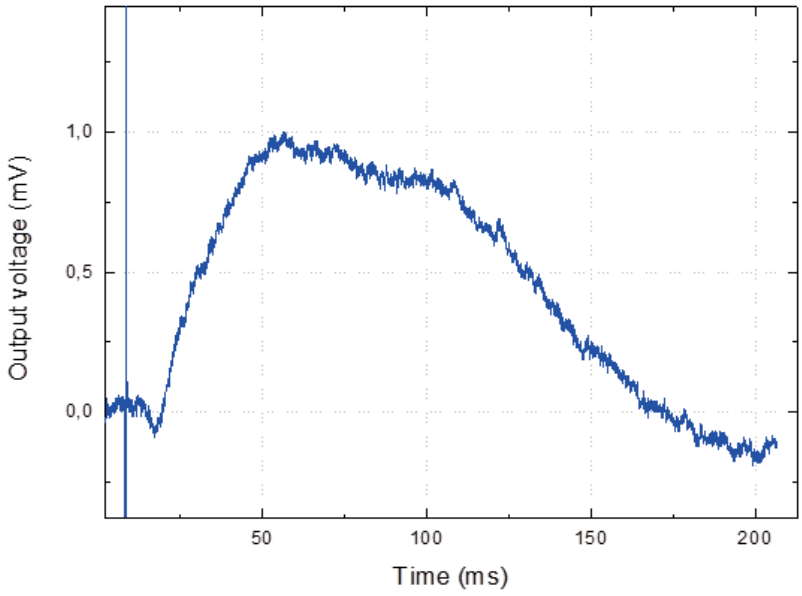

Figure 4.14: Output voltage recorded on a probe with insufficient passivation. A large slow wave appears, linked to the motion of the muscle over the probe. This is probably a consequence of local capacitance value during the muscle motion, which leads to a large output signal change. Improvement of the passivation reduces the value of this slow component, but does not suppress it fully.

4.1.3.7 Signal-to-noise

All the experiment on the muscle have been performed without magnetic shielding. The RMS noise of the laboratory has been measured and at 1 kHz it is about 1 to 2 nT/$\sqrt{Hz}$ so ten times larger than the sensor intrinsic noise. An additional noise is also injected by the stimulation electrode. For that reason, a shielded room was recently fabricated with 1 mu-metal and 1 copper layer to reduce this noise and should give the same signal to noise with only few acquisitions.

4.1.4 Electrophysiology recordings

Due to muscle contraction, conventional electrophysiology recordings were not feasible, therefore, a "floating electrode" recording have been used (technique developed by Gilles Ouanounou at UNIC-CNRS) allowing recording intracellulary the membrane potential while the muscle moves because of contraction.

The electrode is a sharp pipette that penetrates the muscle cells and is made in borosilicate glass with the tip cut at the limit of the pulled zone. The pipette is filled with KCl 3M solution to get a resistance of 40-60 MΩ. A silver wire (10 cm long, 50 µm of diameter) is inserted into the glass pipette and plugged by its opposite to the head-stage of a voltage-follower amplifier where it hangs loosely above the muscle. The floating electrode is inserted vertically into the muscle cells, and its flexibility allows stable membrane potential to be recorded in contracting muscles. Figure 4.15 presents the floating electrode system in the recording chamber on soleus muscle (A) as well as the measured signals coming from a single cell (i.e the membrane potential) which has an amplitude about 50 mV (B) during a repetitive nerve stimulation.

The contraction force is also measured by attaching one of the tendons to a force gauge (B). Moreover, some recordings have been performed to determine the AP propagation speed by measuring along the muscle at different locations: at the center of the muscle fiber, close to the synapse, where the delay between the stimulation artefact and the AP onset is the time for the nervous AP to reach the synaptic cleft; and another point measurement at the extremity (tendon region) (see figure 4.16). The resulting propagation speed is 2-4 m/s (to be compared to 10 m/s in non-myelinated neuron and 100 m/s in myelinated neurons). The electrophysiology recordings have been realized by G. Ouanounou (UNIC-CNRS).

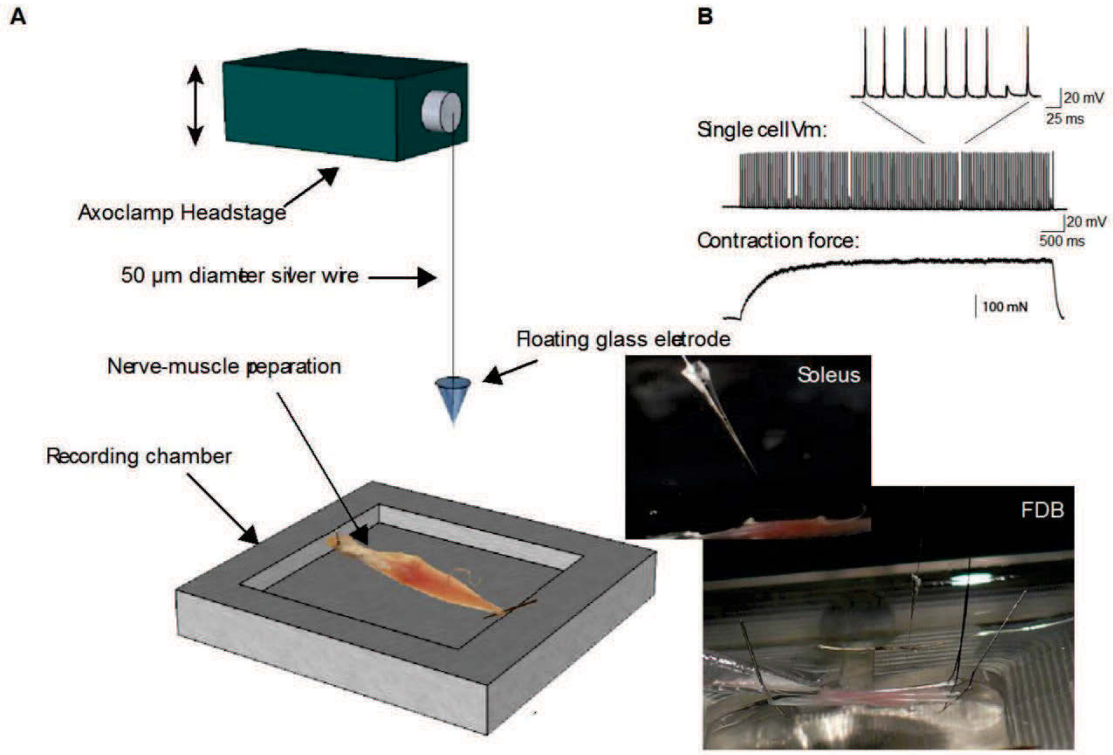

Figure 4.15: A) Schematic of the intracellular electrophysiology recordings, where a floating electrode has been inserted into the muscle to record the AP. The contraction force is recorded through a force gauge connected to one of the tendons. B) shows some typical AP recordings and contraction force. Flexor Digitorum Brevis (FDB) is another kind of muscle located in the leg and is responsible of fingers motion.

Planar magnetrodes perform a spatial averaging over the recording length. Axial resistance being homogeneously distributed along the muscle fiber, averaged axial current can be simply calculated with the Ohm law, using the membrane potential at the two extremities of the recording length. Figure 4.16 shows the averaged axial current in one muscle fiber for a 4 mm segment, calculated from the recorded APs. The resulted biphasic pattern of the axial current in one muscle fiber well matched the pattern of the recorded magnetic field shown before (Figure 4.17).

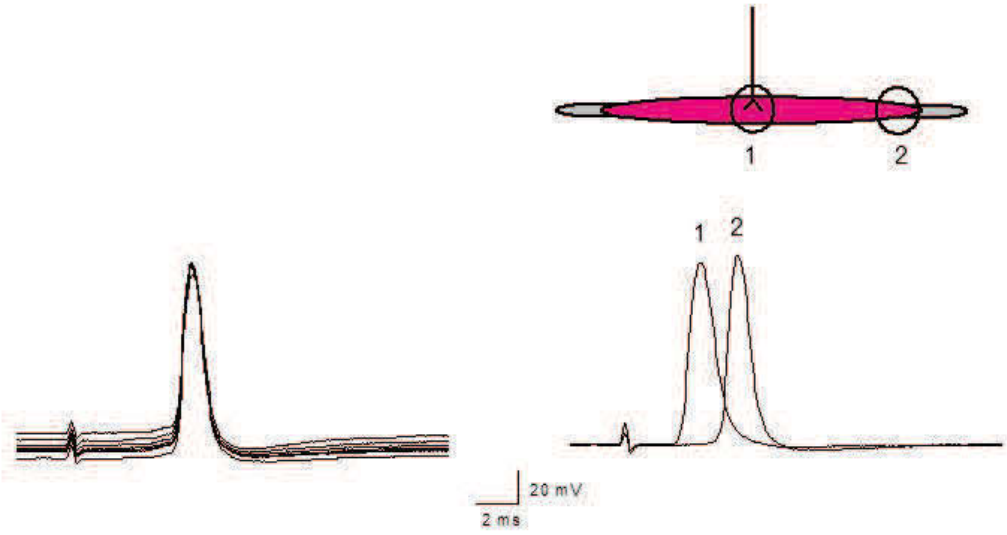

Figure 4.16: AP propagation speed. Left: post-synaptic responses to repetitive pre-synaptic stimulation. Right: APs recorded in two different locations.

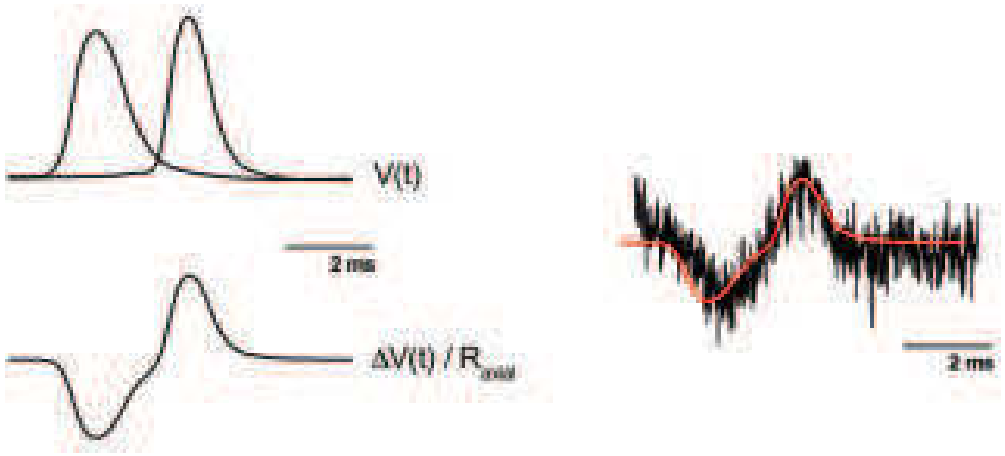

Figure 4.17: Axial current in one muscle fiber matches with pattern of the magnetic field. The small difference in the timings comes from the 4 mm distance between the potential recordings v.s. the 3 mm recording length of the magnetrode.

4.1.5 Modeling

In order to determine whether the amplitude of the recorded magnetic field is compatible with summation and cancellation among the contributions coming from all the muscle fibers, simulations were performed by Francesca Barbieri (UNIC-CNRS) using a computational model reproducing the electrophysiological features of the mouse soleus fibers. In accordance with histological studies, the model was composed by 800 parallel cylinders of 30 µm diameter and 8 mm length, separated from each other by 5 µm. The membrane of each fiber was equipped with a central excitatory synapse, a voltage-gated Na^+ conductance, two voltage-gated K^+ conductances, an inward rectifying K^+ leak and a linear K^+ leak conductance. Simulations were performed with the Neuron software described in chapter 1. Time and voltage-dependency were slightly adjusted as well as membrane density of the different conductances, that were previously established from a voltage-clamp study performed on Xenopus muscle cells in primary culture in order to reproduce the pattern of the mouse AP and its propagation speed (Figure 4.15).

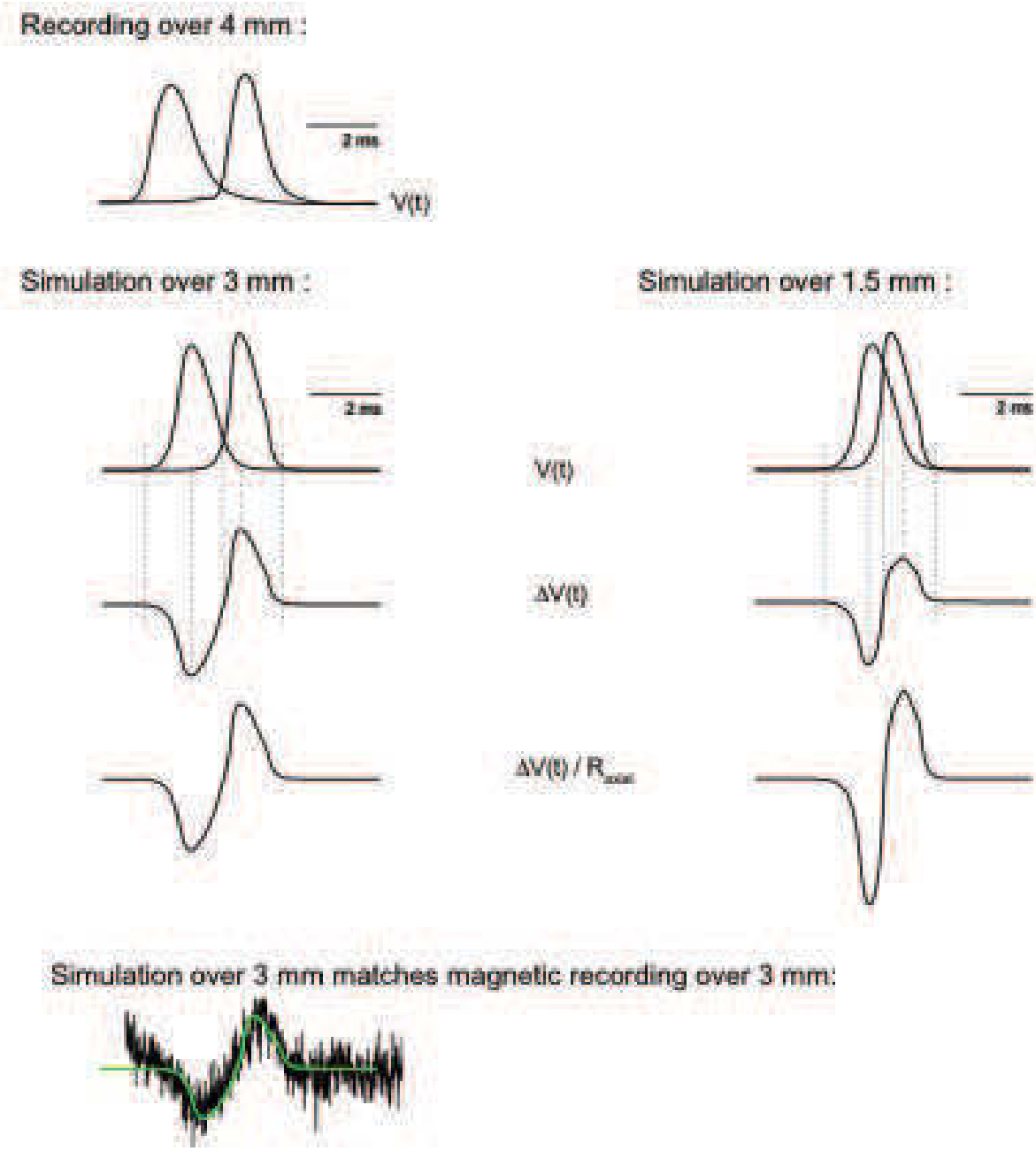

Figure 4.18: Membrane potential simulation over 4 mm, 3 mm or 1.5 mm. Simulations well reproduced the pattern of the APs, as well as the AP propagation speed. The pattern of the axial current in one fiber matches the temporal behavior of the magnetic field recorded with a 3 mm length magnetrode

Simulations provide the behavior of the membrane potential in time and space and of the resulted axial currents in one fiber. The magnetic field generated by all the fibers was calculated using the Biot-Savart law in the vacuum approximation and the superposition principle. The magnetic field was calculated as the average over several positions along a 3 mm length in order to simulate the signal perceived by the probe. The simulated peak-to-peak amplitude was around 8 nT, in agreement with the experimental recordings.

4.1.6 Discussion

In these experiments we were able to record a magnetic AP at local scale. The recordings gave a direct information on the axial current within the fibers, which is not accessible by any other techniques.

The results were in good agreement over time and amplitude of the signals with the data collected from electrophysiology and from the modeling.

Further experiments could be performed, including use of ryanodine to block the muscle contraction and suppress the slow wave signal. Another experimental scheme could comprise a direct external stimulation through two electrodes located on each edge of the muscle, which would induce AP to propagate only in one direction.

Future probes will contains several separated segments associated by independent electronics readout to measure in the same time the response at various positions of the probe.

4.2 Hippocampal slices experiment

4.2.1 Context and Objectives

4.2.1.1 Hippocampus physiology

Hippocampus is a region in the brain comprised in the limbic system, a collection of brain structures on both sides of the thalamus which plays a fundamental role in behavior, emotions and memory. *In vitro* hippocampus brain slices are highly studied in rodents for their involvement in behavior inhibition system, attention, spatial memory and navigation [3, 77]. In this structure can be found pyramidal cells and interneurons that are activated by electrical stimulation, the specific studied regions are CA1 and CA3 (CA means Cornu Ammonis or Ammon's corn).

Action potential are coming from pre-synaptic neurons in the CA3 region, and propagate along the axons via the Schaffer Collateral (SC) to project in the CA1 region, ending

where depolarization trigger neurotransmitters release (figure 4.19). These neurotransmitters (GABA or glutamate mainly) activate pre-synaptic receptors in the CA1 region by opening membrane channels that are ionically permeable. The generated ionic currents thus change the membrane potential of post-synaptic neurons that is measured by means of electrodes.

Many inputs arrive in the CA1 region, all are coming from different regions targeting specific parts of CA1 neurons. The excitatory inputs coming from CA3 through SC arrive to CA1 interneurons and to the basal and oblique dendrites, also to the trunk with a delay due to the synaptic transmission. Nevertheless, the tuft of CA1 pyramidal neurons receives inputs from other structures such as entorhinal cortex and thalamus.

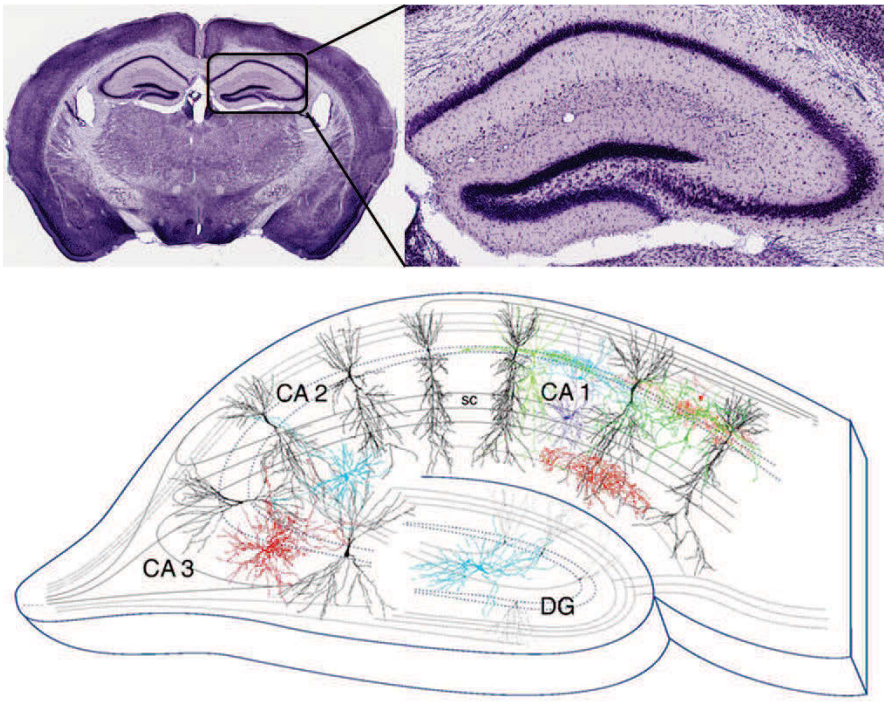

Figure 4.19: Schematic architecture of the hippocampus. Upper left and right panels: coronal plane of mouse brain and zoom-in on the hippocampus. Lower panel: region CA3 send SC (Schaffer Collateral) to the basal and apical dendrites of CA1 neurons that are arranged in a parallel way with all the somata lying on a same layer. Stimulation of the CA3 region produces a burst of synchronous activity in CA1 neurons. Modified from [78]

4.2.1.2 Objectives

Electrophysiologically, hippocampus slices present many advantages including a highly organization of pyramidal cells: neurons are parallely arranged and all the somata are lying on a same layer (cf Figure 4.19), which should provide a summation of the magnetic field.

Hippocampus brain slice is one of the systems of interest for the former magnetophysiology recordings with SQUIDS [79, 37, 1, 32]. Several measurements of Evoked Magnetic Fields (EMF) from transverse hippocampal slices have been reported. A study showed that the evoked magnetic field measured were coming from excitatory post-synaptic currents in the CA1 region while stimulation occurring in the CA3 region, and have 5 pT signal at more than 500 µm distance with 500 averages. S.-I. Kyuhou and Y. Okada [32] have performed similar recordings in a system with 2 mm distance between the SQUID and the slice. They obtained signals with 3.5 pT amplitude maximum field coming from population spikes of ~ 2 mV. Since magnetrode recordings have the advantage of being closer to the sources, stronger MF are expected.

The idea here is to record with both planar and sharp magnetrode the magnetic field (MF) created by ionic currents in hippocampus mouse brain slices. On sharp probes, local measurements are possible.

The targeted signals are the magnetic signature of Local Field Potentials (LFPs) coming from excitatory inputs, occurring between 10-100 Hz and population spikes (PS), in the kHz range. These signals can be obtained by a small population of neurons, either at the microscopic level by measuring within the tissues or by integrated on a larger surface and record at a small distance from neurons.

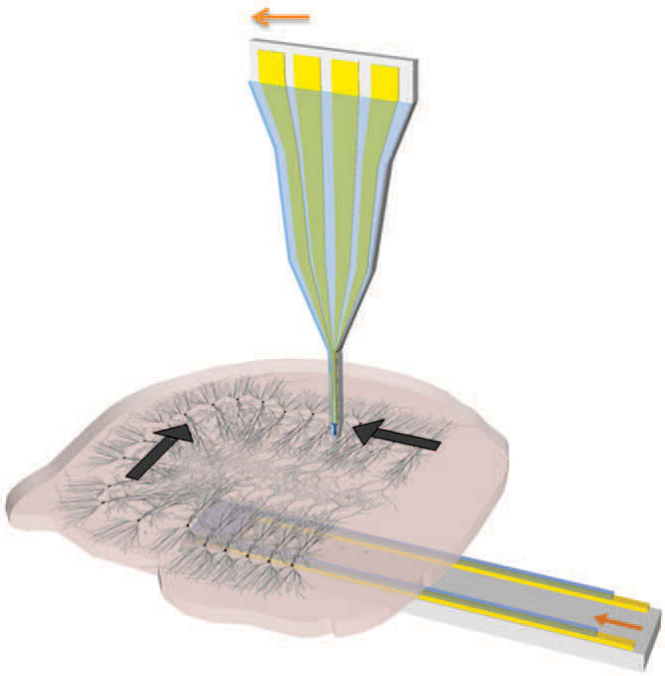

Figure 4.20: Slice setup with sharp and planar probes. Black arrows correspond to the direction of the MF while orange arrow is the sensitivity direction of the probe. Stimulation is applied in the CA3 region and magnetic signals are collected in the CA1 region (sharp probe location on the scheme). Typical thickness of the slice is 300 µm.

4.2.1.3 Simulation

The aim of modeling is to highlight the region where the strongest MF are produced in order to determine the better probe positioning, and to estimate the level of MF signal. MF having an estimation of neuronal current sources (region, shape, amplitude and direction), based on realistic neuron morphology, enable suitable probe design as well as the required probe sensitivity and the amount of averaging suitable to get a signal.

modeling was performed by UNIC-CNRS team, using NEURON software and was first realized on a single neuron with a realistic morphology (Figure 4.21), showing that the strongest current, and so the strongest MF, was produce close to the soma, axon and proximal trunk when neuron is receiving inputs from CA3 stimulation. The inputs are synchronous EPSP that are integrated at the level of the soma and axon to produce a spike. The MF was calculated according to Bio-Savart law in the quasi-static approximation thanks to small distances from sources, and neglecting the volume currents (vacuum approximation). The MF contribution at the dendrites location was nevertheless much lower than in the soma

and axon region because of their parallel-like arrangement which cancel out the contribution. Strongest MF proved to be in the z-component with amplitude of 10 pT at 10 µm from a single cell [80].

The same simulations have been done with 100 copies of the single model neuron, with 5 µm distance between neurons and with taking into account sharp probe's dimensions (40 µm long and 200 µm thick) for spatial average of the field over its length. Again, the simulations display the strongest MF magnitude in the z-direction with amplitude of the average field is of the order of 0.1 nT thanks to summation effects. Moreover, the amount of neurons is higher within the hippocampus slice than the one use for modeling, consequently the recorded signals should be higher. According to these features, a scheme of how the probe should be positioned is shown in Figure 4.26 (for next experiments).

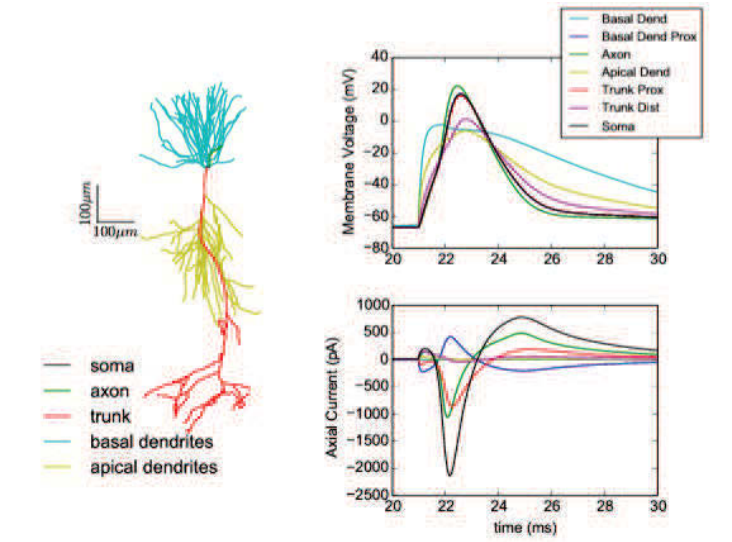

(a)

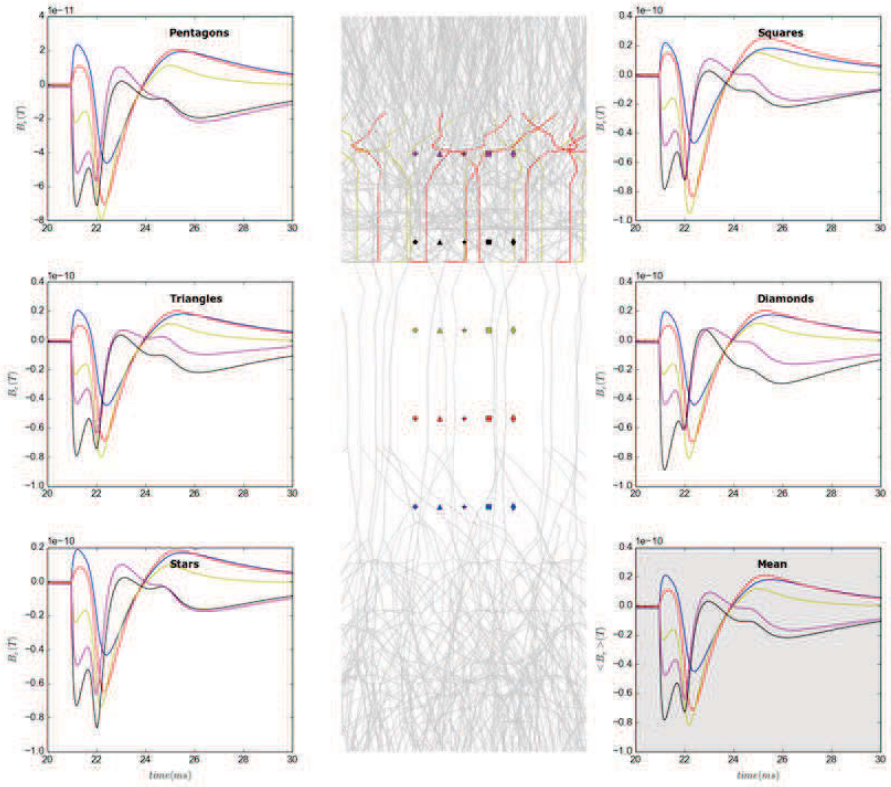

(b)

Figure 4.21: Neurons modeling. a) Membrane potential and axial current vs time in different part of the neuron. Strongest currents are flowing in the axon, soma and proximal portion of the trunk. b) z-component of the field produced by a population of 100 neurons firing synchronously after stimulation on CA3. Bottom left panel shows the average field over the length of a sharp probe (40 µm). Courtesy F. Barbieri.

4.2.1.4 Slice experiments

Both planar and sharp probes have been tested on hippocampus slice setup. The first ones measure the magnetic signature coming from neurons network above the slice while sharp probe penetrates into the slice to be as close as possible to a population of neurons. Magnetic recordings were performed for both planar and sharp in the CA1 stratum Lacunosum Moleculara during electrical stimulation in the Schaffer collateral (CA3 stratum radiatum) by means of tungsten electrodes targeting excitatory cells. An LFP probe was inserted into the CA1 region (close to the sharp probe) to measure simultaneously the electric signature of neuronal activity. A picture of the setup is shown in Figure 4.24.

The animal (Swiss mice-1 month old) was anesthetized with isoflurane and cervical dislocated. The dissection consists of isolating the hippocampi, then align and slice it to obtain 10 slices which can live up to eight hours at room temperature. The slices are deposited in Haas interface chamber. An LFP probe was then inserted into the slice to get the electric signature of the recordings and it allows sharp magnetrode positioning. Stimulation is sent in the SC which consists of short paired pulses while magnetic recordings are in the CA1 region. The stimulation is 2×0.3 ms pulses 100ms apart (start of the 1st to start of the 2nd), repeated every 6 seconds. The amplitude of the stimulation is ranging between 0.1 and 1 nA (varied per experiment to reach to current necessary to have a clear LFP of the 1st population spike).

Planar setup Planar probe was mounted on a PCB covering by a blotting paper to let the nutritive liquid flow within the slice (Figure 4.22). As explained previously (chapter 3, packaging), the probe is wire bonded by aluminum wire and encapsulated with araldite (glue) to get a perfect isolation from the medium. The PCB was then fixed into a Teflon ring, with dimensions adapted to the Haas chamber (Figure 4.22). The slice is then deposited above the sensor. One should note that the upper layer of the slice (the one in contact with the sensor) is not receiving oxygen/bubbling, hence a dead layer was formed (around 100µm) which increase the distance between the sensor and signal sources. The dead layer could also make the lifespan slice weaker. The using probe was a GMR rectangle (200 x 400 µm) with a resistance of 30 Ω with a MR ratio of 6 % and a sensitivity of 9.5 and 6.5 %/mT. Sensor was mounted in the AC mode with a feeding current of 10 mA (300 mV) and a carrier frequency of 64,111 kHz.

Several trials were performed with planar sensors but several issues compromise the recordings after 400 recordings. The two major issues were the lifespan of the slice which was

limited due to the lack of oxygenation in the upper layer, which causes damages to the slice. The second issue was coming from the glue protecting the sensor which was corroded by the medium and the bubbling; hence the probe was non-covered anymore. Next recordings are scheduled with a fully-encapsulated probe.

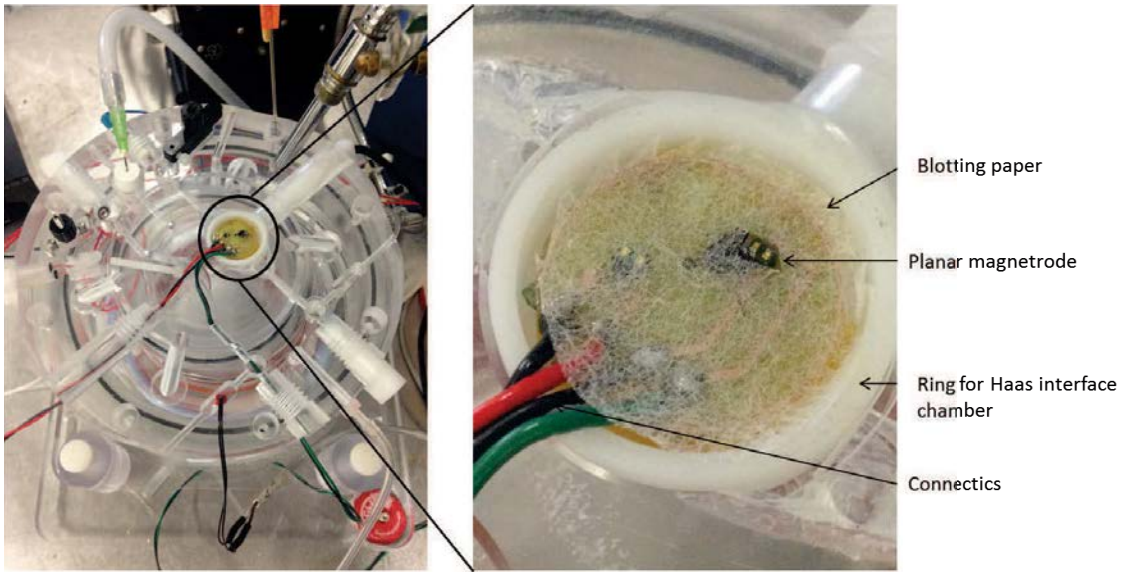

Figure 4.22: Planar sensor for slice setup. Left: full view of the sensor mounted on the interface chamber at UNIC-CNRS. Right: close-up view of the sensor in the chamber.

Sharp setup The sharp setup is roughly the same as for the planar one except for probe positioning: the goal here was to approach the sensor above the slice, to get closer to the tissues by penetrating the slice with sharp magnetrode (Figure 4.24). Several probe designs have been investigated, with regard to the dimensions of the slice and the field direction.

The sensor used for the first experiment is a sharp magnetrode (#M11G) containing two yokes (3 µm wide and 30 µm long) and of resistance R= 240 Ω). The sensitivity of the sensor was 1.2 %/mT with a magnetoresistance (MR) of 4.48 % (Figure 4.23) with a field equivalent noise of 20 nT at 10 Hz and 2 nT at 1 kHz. Only one sensor has been used (up yoke) because of a corrosion issue with the other one (bottom yoke), making a shortcut with the medium.

Measurements were performed in AC mode (frequency modulation) with a 400mV alternative bias voltage applied in the sensor. The frequency modulation chosen was 64.111 kHz (decimal number was chosen to avoid any 50 Hz harmonic contaminations) and the feeding voltage for demodulation was 2 V for each channels (magnetic phase and quadrature). The output is then sent amplified (G = 20000) and filtered by two low-noise amplifiers (Stanford)

with a bandwidth of [1 Hz -10 kHz] to target both slow and fast events (i.e LFPs as well as spiking activity). During the acquisition, a high noise level has been observed (few hundreds of nT rms), mainly because of a lack of shielding inside the recording chamber. Moreover, the bubbling system is a high noise source that has a strong impact on the output sensor.

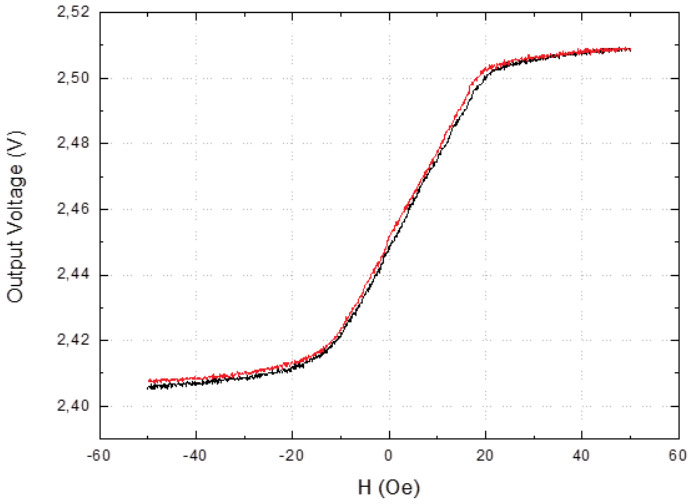

(a)

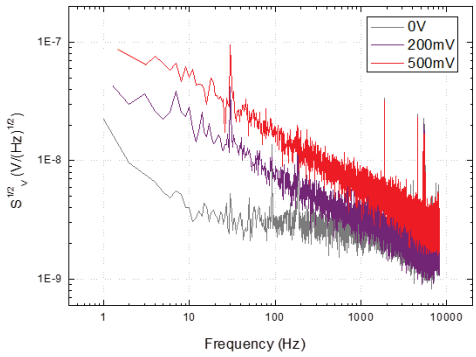

(b)

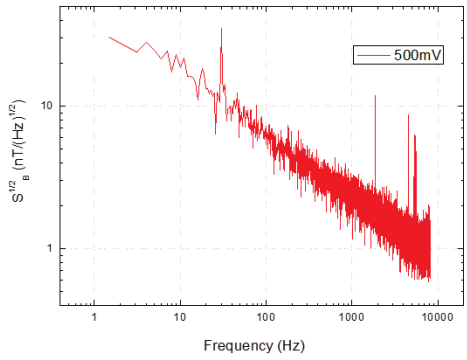

(c)

Figure 4.23: Sharp probe calibration (#M11G). a) R(H) on 3x30 µm yoke. The probe exhibits a linear, non-hysteretic response with a MR of 4.48 % and a sensitivity at zero field of 1.2 %/mT. b) Voltage noise as function of frequency. c) Field equivalent noise as function of frequency

Frequency	10 Hz	30 Hz	1 kHz
Voltage noise	20 nT	11 nT	2 nT

Table 4.1: Noise characteristic #M11g

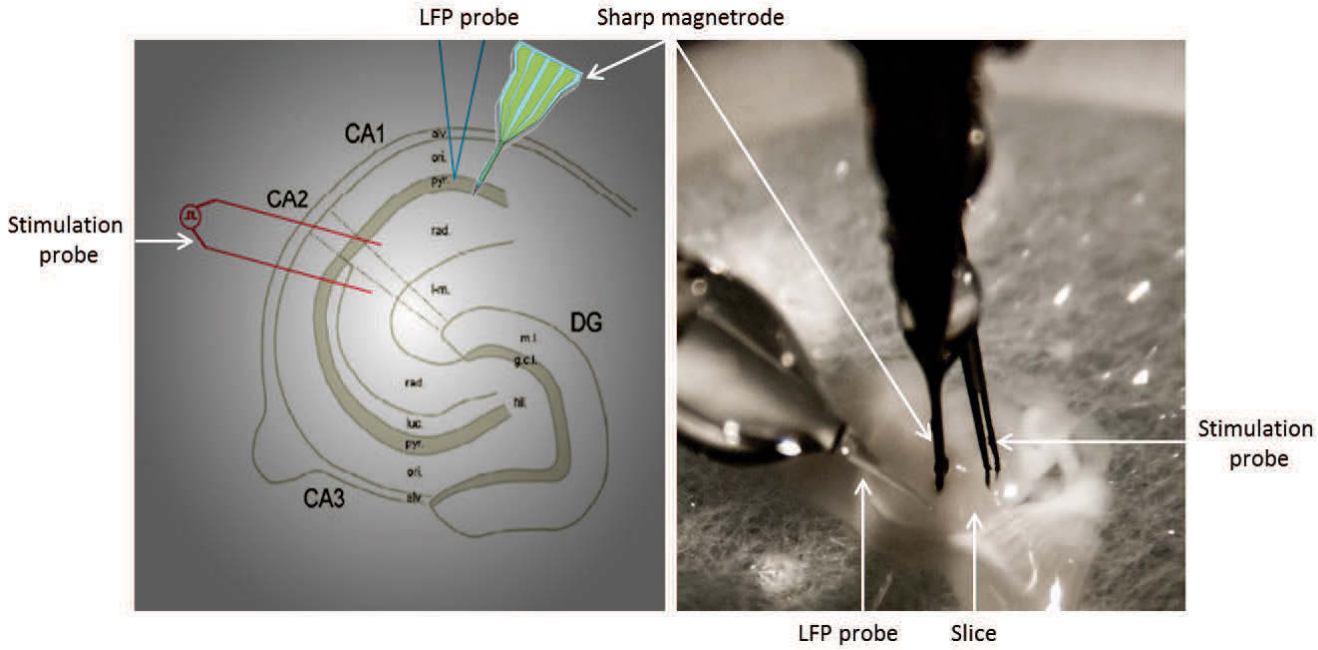

Figure 4.24: Hippocampus slice magnetic and electric recordings. Left: Schematic view of a the slice, sharp magnetrode was inserted close to the LFP probe. Right: Picture of recordings. Modified from [81].

4.2.1.5 Magnetic recordings with sharp probes

Figure 4.25 shows the recordings with the sharp probe and the electrical control with the LFP probe. The evoked potentials recorded in the CA1 region arise few ms after the stimulus (electric channel on figure 4.25). The stimulation probe sends a pulse train (2 x 0.3 ms) at 20 ms (onset) which is repeated after 100 ms. This electrical stimulation produces an artefact that is seen by both magnetic and electric probes (large sharp signal at 20 ms). Because of its large amplitude, the magnetic sensor output is saturated for a short period (typically few ms), a latency where biological signals are expected. This delay can thus hide fast neuronal events (such as spikes). A digitally filtering can be applied to reduce the artefact amplitude.

On the electrical recordings, one can observe an evoked few ms after the stimulation artefact, this response being higher after the second stimulus. This is mainly due to facilitation process; a first AP leads calcium voltage-dependent channel to open and let calcium join the inward synapse, thus conduct to release neurotransmitters in the synaptic button. When a second AP arises quickly after the first one, intra-synaptic calcium is still present in the synaptic button that induces a high calcium concentration inside the synapse. This explains the larger amplitude in the second recording (both electric and magnetic) on Figure 4.25. Magnetic in phase output is shown in Figure 4.25 after electrical stimulation. Here also an evoked response is observed on a proper timing with respect to the electrical recordings. Nevertheless, the amplitude of the corresponding magnetic field signal is too high (of the order of 1 µT) to be a pure magnetic component. The signal might be mainly due to direct electrical coupling to the ERP component.

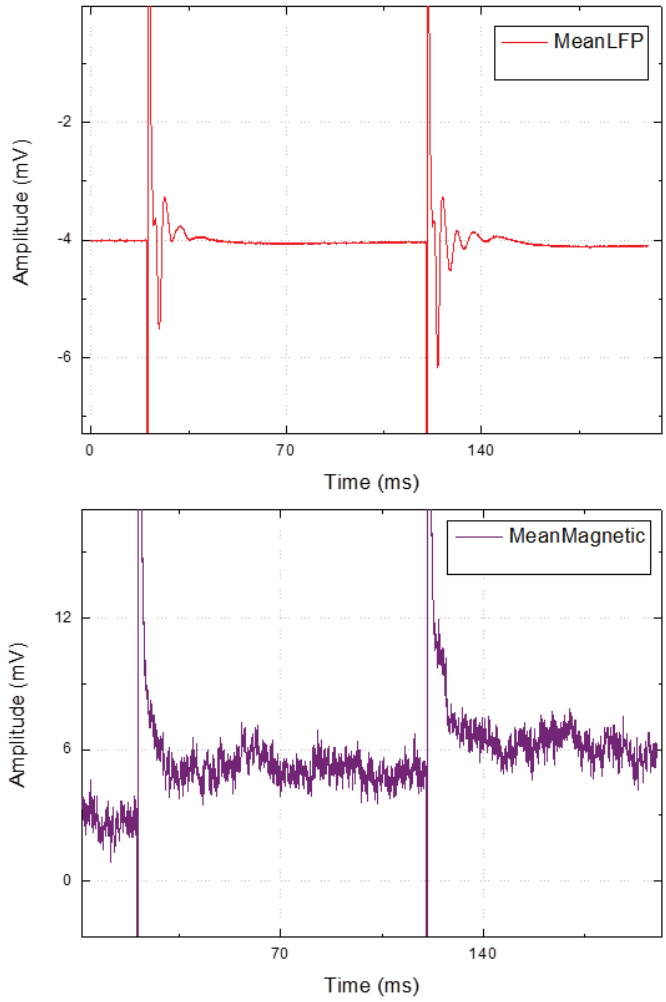

Figure 4.25: Hippocampus slice recordings: Output voltage (mV) as function of time (ms). Top) LFP recordings averaged over 1000 acquisitions. Bottom) Output voltage of the sharp GMR sensor. The signal amplitude in equivalent field is 1 µT, which leads to suspect a direct coupling.

4.2.1.6 Conclusion

First *in vitro* recordings on hippocampal brain slices have been performed using magnetrode technology. However, the amplitude of the signal found, typically hundreds of nT is too large compared to what is simulated and it is presumably an artefact. The noise level recorded on the interface chamber is extremely high and leads to a rms noise much higher than the intrinsic noise of the sensor.

Two main improvements are now being implemented. The first one is a new set of probes designed with better sensitivity, able to record either on the surface of the slice or within the slice, and with an optimized insulation layer. Planar probe setup (probe and wire bonding) must be protected in a full enclosing system (araldite) while sharp probe should include an electrical measurement point to record simultaneously magnetic field and electrical activity. New *in vitro* probes were designed with a penetration angle slightly reduced (40° instead of 20°) and including an electrode made in platinum. The second improvement is the development and the construction of a shielded structure around the *in vitro* recordings experiments. This two layer shield (copper and mu metal) will reduce strongly the RF noise, the 50 Hz contamination and the low frequency noise, to achieve an environmental noise not larger than the noise intrinsic noise. Lastly, other stimulation schemes could be used, for instance inducing an epileptic seizure which would lead neurons into a synchronous burst of activity that could conduct to strongest MF.

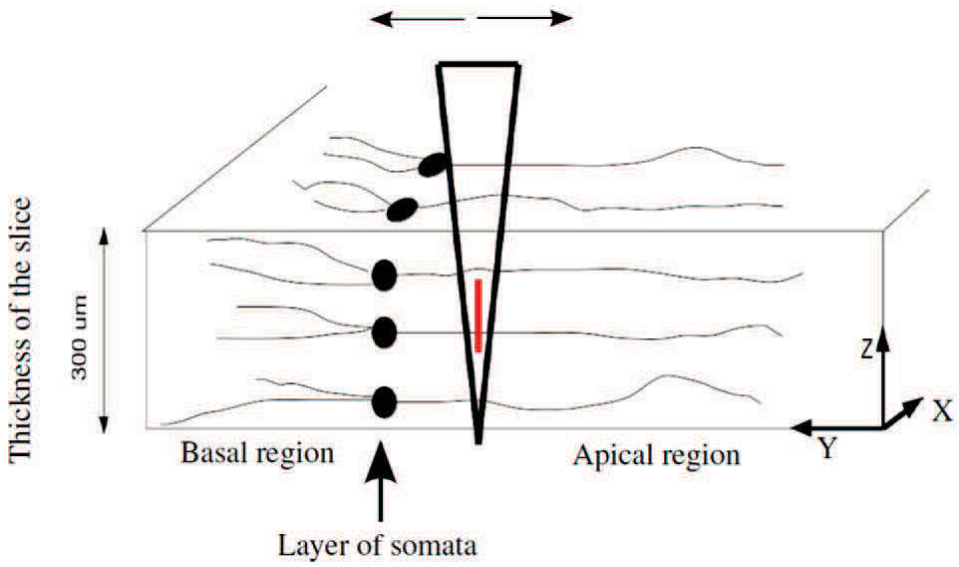

Figure 4.26: Schematic view of probe positioning within the hippocampus slice. The black dots represent the somata and the red line is the required sensitivity direction of the sharp probe. The expected strongest MF produced by a population of neurons is in the z-direction.

Chapter 5

In vivo recordings

All the recordings presented in this chapter have been realized at Ernst Strüngmann Institute, in collaboration with Max Planck Institute at Frankfurt, with the team of Pascal Fries; Thomas Wünderle, Chris Lewis and Jianguang Ni.

All procedures in this study were approved by the Ethics Committee of the state of Hessen in accordance with the guidelines of the German law for the protection of animals.

5.1 Objectives

One of the main goal of this thesis is to perform magnetic recordings of the local neuronal activity. The reasoning behind neuroelectric signature is well known thanks to *in vivo* electrophysiology, by means of inserted electrodes that record the potential variations within the cerebral cortex (cf Chapter 1, section 1.1). Noticeably, the magnetic signature induced by the neuronal currents is accessible through MEG, which provide neuromagnetic field mapping outside the head using SQUIDs (cf chapter 1, section 1.3). One of the major constraints in MEG is the localization of the sources, known as the *inverse problem,* where model parameters have to be estimated from MEG data, assuming a dipole current model [32]. The primary difficulty for this problem lies in the lack of measurements at local scale, which require high sensitive and small magnetic sensor. In this study, we used sharp and planar magnetrodes presented in Chapter 3 to perform *in vivo* magnetic measurements.

The studying model is the primary visual cortex of anesthetized cat, which is commonly used to perform *in vivo* electrophysiology, providing insights about visual and cerebral processing. Indeed, visual cortex induces evoked neuronal responses when presenting visual stimuli in the eyes; those visually driven evoked responses can trigger neurons to fire several

tens of spikes per second that can be record electrophysiologically.

Standard anesthetized cat experiments use micro-electrodes, either sharp or/and surface (ECoG) to record extracellular neuronal signals (mostly LFPs and Multi-Unit Activity (MUA)). Sharp electrodes can also record single neuron spikes, however, limited to the nearby neurons, and for a limited number (from one to maximally a dozen of special tetrodes [14]). The electrode tip is separated from the surrounding neurons by the neuropil, a very dense mesh of neuronal membranes that strongly attenuates currents on their way from the generating neurons to the electrode tip. By contrast, magnetic field can travel almost freely through the neuropil, which means that a magnetic measurement might be able to sense spiking activity of hundreds of neurons in its vicinity, giving information about spatial arrangement at local scale within the cerebral cortex. Besides magnetic recordings, having simultaneously access to the local potential variations is very helpful to reconstruct the EM field in the probe neighborhood; thus, an electrode contact was integrated on sharp magnetrode.

Two kinds of magnetic probe were developed to sense the stimulus-induced cortical responses:

- Planar probes (ECoG-like) that contain a rather large GMR element to record at the surface of the cortex,
- Sharp probes with either one or two GMR sensors with various surfaces magnetic sensing elements are used as depth sensors. An electrode is located on the tip of the probe to have a local reference of the LFPs.

Figure 5.1 gives a schematic view of the experiments which were performed at ESI.

The cat primary visual cortex is located on areas 17 and 18 (red spot - left scheme on Figure 5.2) while area 21a is a higher visual area (red spot - right scheme Figure 5.2)[82]. When a visual stimulus is presented to the cat's eyes, either by projecting gratings on a LCD screen monitor or with a direct light in the eye (LED), the optical signal is transformed into nervous signal traveling through the optical nerve and transferred to primary visual cortex for cerebral processing where spiking and extracellular activity into neurons can be measured. As visual processes are antisymmetric, visual stimulus seen by the right eye will activate neurons in the left hemisphere. The response signals are Evoked Response Potentials (ERPs) correlated with the visual stimulus, and arising after a synaptic delay.

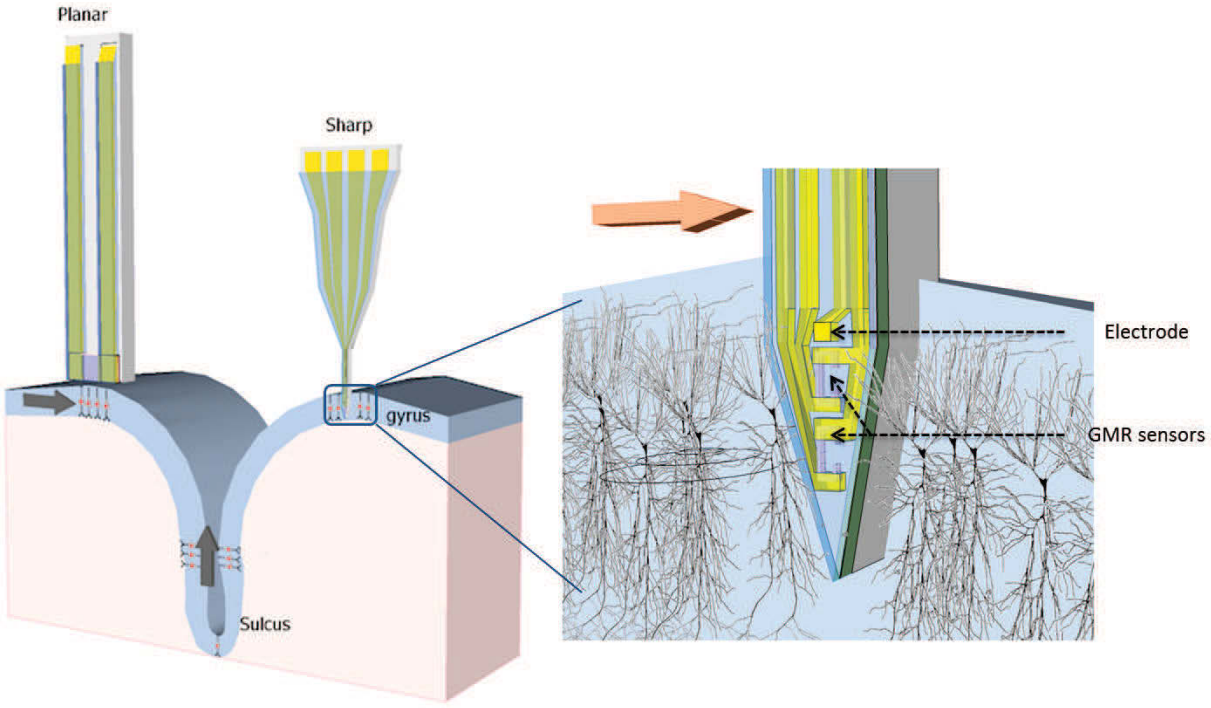

Figure 5.1: Schematic of the *in vivo* recordings: cerebral cortex is represented in blue and pyramidal neurons are aligned perpendicular to the surface. Planar probes record local magnetic features without penetrating the cortex while sharp magnetrode (zoom-in on right) goes through the cortical tissues. Black arrows represent the magnetic field that neurons create, perpendicularly to the major axis of the neurons neurons, and the orange narrow is the sensitivity direction of the sensor. Besides magnetic recordings, local electrical activity is measured by means of an electrode on sharp probe.

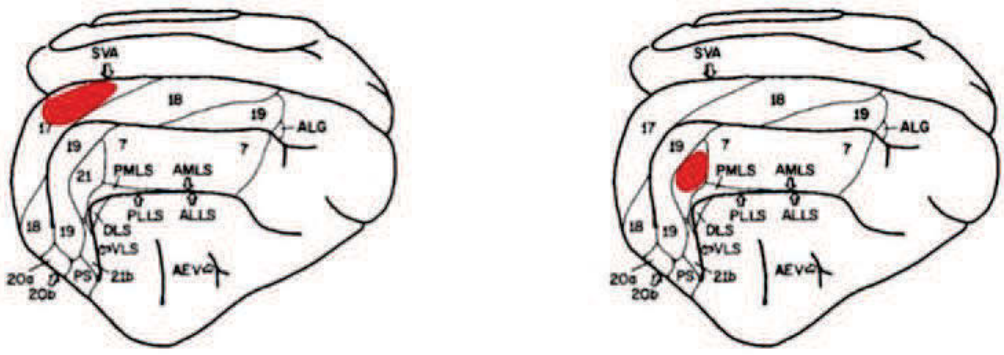

Figure 5.2: Cat's cortex. The red dots show area 17-18 and 21a, where the recordings have been performed. Courtesy Thomas Wünderle.

5.2 Experiments / Methods

5.2.1 Sensors

Both type of sensors (planar and sharp) tested are sensitive either to tangential or to radial magnetic field (cf Chapter 3). All the probes are encapsulated (except for the electrode) and connected to the electronics system (AC or DC mode) and fed in a commercial recording system (Tucker Davis Technologies) where the signals are amplified and digitized. All the probes were previously calibrated with a coil by sending a known magnetic signal at a given frequency on the sensors (Chapter 3). The sensitivity in V/T is then known for a given bias voltage of the GMR.

5.2.1.1 Planar sensor

Two kinds of flat sensors have been used for *in vivo* recordings (cf Chapter 3): the first ones are sensitive to the tangential MF direction while the others are sensitive to the radial MF direction. Each sensor is mounted on a long PCB containing the copper lines for the sensor feeding and output, held by its extremity with a micro-manipulator to keep the sensor motionless during measurements (Figure 5.3). Due to its large GMR volume, a small bias magnet was added to compensate the coercive field (see Chapter 2 and 3); Figure 5.4 gives the R(H) response before and after field compensation. The sensitivity of the sensor is 7.34 %/mT with a total MR of 6.6 %.

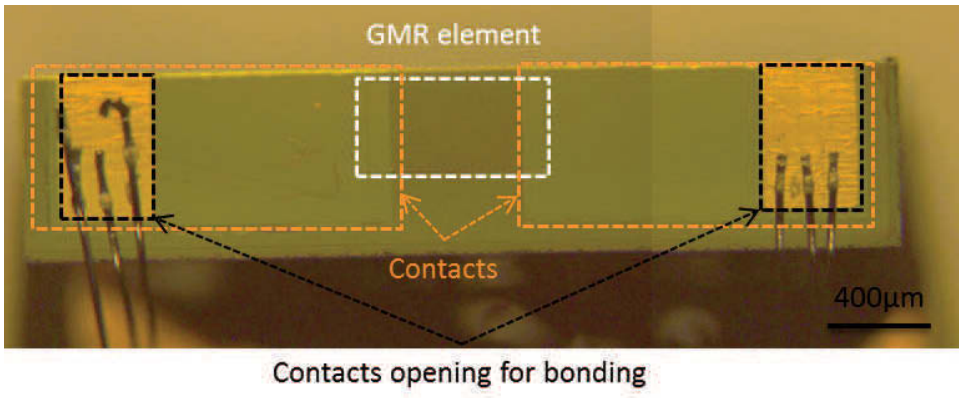

Figure 5.3: Planar sensor ECoG-like for *in vivo* recordings: A single GMR element (400 x 800 µm), wire bonded. The GMR element is highlighted by the dashed white box; the contacts are shown in the orange dashed boxes, while the contact openings are delimited by the black dashed boxes.

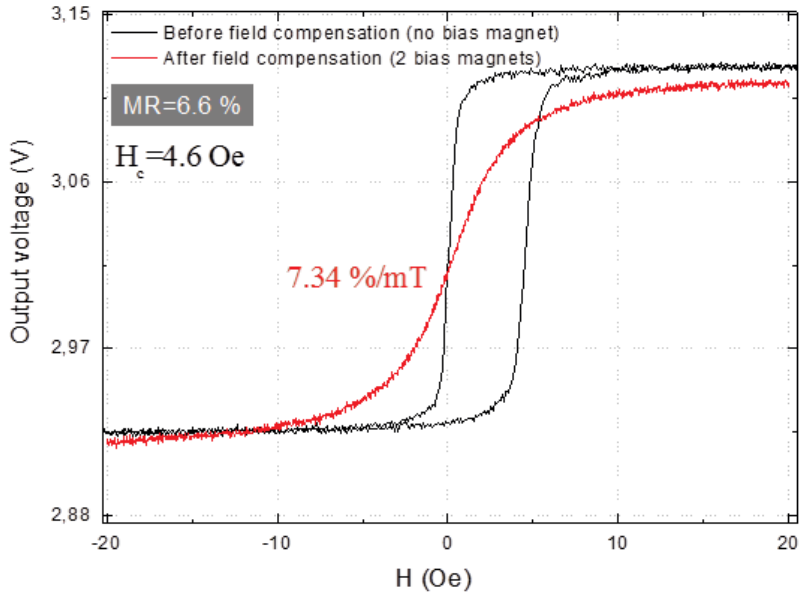

Figure 5.4: R(H) response of the ECoG sensor before and after the magnets mounting.

5.2.1.2 Sharp sensors

Sharp sensor design has been adapted to electrophysiological probes, with a substrate shaped in a needle with a penetration angle of 18°, a width of 100 m and 200 µm thickness (cf Chapter 3). Sharp magnetrodes have one or two magnetoresistive elements located on the tip of the probe, to allow recording a single channel, two channels separately or in a gradiometer configuration. All sharp probes contain an electrode element made in gold or platinum, close to the magnetic sensors (typically less than 100 µm away from MR sensor). This gives access to local electric measurement such as LFP signals and potentially spikes, like those present on the tungsten control probe, a hundreds of microns away from the magnetrode.

One of the inserted magnetrode (#M19Evans) displayed a MR ratio of 6 %, a sensitivity of 1.9 %/mT and a thermal noise of 300 pT/$\sqrt{Hz}$. Figure 5.5 and table 5.1 gives used probe characteristics. During recordings, #M19Evans probe was fed with a bias voltage of 1 V_{pp} corresponding to a sensitivity of 14 V/T.

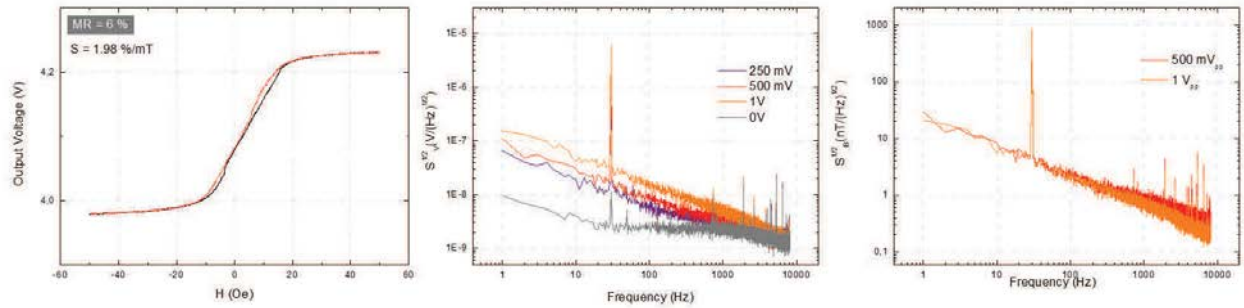

Figure 5.5: Sharp magnetrode characteristics. Left: R(H) response of #M19Evans probe with a resistance R_0= 820 Ω, a MR ratio of 6 % and a sensitivity near zero field of 1.9 %/mT. One can note the linear response of the GMR. Middle: Noise voltage spectrum as function of the frequency. Right: Field equivalent noise as function of frequency.

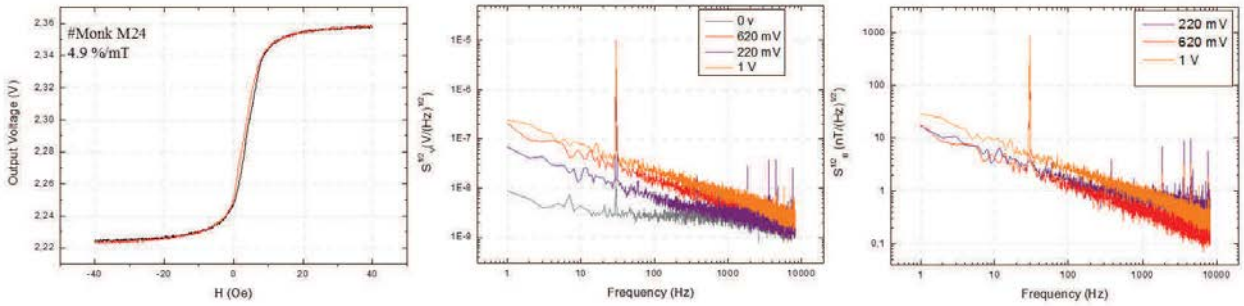

Figure 5.6: Sharp magnetrode characteristics. Left: R(H) response of #M24 Monk probe with a resistance R_0= 440 Ω, a MR ratio of 6 % and a sensitivity near zero field of 4.9 %/mT. One can note the linear response of the GMR. Middle: noise voltage spectrum as function of the frequency. Right: field equivalent noise as function of frequency.

#M19Evans @ 500mV				
	10 Hz	30 Hz	1 kHz	10 kHz (thermal noise)
S_V	29 nV/$\sqrt{Hz}$	16 nV/$\sqrt{Hz}$	3 nV/$\sqrt{Hz}$	1.3 nV/$\sqrt{Hz}$
S_B	7 nT/$\sqrt{Hz}$	4 nT/$\sqrt{Hz}$	800 pT/$\sqrt{Hz}$	240 pT/$\sqrt{Hz}$
#M24Monk @ 1V				
S_V	77 nV/$\sqrt{Hz}$	53 nV/$\sqrt{Hz}$	6 nV/$\sqrt{Hz}$	2 nV/$\sqrt{Hz}$
S_B	9 nT/$\sqrt{Hz}$	6 nT/$\sqrt{Hz}$	1 nT/$\sqrt{Hz}$	500 pT/$\sqrt{Hz}$

Table 5.1: Noise characteristics of two of the sharp probes used for the recordings in their operating bias voltage.

5.2.2 Experimental protocol

The cat was anesthetized with Isoflurane (0.8-0.9 %) mixed with O_2/N_2O (30 %/70 %) and maintained after tracheotomy by artificial respiration. Analgesia was provided by continuous infusion of the opiate Sufentanil (2 µg/kg/h). Depth of anesthesia was continuously monitored by careful inspections of vital signs (heart rate, expiratory CO_2, body temperature) and adjusted if necessary. Cat's head was hold by a stereotaxic chamber (figure 5.7) and two craniotomies were performed according to stereotactic coordinates, given access to areas 17 and 21a. Area 21a was previously injected with an AAV (Adeno Associated Virus) vector system delivering a channelrhodopsin (ChR2), rendering the local neuronal population sensitive to blue light (optogenetic stimulation). The duratomy was done before implanting the magnetrodes and in some case, the pia mater also was removed.

After the surgery, a tungsten electrode (NeuroNexus 32 channels probe; FHC driver) was inserted into area 17, hundreds of microns away from the magnetrode during all the recordings. The tungsten probe is 70 mm long, a shank diameter of 125 µm and an impedance of 1 MΩ at 1 kHz.

First, drifting gratings features were shown on a LCD monitor, 50 cm away from the cat and the stimuli were tailored to match the preference of the recorded areas. However, the magnetrodes have been discovered to be sensitive to the light artefact, leading to a photoelectric effect in the semiconducting silicon, used as a substrate, and which is not entirely electrically isolated from the magnetic sensors. Therefore, visual stimulation has been changed for a blue laser light (its nominal wavelength was 473 nm and was set with a power of 2 mW), directly pointed in the right eye since recordings were done in the left hemisphere (area 17). The laser was covered with aluminum foil to reduce at most the light contamination on the probes.

The stimulation was consisting of a DC pulse to eye with the blue laser. Table 5.2 reports the stimulation parameters used during recordings. The visual stimulus is shown repeatedly, introducing a jitter to avoid adaptation. The numbers of trials used were 1000 to 2000, and the output signals were averaged on the stimulation signal trigger.

	Pre stim	Stim duration	Post stim	Inter-Trial-Interval	jitter(ms)	Trials
AC	200 ms	100 ms/200/500	200 ms	300/500 ms	200/600	1000
DC	200 ms	500 ms	200 ms	500 ms	600	1000

Table 5.2: Stimulation parameters.

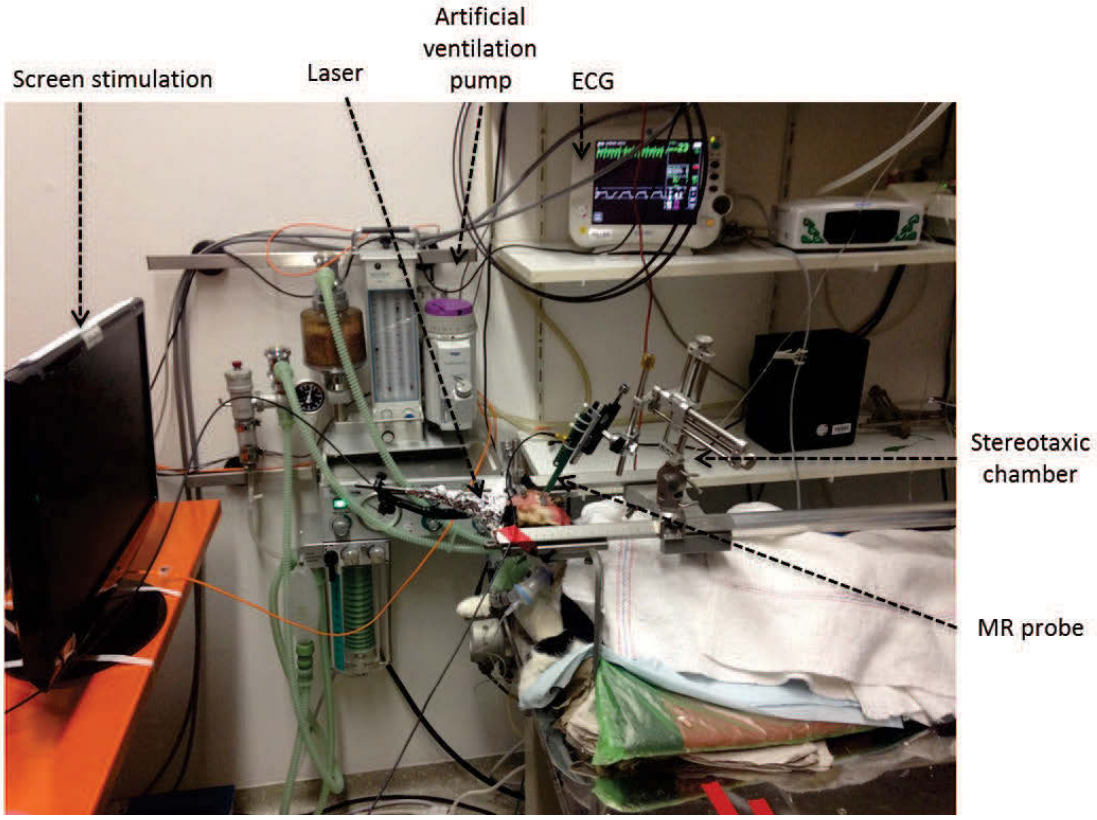

Figure 5.7: Picture of the experiment.

5.3 Results

The results shown here have been obtained during to recordings sessions performed on February 27th and 28th, 2015 and May 1st and 2nd, 2015. Recordings have been performed with both sharp and planar probes in the two electronics mode (AC and DC). During the experiments, heart beat (200 beats/min, 3 Hz) and breathing were detected by planar sensors; this can be explained by cortex movements because of the large craniotomy window. Therefore, planar sensors have not been used for long-time recordings.

Magnetic signals have been detected on two sharp probes *(*#M19Evans, #M24Monk). Both probes contain a single GMR element (meander shape), 4 and 5 µm wide and 30 µm long respectively. On each probe, a Pt electrode (20x20 µm) located 30µm below the sensor were measuring the electric potential. Both AC and DC configuration have been tested and

recorded a magnetic signal (section 5.3.1,5.3.2). Signals recorded from the Pt electrode on sharp magnetrode are strongly correlated with the tungsten electrode (named ESI electrode on figures).

Furthermore, a set of control experiments have been performed to confirm the magnetic and physiologic origin of the recorded signals (section 5.3.3).

5.3.1 AC mode

On AC mode recordings, the GMR was fed with a 700 µA current (V_{in}= 600 mV_{pp}), the carrier frequency was set to 34.111 kHz with V_1= V_2= 2 V_{pp} which are the feeding voltage for phase and out of phase (also called quadrature) demodulation respectively. The frequency bandwidth of the acquisition chain was [0.3 Hz; 10 kHz] or [0.3 Hz; 3 kHz] and was adjusted to record both slow (0.7-300 Hz, LFP) and high (700 Hz-7 kHz, MUA) events. In order to balance the output signal, adjustable capacitances were added in parallel with the output ($\sim$ 2 nF).

The magnetic channels (phase and quadrature, magnetic DC) were amplified by the acquisition chain (the total gain is 384: 192 from the modulation preamplifier, 20 from the Stanford Reasearch amplifier, and 0.1 from the ESI acquisition system) and electric channels (Electrode CEA and Electrode ESI) were not amplified. The recorded signals are expressed in µV and nT as function of time for electric and magnetic output respectively. Finally, the raw data are filtering with a notch-filter to avoid the 50 Hz contamination.

For the 100 ms stimulation and after a set of 2000 acquisitions, a magnetic signal has been measured, correlated in time with recorded ERPs on the tungsten probe (ESI probe on Figure 5.8). The onset is at 800 ms and the response occurs $\sim$30-50 ms after the stimulus (transmission delay between retina and primary visual cortex (V1)) and the offset is 100 ms after the stimulus. One can note that evoked response on ESI electrode, magnetic and quadrature channels are strongly correlated in time, which is a strong indication of its physiological origin.

A second and a third trial with longer stimulation pulse (200 and 500 ms) were performed, the corresponding signals are shown in figure 5.9 for 200 ms duration and figure 5.10 for 500 ms stimulation. As expected, the magnetic signal appears and disappears simultaneously with the control electrode. Besides the temporal dynamic correlation, one can denote that the biphasic nature of the electric signals is also seen on the magnetic phase channel. This shape correlation is reported on all the magnetic AC recordings. This indicates that signals

recorded from magnetrode are the magnetic signature of the electrophysiology signals. One can already note that the obtained signal have an amplitude around 25 nT_{pp}, for 100 ms duration, a signal larger than expected from modeling, which would lead to signals of 1 nT at most. The out of phase signal leads also to a signal about one third smaller than on the phase output.

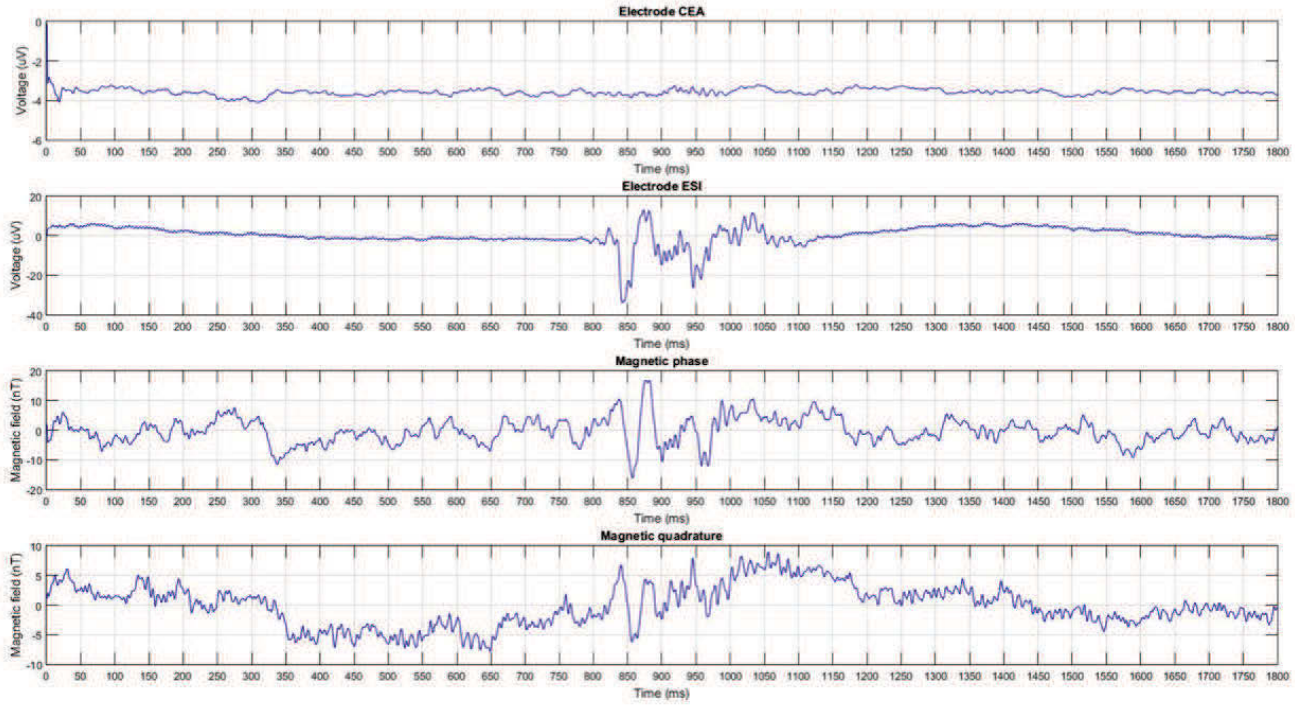

Figure 5.8: AC *in vivo* recordings. Four channels are recorded: ESI electrode (tungsten electrode), CEA electrode (electrode on sharp probe), magnetic in phase and out of phase are the two outputs from AC electronics mode. The onset at 800 ms is the laser stimulation starting; a signal is observed on both ESI electrode and magnetic channels, 30-40ms after the stimulus, which correspond to the transmission delay from the retina to the cortex. The offset is 100 ms later. In this experiment, the signal from the CEA electrode was saturating because of the AC signal driven in the GMR sensors nearby, and the output is note showing any response.

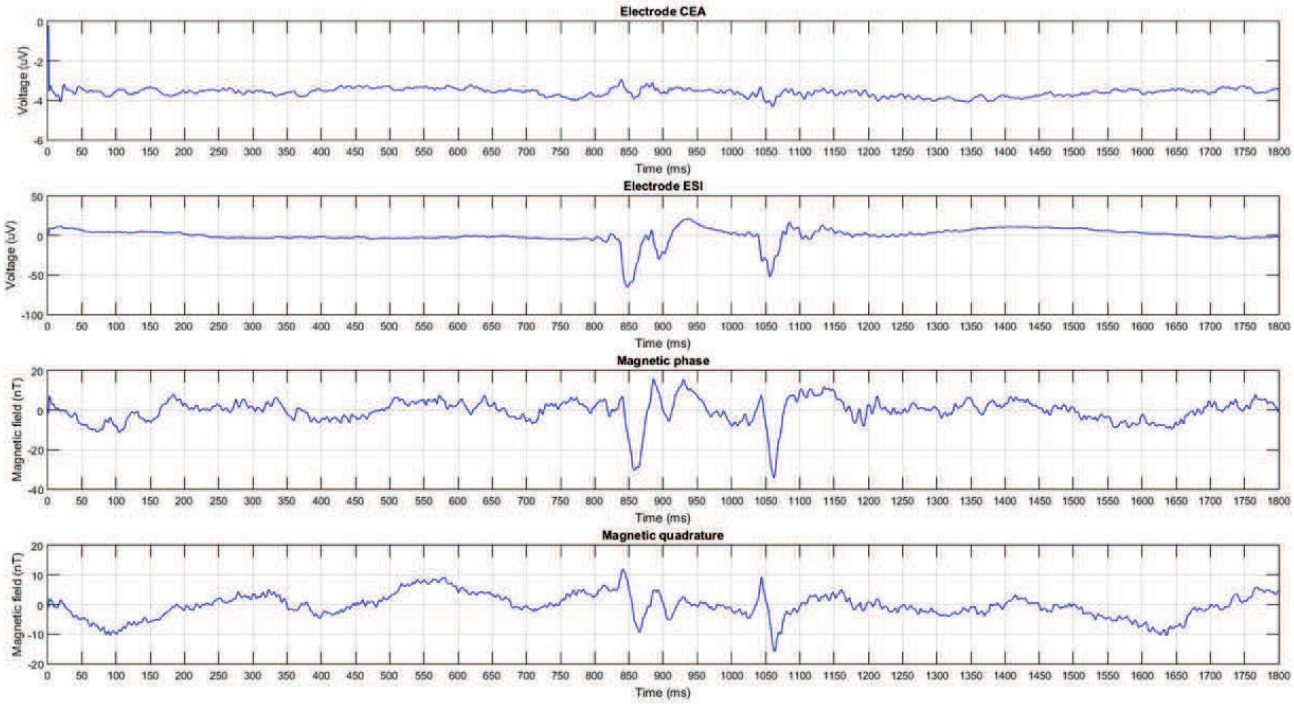

Figure 5.9: Same recordings channels than in Figure 5.8 but with a longer stimulation (offset at 200 ms). Here as well a magnetic signal is recorded on the phase output (30 nT_{pp}) and with much lower amplitude on the quadrature, both very well correlated with the electric ERP recorded on the tungsten electrode.

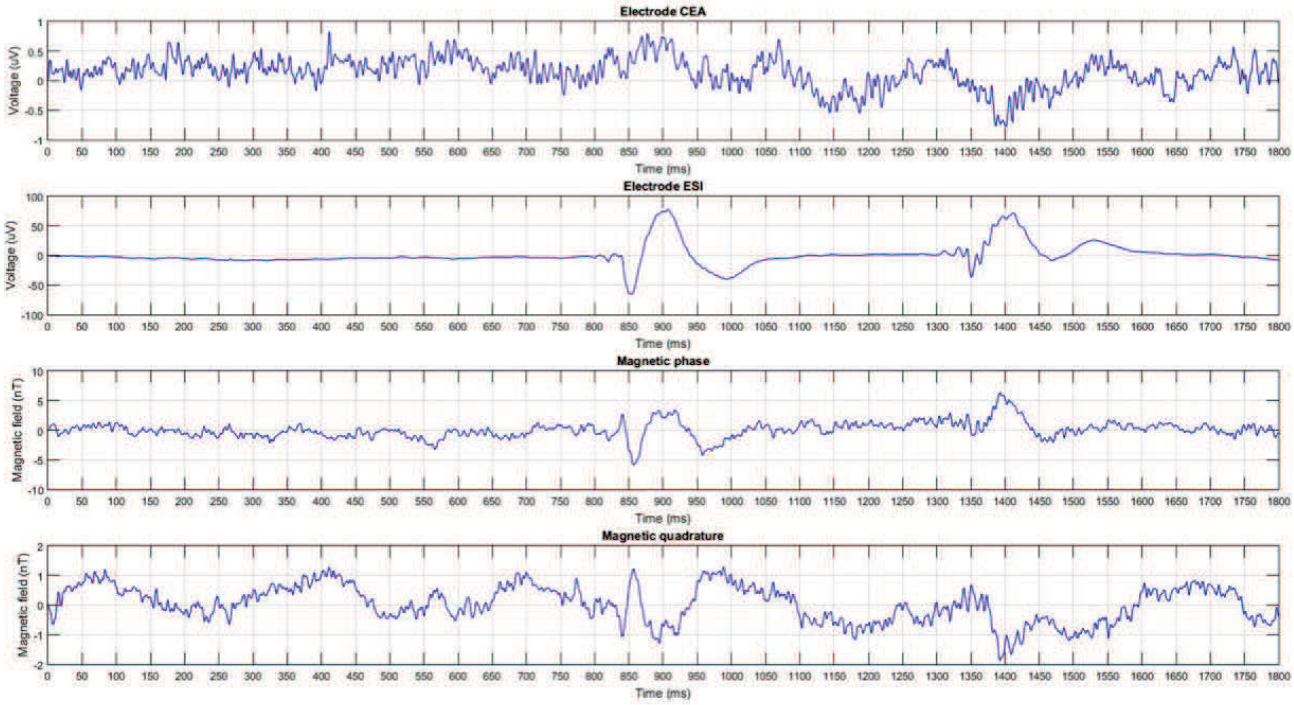

Figure 5.10: Same recordings channels than on Figure 5.8with longer stimulation (500 ms). Note the separation in time between the peaks at the onset (850 ms) and at the offset (1350 ms) because of the longer light exposure. The magnetic phase output is well correlated with the tungsten electrode, and the quadrature exhibits also a small signal (2 nT compared to 10 nT in the phase output).

The results can be treated in frequency-time domain, a common signal processing (Matlab) that studies signals in both frequency and time domains simultaneously (2D viewed unlike amplitude vs time that display signals in 1D). Such technique allows spectrum frequency view after a Fourier Transform. Figure 5.11 highlights the results presented in figure 5.8 with 100 ms stimulation duration. The frequency bandwidth (DC-100 Hz) was chosen according to attempt neuronal activity: indeed, very low frequency components (DC - 25 Hz) include the heart beat and breathing frequency as well as ERPs activity while higher frequency (above 50 Hz) emphasizes information about cortical cerebral rhythms (gamma frequency).

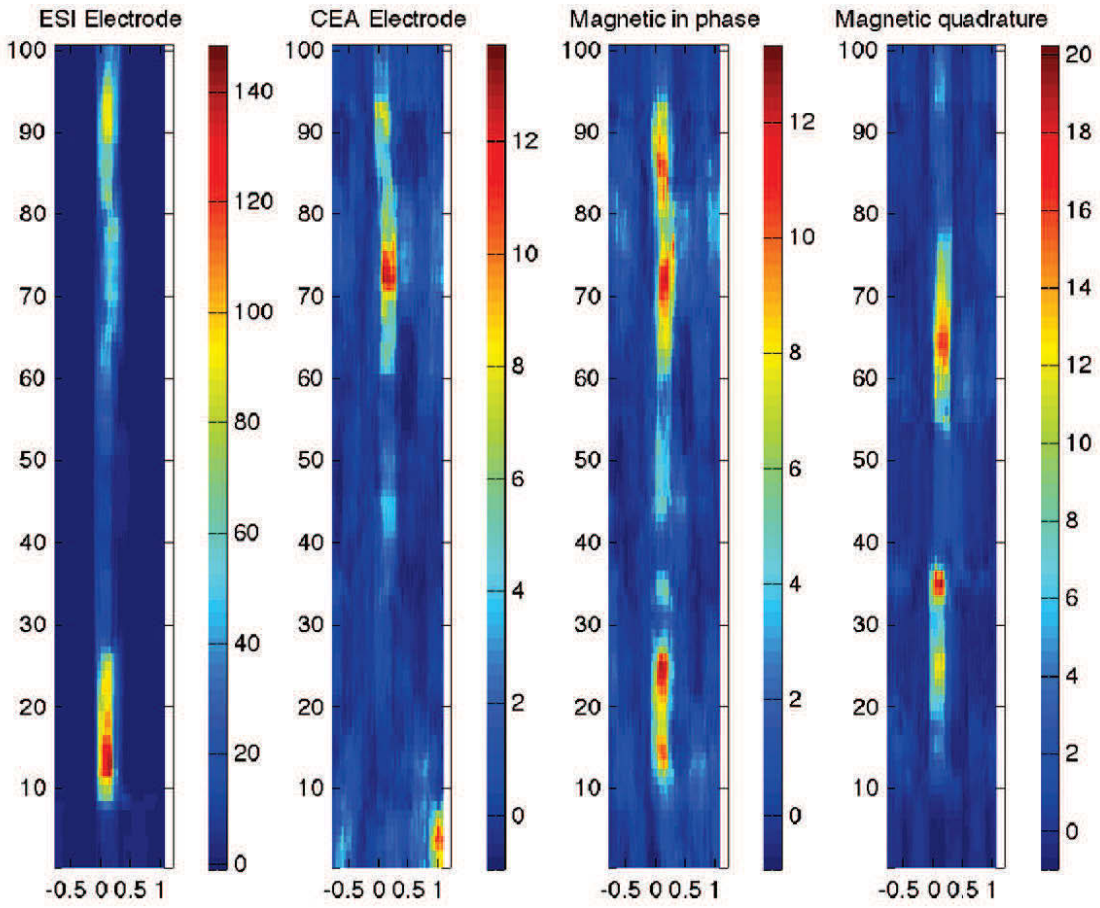

Figure 5.11: Time-frequency analysis for a 100 ms stimulation duration. The onset signal is at 0.

5.3.2 DC mode

As explained in Chapter 3, signals recorded in the DC mode are subject to the strong capacitive coupling arising between the magnetic sensor and the medium. Consequently, the sensors measure both the resistance and capacitive variations. So the AC mode has been used to avoid this capacitive coupling between the sensor and the medium. However, recordings in the DC mode is suitable to observe and quantify this coupling.

Three channels are displayed in the DC mode: Electrode CEA, Electrode ESI and Magnetic DC which is the GMR output while feeding the sensor with a DC current. The total gain of the acquisition chain is 13140 (730 from the preamplifier (INA103), 20 from the Stanford Research amplifier, and 0.9 from the ESI acquisition system).

Figure 5.12 shows the results on #M19Evans sharp sensor after 1000 trials with a stimulation duration of 100 ms. The feeding current is 1 mA. Both electrode CEA and magnetic DC channels were perturbated by 50 Hz contributions. Nevertheless, the evoked response is clearly displayed and corresponds in time to the onset/offset stimulation (800/900 ms respectively).

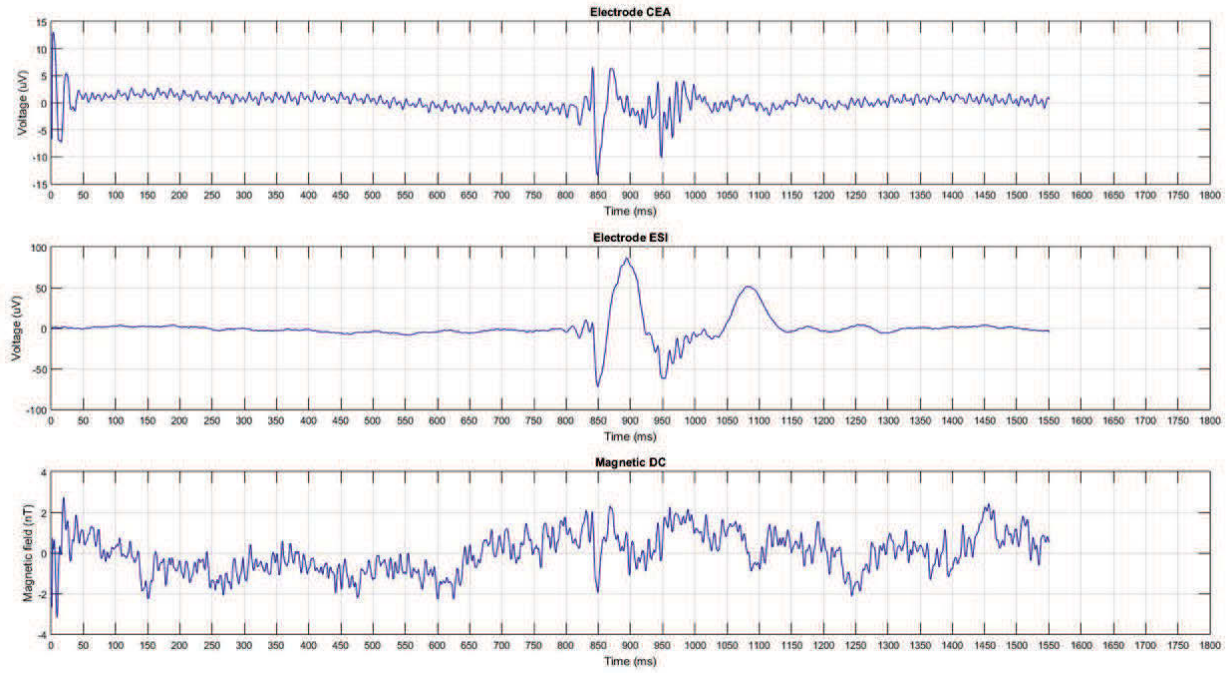

Figure 5.12: DC recordings. The magnetic signal is lower than the one recorded in AC mode.

5.3.3 Control experiments

In order to verify the purely magnetic origin of the measured signal, some control experiments were performed.

5.3.3.1 I=0

First, a straightforward control can be done, by switching-off the bias current in the GMR. As expected, the signal disappeared on magnetic channels with AC mode, meaning that there is no direct electric coupling (Figure 5.13) and confirming the origin nature of the recorded signal while feeding current was switched-on.

While the current is switched of on the GMR sensors, the electrodes, which are passive, still record the electric signal, though the shape of the ESI electrode is unchanged. Interestingly, the electrode embedded on the magnetrode has been saturated by the RF signal at 64 kHz feeding the nearby GMR sensor (which is why its output while the current was on in the AC mode was blinded), but when no current is feeding the GMR, the magnetrode electrode shows an output which is correlated to the ESI electrode.

The same test was performed with the DC mode; the results reveal a small coupling contamination while switching-off the feeding current (figure 5.14).

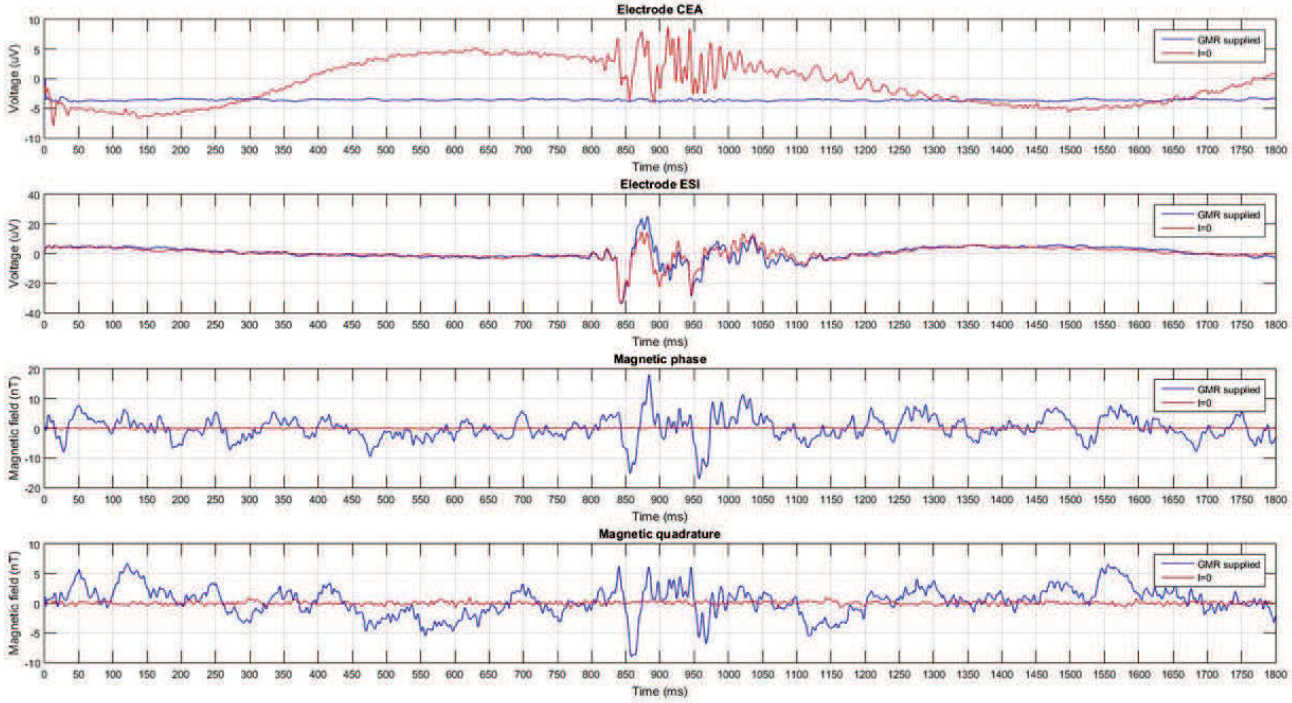

Figure 5.13: AC *in vivo* recordings with #M19Evan*s* sharp probe. Blue lines are the output while the GMR sensor is supplied at 64 kHz; Red lines are recordings when switching-off the bias voltage, as a proof of a purely magnetic origin, magnetic channels are silent while ESI electrode shows the same ERPs. Note that the electrode on the magnetrode is blinded when the RF feeding current is on. At I = 0, it displays an output correlated in time with the ESI electrode, though with differences on some features.

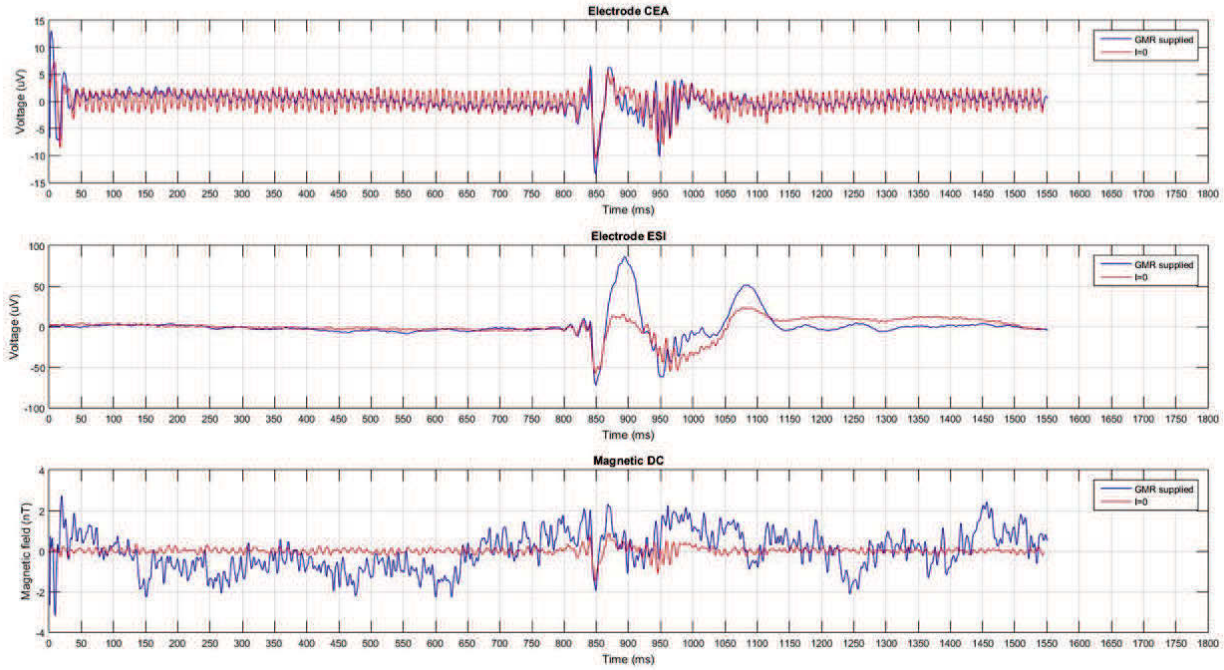

Figure 5.14: DC *in vivo* recordings with #M19Evans sharp probe. The two first channels correspond to the electrical recordings while the third is the DC magnetic output. The blue lines is recordings with feeding current in the GMR (1 mA) and the red lines without feeding current. The amplitude recorded on the magnetic output in DC is lower than on AC mode; furthermore, the noise level is lower than expected, which could be due to some saturation on the electronics, that would also lead to a limitation of the magnetic signal amplitude. Note that while switching-off the current, the signal is reduced on both Electrode ESI and magnetic DC channels.

5.3.3.2 Tangential direction

Following the theory, the probes sensitive to the tangential direction should not exhibit a signal while recording in the gyrus. This has been confirmed with the sharp probe #M19Camilo, a single GMR element (meander shape) tangentially sensitive to the MF used in the AC mode. As expected, the magnetic outputs are silent during visual stimulation on the #M19Camilo probe and electric outputs are blind to the changes.

5.3.3.3 Removing tungsten

A last control experiment was achieved to see whether the tungsten electrode could have an influence on the magnetic sensor, leading to any signal distortion. Two trials were performed,

one with the tungsten probe inserted into the visual cortex and another one after tungsten was removed. Figure 5.15 demonstrates that there is no direct effect linked to the presence of the tungsten probe.

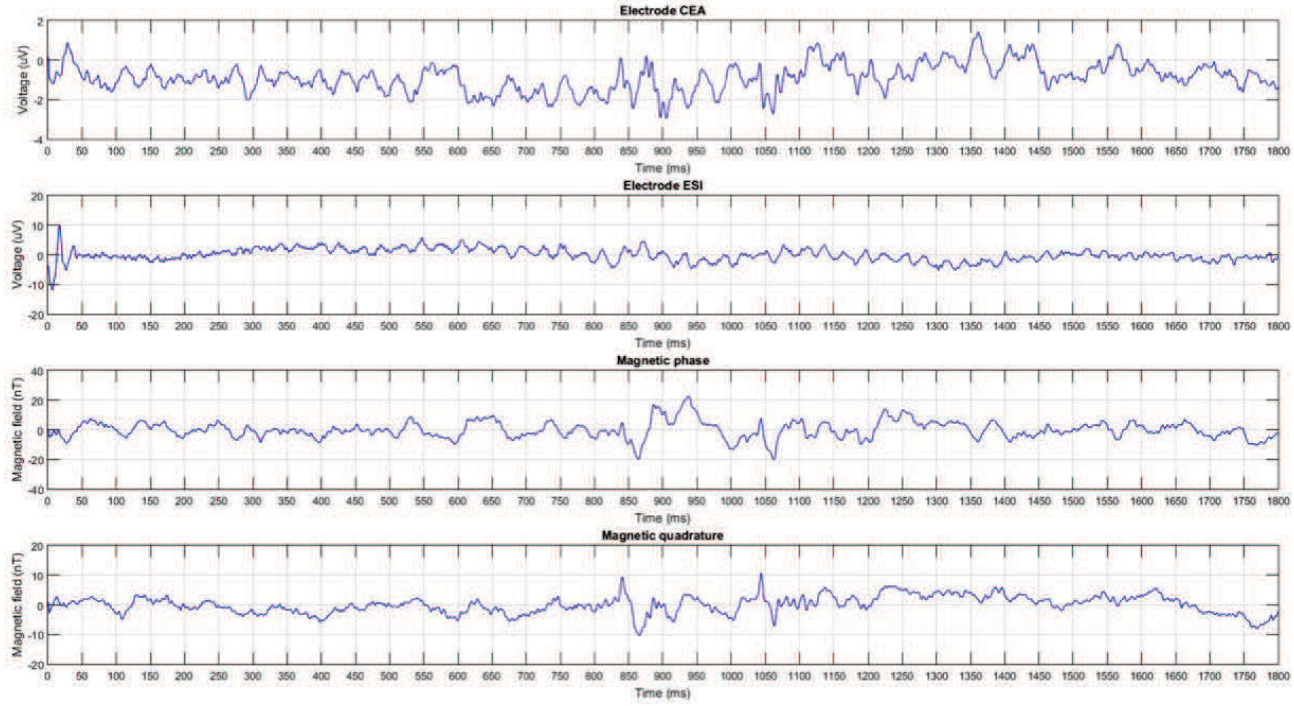

Figure 5.15: Recordings with the tungsten electrode removed from the cortex. The magnetic signals are still present.

5.3.4 Conclusion and perspectives

We obtained the first magnetic recordings of the neuronal activity within the cat's cerebral cortex by means of GMR sensors. Sharp magnetrode with a single GMR element have exhibited a signal that corresponds to the magnetic signature of the stimulus-induced cortical responses while visual stimuli were presented into the eyes.

Both AC and DC electronics mode have been tried. The amplitude of the recorded signal is ∼2-20 nT_{pp}, depending on probe location within cortical layers. The strong temporal dynamics as well as shape correlation between electric and magnetic outputs confirm that those signals are from magnetic origin. Furthermore, control experiments (switching-off the sensor feeding current, removing the tungsten electrode and measuring in the tangential direction) dismiss any artefact or coupling origin of the obtained signals.

An important point is the magnitude of the signals recorded, and the origin of these signals. modeling leads to expected signals about ten times lower than those measured in this work, which remain an open question at this stage of the work. The influence of the return (volume) currents is not yet well understood neither modeled at this scale, and further theoretical investigation could unveil the nature of the magnetic signals recorded.

Additionally, the difference of amplitudes between AC and DC signals is also not understood and will require more measurements to be further analyzed. Several hypothesis are under discussion and in particular a partial screening of DC signals due to the huge 50 Hz signal, typically 50 times larger than the detected signal, an artificial enhancement of the magnetic signal induced by a local strong RF electromagnetic field.

Starting from the obtained data, additional measurements remain to be tested. First, in term of environment, the noise level of the recording chamber was high (in the nT range rms), mainly caused by the 50Hz contamination emitted by the breathing tool. One way to reduce it is by shielding, either with aluminum foil around the sensor or by placing a Faraday cage around the recording table. Shielding would drastically increase the SNR and new recordings could be performed.

Secondly, one can play with the surface and shape of the magnetic sensors, for example by increasing the number of sensors, located either at the tip of the sharp magnetrode and another one near the cortex surface to observe signal propagation, from dendritic tree to soma regions. This would benefit for study the temporal dynamic of neuronal events.

Finally, different types of stimuli could be used; more complex visual stimuli, like gratings could be applied.

Conclusion

The main goal of this thesis work was to investigate the local neuronal currents through magnetic detection. As described in Chapter 1, the electromagnetic activity within neuronal tissues is generated by ions moving across transmembrane channels, exhibiting characteristic amplitudes, durations and shapes.

The first step was to design, fabricate and test magnetic probes meeting these required conditions. Two types of probes have been realized; both are GMR-based sensors.

Firstly we have designed and fabricated planar sensors which exhibit a sensitivity in the range of 10 to 20 %/mT, a MR ratio of 6 % and a detectivity (field equivalent noise) of 1 nT/$\sqrt{Hz}$ at low frequencies, thanks to their rather large GMR volume (typically 1 mm^2). Planar magnetrode were dedicated to magnetic field surface measurements.

Secondly, we developed magnetically inserted probes, designed as a needle-shape and dedicated to record neural activity within the living tissues. Specific microfabrication process for sharp magnetrodes have been achieved. Sharp probes contain one or two sensing elements deposited on very thin silicon substrate (100 to 200 µm) to limit the damages tissues.

Furthermore, several designs have been investigated, trying to enhance the sensor performances. The first set of sharp magnetrodes, composed by one or two small sensors designed as a yoke shape (3x25 µm) has revealed a sensitivity of 1-2 %/mT with a field equivalent noise in the range of 20 nT/$\sqrt{Hz}$ at low frequencies. By playing with the shape and the size of the sensors (meander shape, 4x30 µm), a second set of sharp probes displayed important improvements in terms of sensitivity and field equivalent noise. Additionally, all probes passivation has been successfully tested in a conductive medium that guarantee the stability later on during the experiment.

One of the main constraints throughout this work was to deal with the strong direct coupling between the GMR sensors and the living tissues which could mask the physiological signals. Thus, a dedicated electronics scheme, based on frequency modulation has been developed, enabling the separation between the electric and magnetic components of the

recording signals (chapter 3). This electronics have been tested and validated on both *in vitro* and *in vivo* experiments.

Testing the magnetrode technology on neuronal circuitry with its normal anatomical organization was one of the main goals of this project. Hence, three models have been investigated, trying to get a neuromagnetic response. The two first ones are realized *in vitro* while the third one is *in vivo*.

First magnetic recordings have been performed on the neuro-muscular junction of a mouse muscle (soleus). Planar segment probes have recorded the first magnetic AP at local scale, providing a direct information on the axial currents within the fibers; both DC and AC schemes gave an amplitude of the measured signal in the range of few nT_{pp} with a biphasic nature which matches with the data from electrophysiology and with the modeling. A set of control experiments have been performed by playing with the geometry and some pharmacology to ensure the magnetic origin of the recorded signals and dismiss an artefact or a coupling origin.

Further improvements can be achieved in terms of probes and experiments. A new set of probes are designed and processed with multiple separated segments to allow simultaneous magnetic recordings at various positions of the muscle. A multiple channels electronics readout is now being developed.

The second analyzed *in vitro* model was the hippocampal mouse brain slices. Both planar and sharp probes have been tested showing some preliminary results. However, the amplitude of the recorded signals (few hundreds of nT) leads to a direct coupling issue. Moreover, the actual rms noise level in the interface chamber is higher than the intrinsic sensor noise. In order to reduce this contamination, a new shielded structure, made with two layer shield (mu metals and copper) has been built to be placed around the present recording chamber.

The last experiment perform in this thesis work has been realized on anesthetized cat's cerebral cortex at ESI in Pascal Fries's lab (*in vivo* measurements). The results manifest the first local magnetic recordings of the neuronal activity within the cat's visual cortex. While visual stimuli were presented into the eyes, a sharp magnetrode with a single GMR element has recorded the magnetic features of stimulus-induced cortical responses. Depending on probe location within cortical layers, the amplitude of the measured signal is $\sim$ 10-20 nT_{pp}; the strong correlation in terms of shape and temporal dynamic between electric and magnetic channels demonstrates the magnetic origin of the measured signals.

Additionally, several control experiments (switching-off the sensor feeding current, measuring in the tangential direction and removing the tungsten control probe) have excluded

any artefact or coupling origin of the obtained signals.

An important point is the magnitude of the signals recorded, and the origin of these signals. Modeling leads to expected signals about ten times lower than those measured in this work, which remains an open question at this stage of the work. The influence of the return (volume) currents is not yet well understood neither modeled at this scale, and further theoretical investigation could unveil the nature of the magnetic signals recorded.

As previously described, further improvements can be achieved on both magnetic sensors and measurement setup for the future recordings.

Electrophysiology techniques carry crucial information about the electrical activity within neuronal matter, from local microcircuits to large-scale brain-wide networks thanks to the development of multiple techniques. However, probing locally the magnetic signature of this activity gives direct information about neuronal currents and further, the vectorial nature of magnetic measurement guarantee information about the directionality of neuronal ionic flux without disturbing it. Additionally, a reference free measurement such as magnetic sensing is a condition required for brain network analysis by correlation.

Measuring locally the magnetic signature of the neuronal activity will also shed light on the MEG measurements analysis, and helps reaching an accurate description of the signal sources, which is necessary for the *inverse problem* resolution.

At last, by contrast to implantable electrodes that eventually fail due to the adverse effect of the host tissues response to the indwelling implant, magnetically inserted probes are not affected by this drawback. Indeed, a magnetic signal is crossing the tissues freely and is immune to the interface evolution. Thus, neural engineering applications such as implantable neural prosthesis used for chronic recordings are conceivable.

Bibliography

[1] E.J Tarte, P.E Magnelind, A.Ya Tzalenchuk, A Lõhmus, D.A Ansell, M.G Blamire, Z.G Ivanov, and R.E Dyball. High tc squid systems for magnetophysiology. *Physica C: Superconductivity*, 368(1–4):50 – 54, 2002.

[2] Ranjith S Wijesinghe. Magnetic measurements of peripheral nerve function using a neuromagnetic current probe. *Experimental Biology and Medicine*, 235(2):159–169, Feb 2010.

[3] Eric R. Kandel; James H. Schwartz; Thomas M. Jessel. *Principles of Neural Science, Fourth Edition*. Elsevier, 2000.

[4] Nelson Spruston. Pyramidal neurons: dendritic structure and synaptic integration. *Nature Reviews Neuroscience*, 9(3):206–221, March 2008.

[5] Eugene M. Izhikevitch. *Dynamical Systems in Neuroscience; The Geometry of Excitability and Bursting*. MIT Press, 2007.

[6] Claude Bédard, Helmut Kröger, and Alain Destexhe. Modeling extracellular field potentials and the frequency-filtering properties of extracellular space. *Biophysical Journal*, 86(3):1829–1842, March 2004.

[7] A. Destexhe and C. Bedard. Local field potential. *scholarpedia*, 8(8):10713, 2013.

[8] Andreas K. Engel, Christian K. E. Moll, Itzhak Fried, and George A. Ojemann. Invasive recordings from the human brain: clinical insights and beyond. *Nature Reviews Neuroscience*, 6(1):35–47, Jan 2005.

[9] CM Lewis, CA Bosman, and P Fries. Recording of brain activity across spatial scales. *Current Opinion in Neurobiology*, 32(0):68–77, June 2015.

[10] György Buzsáki, Costas A. Anastassiou, and Christof Koch. The origin of extracellular fields and currents - eeg, ecog, lfp and spikes. *Nature Reviews Neuroscience*, 13(6):407–420, June 2012.

[11] Adrien Peyrache, Nima Dehghani, Emad N. Eskandar, Joseph R. Madsen, William S. Anderson, Jacob A. Donoghue, Leigh R. Hochberg, Eric Halgren, Sydney S. Cash, and Alain Destexhe. Spatiotemporal dynamics of neocortical excitation and inhibition during human sleep. *Proceedings of the National Academy of Sciences*, 109(5):1731–1736, 2012.

[12] Galvani Luigi; Volta Alessandro. *De viribus electritatis in motu musculari commentarius*. Dibner Library. Heradl of science, 1791.

[13] Donald B. MacHattie. *Investigation of the Evoked Magnetic Action Flux of Skeletal Muscle*. PhD thesis, McMaster University, 1987.

[14] Gyorgy Buzsaki. Large-scale recording of neuronal ensembles. *Nature Neuroscience*, 7(5):446–451, May 2004.

[15] Piotr Olejniczak. Neurophysiologic basis of eeg. *Journal of Clinical Neurophysiology*, 23(3), 2006.

[16] Ernst Niedermeyer and Fernando H Lopes da Silva. *Electroencephalography: basic principles, clinical applications, and related fields*. Wolters Kluwer Health, 2005.

[17] G. Pfurtscheller and F. H. Lopes da Silva. Event-related eeg/meg synchronization and desynchronization: basic principles. *Clinical Neurophysiology*, 110(11):1842–1857, Nov 1999.

[18] N E Crone, D L Miglioretti, B Gordon, and R P and Lesser. Functional mapping of human sensorimotor cortex with electrocorticographic spectral analysis. ii. event-related synchronization in the gamma band. *Brain*, 121(12):2301–2315, Dec 1998.

[19] Thilo Womelsdorf, Jan-Mathijs Schoffelen, Robert Oostenveld, Wolf Singer, Robert Desimone, Andreas K. Engel, and Pascal Fries. Modulation of neuronal interactions through neuronal synchronization. *Science*, 316(5831):1609–1612, June 2007.

[20] Birthe Rubehn, Conrado Bosman, Robert Oostenveld, Pascal Fries, and Thomas Stieglitz. A mems-based flexible multichannel ecog-electrode array. *Journal of Neural Engineering*, 6(3):036003, 2009.

[21] Thilo Womelsdorf, Pascal Fries, Partha P. Mitra, and Robert Desimone. Gamma-band synchronization in visual cortex predicts speed of change detection. *Nature*, 439(7077):733–736, Feb 2006.

[22] Micha E. Spira and Aviad Hai. Multi-electrode array technologies for neuroscience and cardiology. *Nature Nanotechnology*, 8(2):83–94, Feb 2013.

[23] Utah array - http://www.blackrockmicro.com.

[24] Massimo Scanziani and Michael Hausser. Electrophysiology in the age of light. *Nature*, 461(7266):930–939, Oct 2009.

[25] Erwin Neher and Bert Sakmann. Single-channel currents recorded from membrane of denervated frog muscle fibers. *Nature*, 1976.

[26] Patch-clamp - http:/www.ipmc.cnrs.fr.

[27] Francisco Varela, Jean-Philippe Lachaux, Eugenio Rodriguez, and Jacques Martinerie. The brainweb: Phase synchronization and large-scale integration. *Nature Reviews Neuroscience*, 2(4):229–239, Apr 2001.

[28] Matti Hämäläinen, Riitta Hari, Risto J. Ilmoniemi, Jukka Knuutila, and Olli V. Lounasmaa. Magnetoencephalography theory, instrumentation, and applications to noninvasive studies of the working human brain. *Reviews of Modern Physics*, 65(2):413–497, Apr 1993.

[29] Makoto Fukushima, Okito Yamashita, Thomas R. Knösche, and Masa-aki Sato. Meg source reconstruction based on identification of directed source interactions on whole-brain anatomical networks. *NeuroImage*, 105(0):408–427, Jan 2015.

[30] Emma L. Hall, Siân E. Robson, Peter G. Morris, and Matthew J. Brookes. The relationship between meg and fmri. *NeuroImage*, 102, Part 1(0):80–91, 11 2014.

[31] Orang Alem, Alex M. Benison, Daniel S. Barth, John Kitching, and Svenja Knappe. Magnetoencephalography of epilepsy with a microfabricated atomic magnetrode. *The Journal of Neuroscience*, 34(43):14324–14327, Oct 2014.

[32] Yoshio C. Okada, Jie Wu, and Shinichi Kyuhou. Genesis of meg signals in a mammalian cns structure. *Electroencephalography and Clinical Neurophysiology*, 103(4):474 – 485, 1997.

[33] P. Magnelind. *High-Tc SQUIDs for magnetophysiology - development of a magnetometer system and measurements of evoked fields from hippocampal neurons in-vitro.* PhD thesis, Chalmers University of Technology, Göteborg, Sweden, 2006.

[34] B J Roth and J P Wikswo. The magnetic field of a single axon. a comparison of theory and experiment. *Biophysical Journal*, 48(1):93–109, Jul 1985.

[35] J. P. Jr. Wikswo and J. M. van Egeraat. Cellular magnetic fields: Fundamental and applied measurements on nerve axons, peripheral nerve bundles, and skeletal muscle., 1991.

[36] José Amaral, João Gaspar, Vitor Pinto, Tiago Costa, Nuno Sousa, Susana Cardoso, and Paulo Freitas. Measuring brain activity with magnetoresistive sensors integrated in micromachined probe needles. *Applied Physics A*, 111(2):407–412, May 2013.

[37] J. Amaral, S. Cardoso, P. P. Freitas, and A. M. Sebastião. Toward a system to measure action potential on mice brain slices with local magnetoresistive probes. *Journal of Applied Physics*, 109(7):07B308, 2011.

[38] J M van Egeraat and J P Wikswo. A model for axonal propagation incorporating both radial and axial ionic transport. *Biophysical Journal*, 64(4):1287–1298, Apr 1993.

[39] K.R. Swinney and J.P. Wikswo Jr. A calculation of the magnetic field of a nerve action potential. *Biophysical Journal*, 32(2):719 – 731, 1980.

[40] James K. Woosley, Bradley J. Roth, and John P. Wikswo Jr. The magnetic field of a single axon: A volume conductor model. *Mathematical Biosciences*, 76(1):1–36, Sep 1985.

[41] Shingo Murakami and Yoshio Okada. Contributions of principal neocortical neurons to magnetoencephalography and electroencephalography signals. *The Journal of Physiology*, 575(3):925–936, 2006.

[42] Shingo Murakami, Tongsheng Zhang, Akira Hirose, and Yoshio C. Okada. Physiological origins of evoked magnetic fields and extracellular field potentials produced by guinea-pig ca3 hippocampal slices. *The Journal of Physiology*, 544(1):237–251, 2002.

[43] K. B. Blagoev, B. Mihaila, B. J. Travis, L. B. Alexandrov, A. R. Bishop, D. Ranken, S. Posse, C. Gasparovic, A. Mayer, C. J. Aine, I. Ulbert, M. Morita, W. Müller, J. Con-

nor, and E. Halgren. Modelling the magnetic signature of neuronal tissue. *NeuroImage*, 37(1):137–148, Aug 2007.

[44] N. Spruston and D. Johnston. Perforated patch-clamp analysis of the passive membrane properties of three classes of hippocampal neurons. *Journal of Neurophysiology*, 67(3):508–529, March 1992.

[45] B. D. Josephson. Possible new effects in superconductive tunnelling. *Physics Letters*, 1(7):251–253, Jul 1962.

[46] Alex I. Braginski John Clarke. *The SQUID Handbook: Fundamentals and Technology of SQUIDs and SQUID Systems, Volume 1*. Wiley-VCH, 2005.

[47] M. Pannetier-Lecoeur and C. Fermon. Magnetic sensors - unpublished. 2015.

[48] Cohen David. Measurements of the magnetic fields produced by the human heart, brain and lungs. *Magnetics, IEEE Transactions on*, 11(2):694–700, Mar 1975.

[49] I. K. Kominis, T. W. Kornack, J. C. Allred, and M. V. Romalis. A subfemtotesla multichannel atomic magnetometer. *Nature*, 422(6932):596–599, Apr 2003.

[50] H. Xia, A. Ben-Amar Baranga, D. Hoffman, and M. V. Romalis. Magnetoencephalography with an atomic magnetometer. *Applied Physics Letters*, 89(21):211104, 2006.

[51] T. H. Sander, J. Preusser, R. Mhaskar, J. Kitching, L. Trahms, and S. Knappe. Magnetoencephalography with a chip-scale atomic magnetometer. *Biomedical Optics Express*, 3(5):981–990, May 2012.

[52] Robert Wyllie, Matthew Kauer, Ronald T. Wakai, and Thad G. Walker. Optical magnetometer array for fetal magnetocardiography. *Optics Letters*, 37(12):2247–2249, 2012.

[53] W. Clark Griffith, Svenja Knappe, and John Kitching. Femtotesla atomic magnetometry in a microfabricated vapor cell. *Biomedical Optics Express*, 18(26):27167–27172, 2010.

[54] Peter D. D. Schwindt, Svenja Knappe, Vishal Shah, Leo Hollberg, John Kitching, Li-Anne Liew, and John Moreland. Chip-scale atomic magnetometer. *Applied Physics Letters*, 85(26):6409–6411, 2004.

[55] W. Thomson. On the electro-dynamic qualities of metals: Effects of magnetization on the electric conductivity of nickel and of iron. *Proceedings of the Royal Society of London*, 8:546–550, 1856.

[56] M. N. Baibich, J. M. Broto, A. Fert, F. Nguyen Van Dau, F. Petroff, P. Etienne, G. Creuzet, A. Friederich, and J. Chazelas. Giant magnetoresistance of (001)fe/(001)cr magnetic superlattices. *Physical Review Letters*, 61(21):2472–2475, Nov 1988.

[57] Claude Chappert, Albert Fert, and Frederic Nguyen Van Dau. The emergence of spin electronics in data storage. *Nature Materials*, 6(11):813–823, Nov 2007.

[58] M. Julliere. Tunneling between ferromagnetic films. *Physics Letters A*, 54(3):225–226, Sep 1975.

[59] B. Dieny, V. S. Speriosu, S. S. P. Parkin, B. A. Gurney, D. R. Wilhoit, and D. Mauri. Giant magnetoresistive in soft ferromagnetic multilayers. *Physical Review B*, 43(1):1297–1300, Jan 1991.

[60] M. Pannetier-Lecoeur, C. Fermon, A. de Vismes, E. Kerr, and L. Vieux-Rochaz. Low noise magnetoresistive sensors for current measurement and compasses. *Journal of Magnetism and Magnetic Materials*, 316(2):e246–e248, Sep 2007.

[61] Reig Candid; Susana Cardoso de Freitas; Subhas Chandra Mukhopadhyay; C.Fermon; M.Pannetier-Lecoeur. *Giant Magnetoresistance (GMR) Sensors. From basis to State-of-the-Art Applications*. Springer-Verlag, 2013.

[62] C. Tiusan, T. Dimopoulos, K. Ounadjela, M. Hehn, H. A. M. van den Berg, V. da Costa, and Y. Henry. Correlation between micromagnetism and tunnel magnetoresistance in magnetic tunnel junctions using artificial ferrimagnets. *Physical Review B*, 61:580–593, Jan 2000.

[63] C. Fermon, M. Pannetier-Lecoeur, N. Biziere, and B. Cousin. Optimised gmr sensors for low and high frequencies applications. *Sensors and Actuators A: Physical*, 129(1–2):203–206, May 2006.

[64] Quentin Herreros. *Very low field magnetic resonance imaging*. PhD thesis, Ecole doctorale interdisciplinaire Européenne Frontières du Vivant (Paris), 2013.

[65] Nathan A. Stutzke, Stephen E. Russek, David P. Pappas, and Mark Tondra. Low-frequency noise measurements on commercial magnetoresistive magnetic field sensors. *Journal of Applied Physics*, 97(10):10Q107, 2005.

[66] H. Nyquist. Thermal agitation of electric charge in conductors. *Physical Review*, 32:110, 1928.

[67] F. N. Hooge and A. M. H. Hoppenbrouwers. 1/f noise in continuous thin gold films. *Physica*, 45(3):386–392, Dec 1969.

[68] R. Guerrero, M. Pannetier-Lecoeur, C. Fermon, S. Cardoso, R. Ferreira, and P. P. Freitas. Low frequency noise in arrays of magnetic tunnel junctions connected in series and parallel. *Journal of Applied Physics*, 105(11):113922, 2009.

[69] L. Yuan, J.X. Shen, and Bharat B. Pant. Locating magnetic noise sources in tmr and gmr recording heads using scanning probe microscopy. *Magnetics, IEEE Transactions on*, 40(4):2233–2235, 2004.

[70] Daryl R. Kipke, William Shain, György Buzsáki, E. Fetz, Jaimie M. Henderson, Jamille F. Hetke, and Gerwin Schalk. Advanced neurotechnologies for chronic neural interfaces: New horizons and clinical opportunities. *The Journal of Neuroscience*, 28(46):11830–11838, 2008.

[71] B Rubehn; C Lewis; P Fries; T Stieglitz. Flexible shaft electrodes for transdural implantation and chronic recording. *Proceedings of the 15th Annual Conference of the International Functional Electrical Stimulation Society*, 2010.

[72] S. Herwik, O. Paul, and P. Ruther. Ultrathin silicon chips of arbitrary shape by etching before grinding. *Microelectromechanical Systems, Journal of*, 20(4):791–793, Aug 2011.

[73] K. Seidl, B. Lemke, H. Ramirez, S. Herwik, P. Ruther, and O. Paul. Cmos-based high-density silicon microprobe for stress mapping in intracortical applications. *Micro Electro Mechanical Systems (MEMS), 2010 IEEE 23rd International Conference on*, pages 35–38, 24-28 Jan. 2010.

[74] Franz Laermer and Andrea Schilp. Method of anisotropically etching silicon. Technical report, March 1996.

[75] C Gabriel, S Gabriel, and E Corthout. The dielectric properties of biological tissues: I. literature survey. *Physics in Medicine and Biology*, 41(11):2231, 1996.

[76] http://www.vetmed.vt.edu/education/curriculum/vm8054/labs/lab10/lab10.htm.

[77] Darrell A. Henze, Zsolt Borhegyi, Jozsef Csicsvari, Akira Mamiya, Kenneth D. Harris, and György Buzsáki. Intracellular features predicted by extracellular recordings in the hippocampus in vivo. *Journal of Neurophysiology*, 84(1):390–400, Jul 2000.

[78]

[79] P. Magnelind, D. Winkler, E. Tarte, and E. Hanse. Hts squid measurements of evoked magnetic fields from transverse hippocampal slices. *International Congress Series*, 1300(0):578–581, June 2007.

[80] F. Barbieri. Modeling magnetic field on hippocampus slice. unpublished.

[81] I. Vida; V. Cutsuridis; B. Graham; S. Cobb; I. Vida. *Hippocampal Microcircuits*. Number 2. Springer, 2010.

[82] Alan Peters Bertram Payne. *The Cat Primary Visual Cortex*. Academic Press, Boston University School of Medicine, 2001.

In vivo sharp probes (model 3)

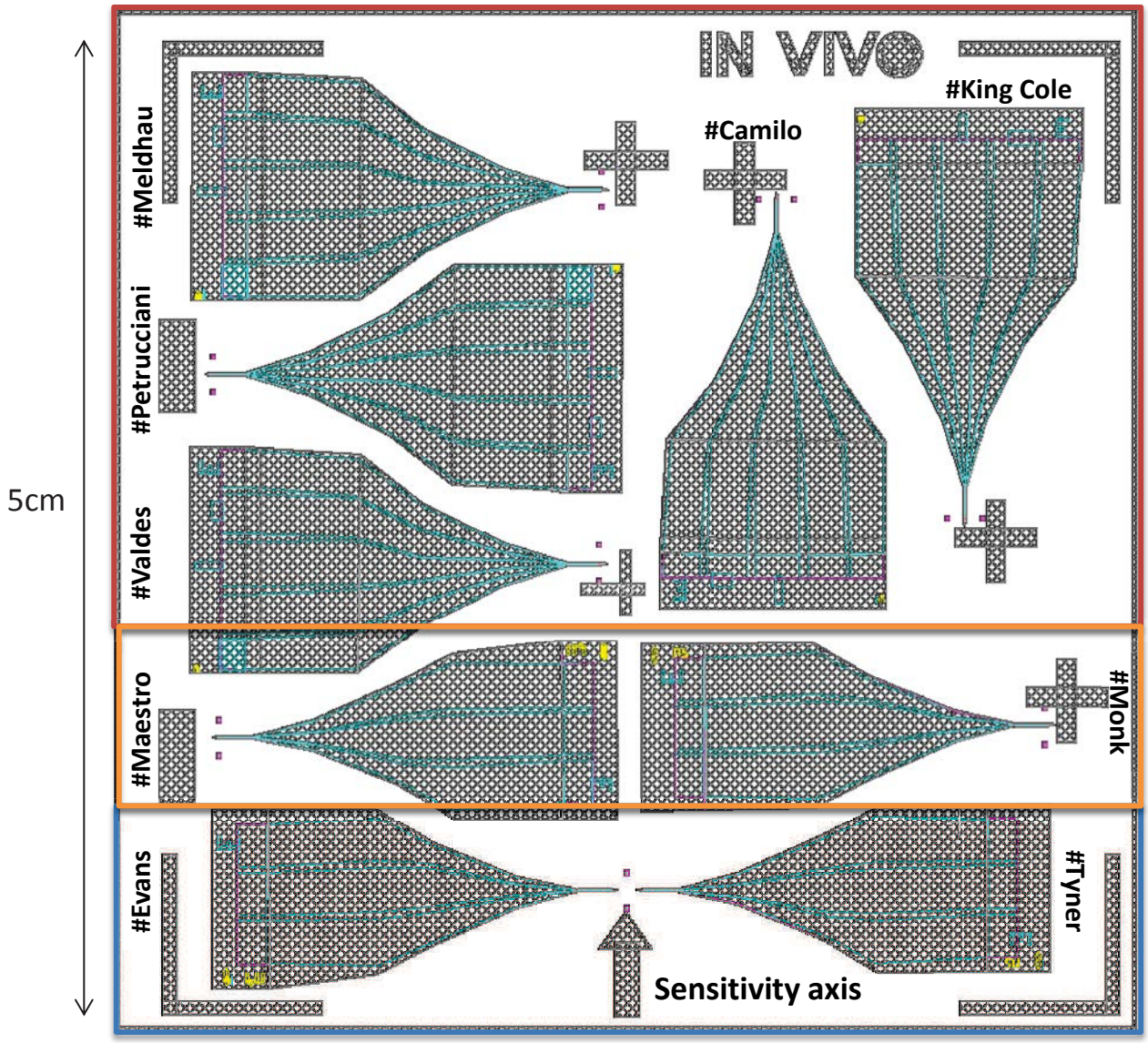

Single meander 30x5 µm + electrode

Single meander 30x4 µm + electrode

Two meanders 30x4 µm + electrode

In vitro (slice) sharp probes (model 3)

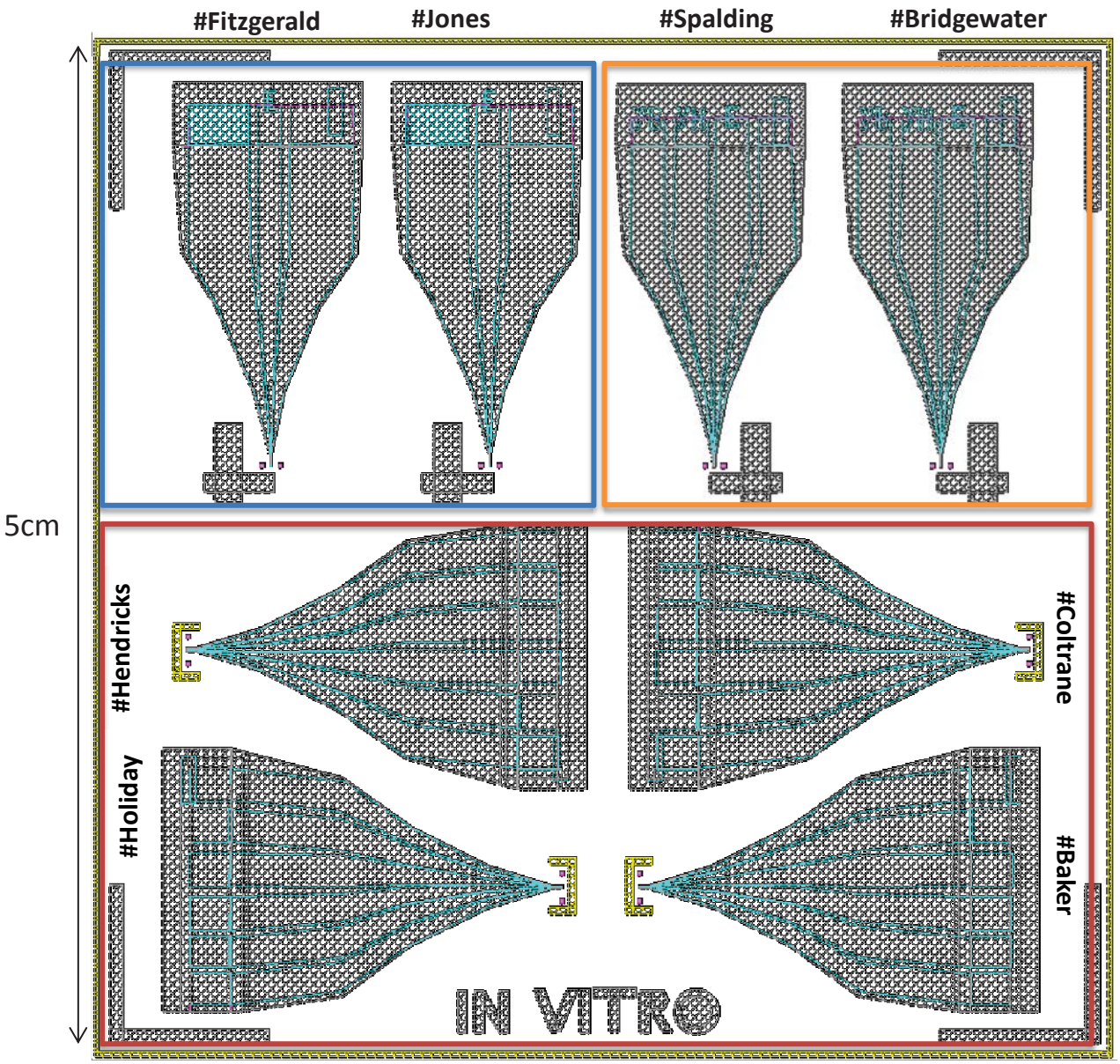

Single meander 25x4 µm + electrode

Two yokes 30x3 µm + electrode

Single meander (10 segments) 26x4 µm

Sharp probes (model 2)

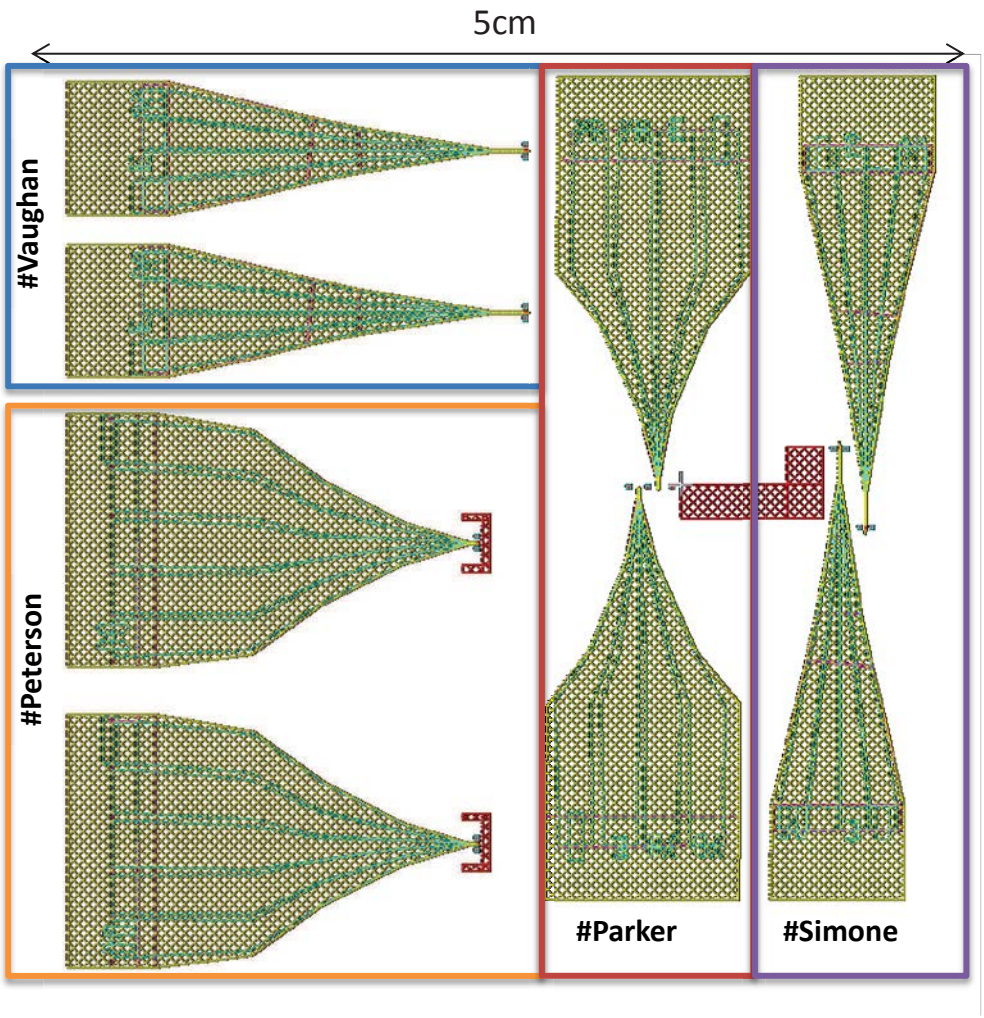

Two meanders 30x6 µm + electrode (***In vivo***)

Single meander (8 segments) 38x6 µm (***In vitro***)

Two yokes 40x5 µm + electrode (***In vitro***)

Two meanders 38x6 µm + electrode (***In vivo***)

In vivo & *in vitro* sharp probes (model 1)

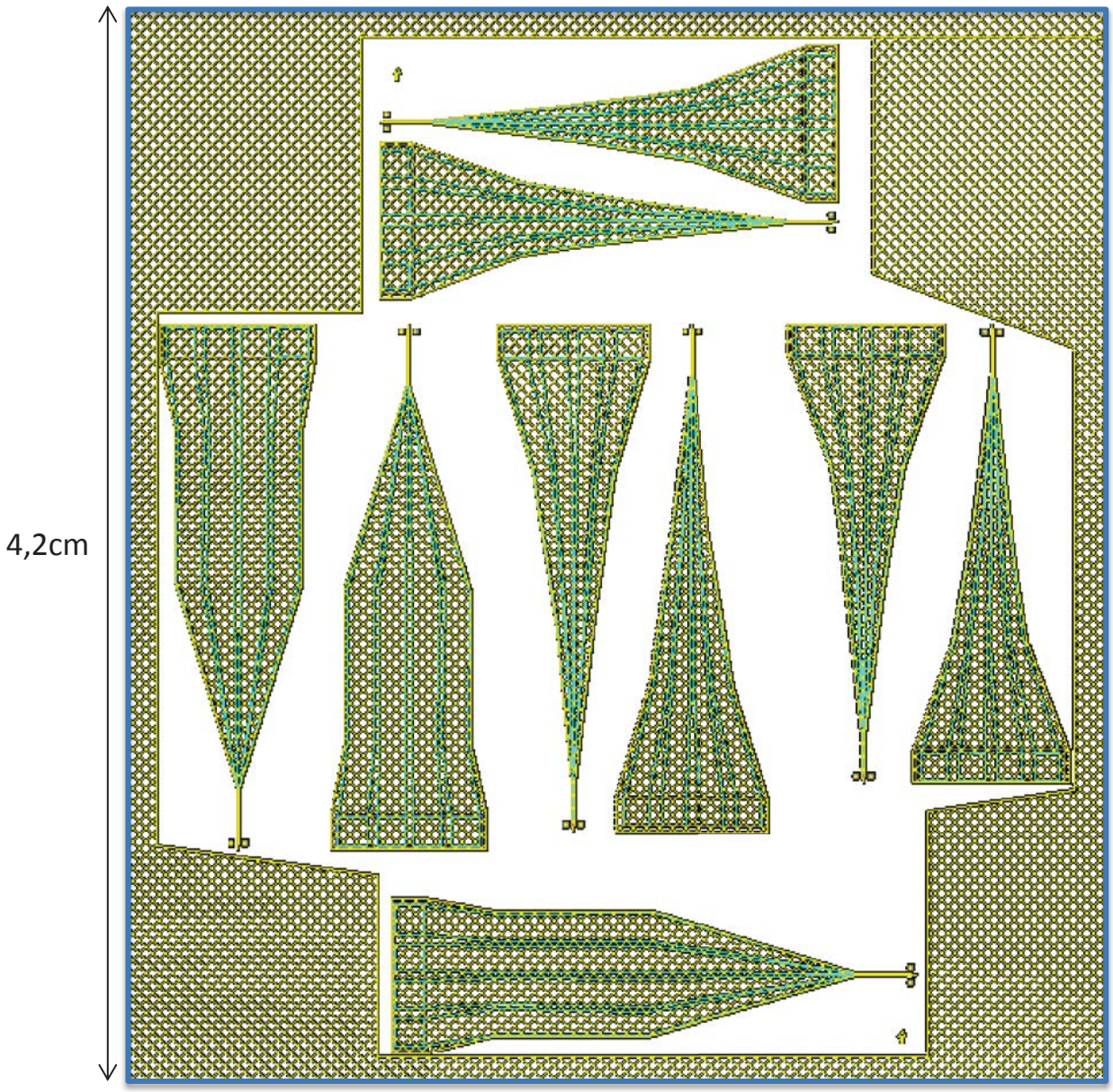

Two yokes 30x3 µm + electrode (***In vivo & in vitro***)

Planar probe – meander (muscle)

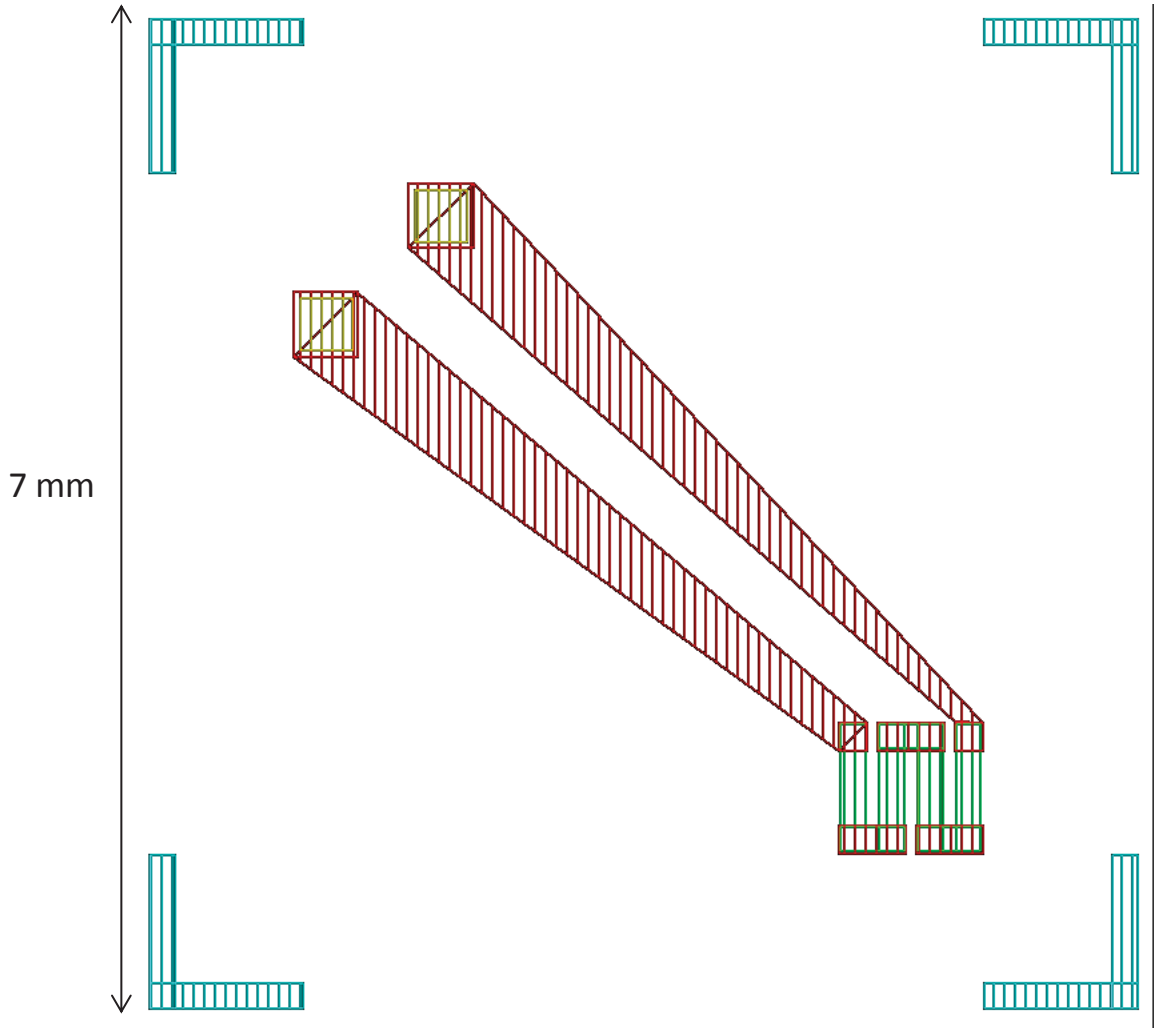

Single meander 580x193 µm (***muscle***)

Planar probe – segments (muscle)

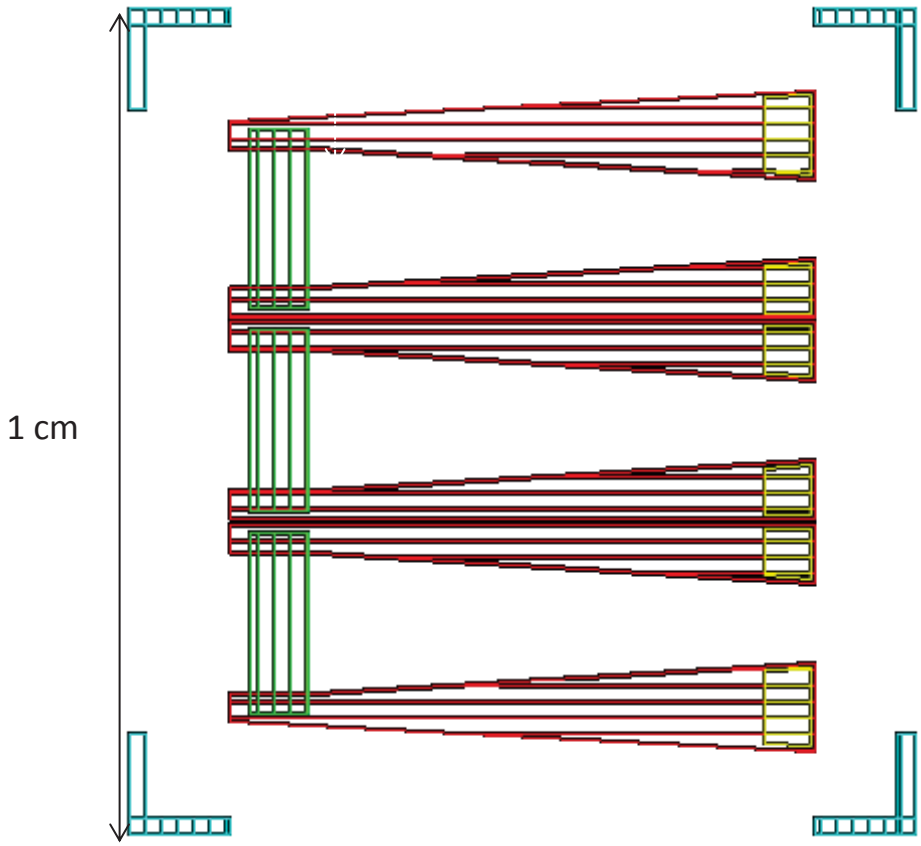

3 segments 1690x693 µm each segment (***muscle***)

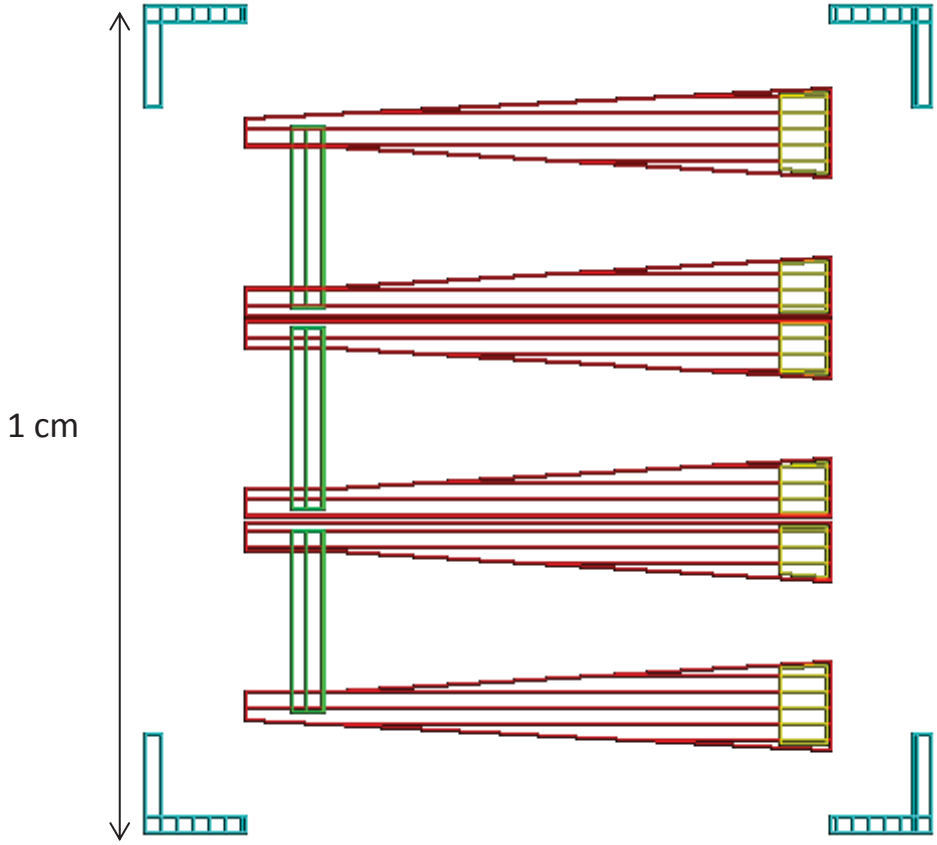

3 segments 1690x390 µm each segment (***muscle***)

Planar probe – segments (muscle)

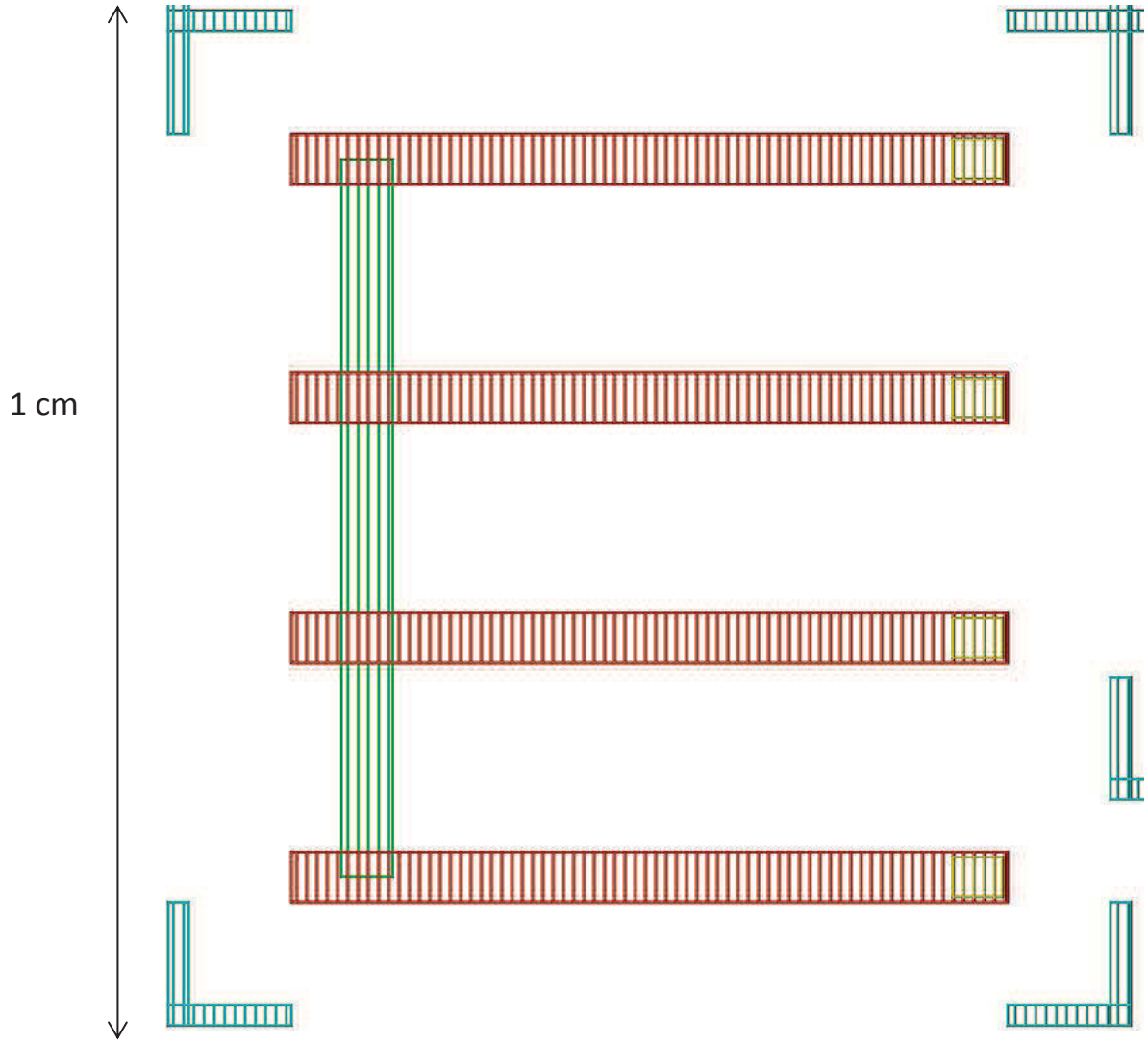

Single segments 18000x500 µm each segment (***muscle***)

Sample # M19

Process beginning : 05-02-2015

Sample : Mask Magnetrode4. Substrate : Si 200µm (wafer 2)

Antiparallel

Wafer: 5676A036 (Osprey stack). SiO_2 deposited by PECVD.

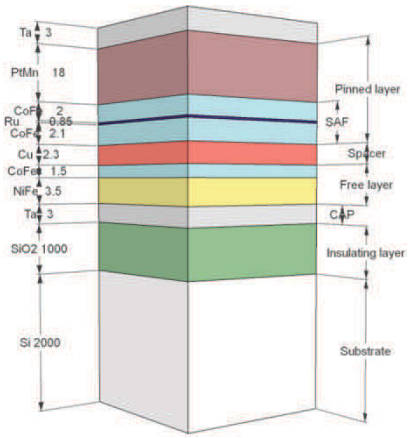

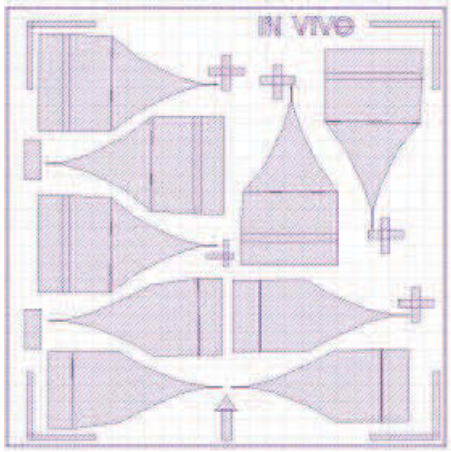

DATE	STEP
05-02-2015	GMR Lithography (UV). Mask aligner : MJB4 **Cleaning** (1min @70° each) acetone isopropanol deionized water isopropopanol **Spin coating** (photoresist : S1813) 5s @ 500 rpm, 60s @ 5k rpm, 2s @ 6k rpm. Baking 3min @ 110° **Exposure (**mask name : Magnétrode4GMR) : 10s (Lamp power : 10mW/cm^2 – wavelength: 365nm) **Development** MF319 45s / deionized water : 15s GMR etching (Ion Beam Etching) : I= 7.6mA, p=1.0^e-4mbar, P= 90W. Flow : 100.10^{-2} sccm **20min** rotated over 90° every 5min (*to ensure etching homogeneities)* Lift-off acetone 3h Contacts lithography (UV). Mask aligner : MJB4 **Cleaning** (1min @70° each) acetone isopropanol deionized water
09/02/15	isopropopanol **Spin coating** (photoresist : S1813) 5s @ 500 rpm (acceleration: 250), 60s @ 5k rpm (acc:1000), 2s @ 6k rpm. Baking: 3min @ 110° **Exposure (**mask name : Magnétrode4Contacts) : 10s **Development** MF319 45s / deionized water : 15s Contacts deposition (evaporation): **Pre etching (IBE)** 30s **Titanium (Ti) deposition** : I= 65mA. p= 1,5.10^{-7} mbar. 2min. **??nm** **Gold (Au) deposition** : I= 330mA. p= 1,7.10^{-6} mbar. 17min. **130nm**

	Lift-off acetone 24h Electrode lithography (UV). Mask aligner : MJB4 **Cleaning** (1min @70° each) acetone isopropanol deionized water isopropopanol **Spin coating** (photoresist : S1813) 5s @ 500 rpm, 60s @ 5k rpm, 2s @ 6k rpm. Baking: 3min @ 110° **Exposure (**mask name : Magnétrode4Electrode) : 10s **Development** MF319 45s / deionized water : 15s
10/02/15	Electrode deposition (evaporation - quantro): **Pre etching (IBE)** 10sec **Platinum (Pt) deposition** : I= 300mA. p = $6{,}5.10^{-7}$ mbar. **200nm** **Lift-off** acetone 24h Passivation lithography (UV). Mask aligner : MJB4 **Cleaning** (1min @70° each) acetone isopropanol deionized water isopropopanol **Spin coating** (photoresist : S1813) 5s @ 500 rpm, 60s @ 5k rpm, 2s @ 6k rpm. Baking: 3min @ 110° **Exposure (**mask name : Magnetrode4Passivation) : 15s **Development** MF319 45s / deionized water : 15s
11/02/15	Passivation deposition (sputtering): **Pre etching (IBE)** 30sec **Alumina (Al_2O_3) deposition** : P= 200W. p =$5{,}4.10^{-3}$ mbar. 1h30. **150nm** **Silicon nitritide (Al_2O_3) deposition** 200W, p = $5{,}1.10^{-3}$ mbar 1h30. **150nm** Lift-off acetone 24h DRIE lithography (UV). Mask aligner : MJB3 **Cleaning** (1min @70° each) acetone isopropanol deionized water isopropopanol **Spin coating** (Primer: HMDS) 30s @ 2k rpm, acceleration 2k min/s. Baking: 1h @ 90° **Spin coating** (photoresist: AZ4562) 30s @ 2k rpm, acceleration 2k min/s. Baking: 1h @ 90°. Photoresist thickness: 9µm **Exposure (**mask name : Magnetrode4decoupe) : 57s **Development** AZ400K:H_2O (1:4) 3min / deionized water : 15s
12/02/15	Finale shape: DRIE (Deep Reactive Ion Etching) at IEF- Minerve: **SiO_2 etching (1µm):** CHF_3 **Silicon etching (200µm):** SF_6 (etching step) Flow: 400 sccm; C_4F_8 (passivation step) Flow: 330 sccm. 400 cycles Lift-off acetone 2h